PRINCIA ANANDAN

TWO PHASE MICROFLUIDICS: NEW TREND IN MODEL IDENTIFICATION

PH.D. THESIS

TUTOR: PROF. M. BUCOLO

CO-ORDINATOR: PROF. L. FORTUNA

2012

ABSTRACT

The aim of the research is to give a proper understanding of the physical aspects involved in two-phase microfluidic systems: from the theoretical point of view to the development of numerical solutions for the flow field by Computational Modeling (*CM*) issue studies devoted to standard droplet generator for separation and segmented flow, bubble and drop formation, breakup and coalescence and then with increasing complexity in large scale microfluidic processors, bubble logic i.e. bubble to bubble hydrodynamic interaction provides an on-chip process control mechanism integrating chemistry and computation. This concept has been implemented using *COMSOL* multiphysics *3.5a* software. These show the non-linearity, gain, bistability and programmability required for scalable universal computation. Alongside experimental work, numerical tools, such as computational fluid dynamics (*CFD*), allow us to study and analyses the behavior of immiscible fluids within microchannels. Good understanding of these microfluidic flows provides us with leverage when utilized in chemical and biological applications. The study in the context of micro-optofluidics analysis have allowed to define in some detail the integrated system used to Thorlabs has provided for the experiments in micro-optofluidics. In particular, the characterization of the microfluidic detection devices has been used in the experimental studies of two-phase flow. In addition, the analysis carried out in the various micro-channels fixed unique features in terms of flow rates for each dimensions. The key issue is finally the study and designs of an embedded system optofluidics in micro-optics Lab-On-Chip (*LOC*), which allows achieving very narrow spaces in a microfluidic system, ensuring a degree of portability, which it integrates optical realizing therefore, the right balance between the two disciplines. Played as part of a global project in which design and manufacture of micro devices *LOC*, and experimental studies within micro-optofluidics could easily fit in a biochemical analysis of the microscopic scale of biological particles of various kinds. The dynamical

model identification of the asymptotic Time signals belonging to a microfluidic Two-Phase Flow process is presented. The experimental time series are used to synchronize another system with known mathematical model but unknown parameters: the Chua's oscillator. This system has been chosen for its simple mathematical structure and for the Possibility, respect to other chaotic systems, of mapping various non-linear experimental phenomena. A genetic algorithm was exploited for parameters estimation in relation to an optimization index that takes into an account of synchronization of master (microfluidic system) and slave system (Chua's oscillator).

ACKNOWLEDGMENTS

CONTENT

CHAPTER-3

OPTICAL ACTUATION AND MONITORING IN MICROFLUIDICS

CHAPTER-4

DATA DRIVEN IDENTIFICATION OF BUBBLE FLOW IN MICROCHANNEL

INTRODUCTION

The earliest microfluidic devices demonstrated that fluidic components could be miniaturized and integrated together, leading to the idea that one could fit an entire "Lab -on-Chip" (*LOC*), in much the same way that a microelectronic circuit is an entire computer on a chip. Since then, there has been tremendous interest in harnessing the full potential of this approach and, consequently, the development of countless microfluidic devices and fabrication methods.

Elastomeric materials such as Polydimethylsiloxane (*PDMS*) have emerged recently as excellent alternatives to the silicon and glass used in early devices fabricated by *MEMS* (micro-electro-mechanical systems) processes. Simplified device fabrication and the possibility of incorporating densely integrated micro valves into designs [44] have helped microfluidics to explode into a ubiquitous technology that has found applications in many diverse fields. This chapter begins with a brief introduction to microfluidics, and the physical background followed by a description of the Computational Modeling for Microfluidic Circuit Design. Alongside experimental work, numerical tools, such as computational fluid dynamics (*CFD*), allow us to study and analyze the behavior of immiscible fluids within microchannels.

Good understanding of these microfluidic flows provides us with leverage when utilized in chemical and biological applications. Many factors taken together have contributed to the success of this technology, as discussed in the final section. In Chapter 3, these desirable properties are used as a guide for the comparison of experimental microfluidics versus computational modeling to draw a

relationship so that the results of experiment can be predicted through CFD.

Microfluidics- As numerous investigators have pointed out, scaling down fluidic processes to the micro scale offers many significant advantages [2, 4, 43, 44, 45, 46, 47], some stemming directly from the reduction in size and others a result of the ability to integrate at this scale.

Benefits of size reduction- One obvious advantage are that miniaturized components and processes use smaller volumes of fluid, thus leading to reduced reagent consumption. This decreases costs and permits small quantities of precious samples to be stretched further (for example, divided up into a much larger number of screening assays) [2].

Quantities of waste products are also reduced. The low thermal mass and large surface to volume ratio of small components facilitates rapid heat transfer, enabling quick temperature changes and precise temperature control. In exothermic reactions, this feature can help to eliminate the buildup of heat or "hot spots" that could otherwise lead to undesired side reactions or even explosions [5]. The large surface to volume ratio is also an advantage in processes involving support-bound catalysts or enzymes, and in solid-phase synthesis.

At the small length scales of microfluidic devices, diffusive mixing is fast, often increasing the speed and accuracy of reactions. Dramatic performance improvements are often seen in microfluidic assays as well: reduced measurement times, improved sensitivity, higher selectivity, and greater repeatability, are common. For

example, dispersion broadening is reduced in electro-phoretic separations by the rapid dissipation of Joule heat. In some separations, sensitivity is improved simply because the reduced measurement time leads to a lower degree of peak broadening [2, 5].

Microfluidic devices sometimes enable tasks to be accomplished in entirely new ways. For example, fluid temperature can be rapidly cycled by moving the fluid among chip regions with different temperatures rather than heating and cooling the fluid in place. A device to screen for protein crystallization conditions harnesses free-interface diffusion—a process that is practical only at the micro scale—to explore a continuous range of conditions when protein and salt solutions are gradually mixed [4]. The laminar nature of fluid flow in microchannels permits new methods for performing solvent exchange, filtering, and two-phase reactions [42].

Benefits of automation and integration - Many microfluidic technologies permit the construction of devices containing multiple components with different functionalities. A single integrated chip could perform significant biological or chemical processing from beginning to end, for example the sampling, pre-processing, and measurement involved in an assay.

This is the kind of vision that led to the terms "lab-on-a-chip" and "Micro Total Analysis System (µTAS)". Performing all fluid handling operations within a single chip saves time, reduces risk of sample loss or contamination, and can eliminate the need for bulky, expensive laboratory robots. Furthermore, operation of microfluidic devices can be fully automated, thus increasing throughput, improving

ease of use, improving repeatability, and reducing the element of human error. Automation is also useful in applications requiring remote operation, such as devices performing continuous monitoring of chemical or environmental processes in inaccessible locations. Another way to increase throughput is to exploit parallelism. Single chips have been demonstrated that perform hundreds or thousands of identical assays or reactions [1, 2, 42].

These chips utilize synchronization and control-sharing so that their operation is not significantly more complex than that of a non-parallel chip. They also feature on-chip distribution of a single input sample to thousands of micro reactors—an interesting solution to the micro-to-macro interface problem. This problem refers to the mismatch between sample sizes that can be easily manipulated in the lab (μL–mL) versus the volume of micro reactors (pL–nL).

The task of controlling thousands of individual valves with a much smaller number of off-chip control inputs is achieved by implementing multiplexers or other more complex logic on-chip, as is done in microelectronic chips. Being planar and on the same scale as semiconductor integrated circuits, microfluidic devices are ideally poised to be integrated with electronic or optical components such as sensors, actuators, and control logic.

On the sensing side, significant progress has been made: chemical, electrical, optical absorption, fluorescence, flow, temperature, and pressure sensors are just some examples that have been reported. Numerous actuators, such as valves, pumps, heating elements, and electrodes for electrophoresis or electro kinetic flow, have also been demonstrated. Beebe et al. [16] devised an interesting

way to link sensing to actuation—specially tailored hydro gels respond to particular properties of the fluid by swelling and directly actuating a valve. In general, however, the potential of integrated control logic has been largely untapped. In the future, hybrid devices that perform sophisticated in situ monitoring and computation may emerge, perhaps to implement feedback control circuits that maintain optimum operating conditions or detect problems. Small integrated microfluidic devices may also offer the feature of portability, enabling mobile applications in chemical analysis, point-of-care medicine, or forensics.

The ability to perform integrated diagnostic tests where they are needed rather than in a centralized lab could reduce costs, improve turn-around time, and reduce the risk of sample mix-up. If manufactured cheaply, devices could be disposable, eliminating cross-contamination between tests. Microfluidic applications in drug delivery are also possible.

Application areas- The literature contains many thousands of reports of reactions and assays that have been carried out in microfluidics devices (see reviews in [1, 2, 4, 42, 43, 44, 45, 46, and 47]). Some have shown significant improvements in performance compared with their macro scale counterparts and have successfully competed in the commercial marketplace. In some rare cases, micro scale implementations have completely transformed the way that a certain type of experiment is performed or have enabled massively parallel experiments that previously could not even be contemplated. Among the numerous biological and biochemical processes demonstrated are

polymerase chain reaction (PCR) [2], immunoassays [290], drug screening, cell counting and sorting [84], electro-phoretic separations, nucleic acid extraction, analysis of unpurified blood samples [290], DNA sequencing [2, 4], screens for protein crystallization conditions [97], cell culture studies [2], and single cell manipulation [293]. In chemistry applications, dramatic improvements in synthetic yields and selectivities have been observed [2, 42, 44]. In addition, microfluidic devices may make possible novel reactions or processing conditions by unprecedented control over surface chemistry, local heat and mass transfer [5], or reagent concentrations in space and time (using electro-osmotic flow) [12]. The greater degree of control may help to design experiments to increase knowledge about many chemical processes [2].

Several investigators have also argued that micro reactors could be used in industrial chemical production or waste treatment plants if volumetric processing requirements are low [1, 2, 4, 42, 43, 44, 45, and 47]. Scaling up production can be achieved by bringing additional micro reactors into service at a relatively low incremental cost rather than constructing a new higher-capacity reactor—an ability that would be especially useful in pilot plants or in industries with production demands that change with time or geographical location.

The ability to set up production when and where it is needed could decrease the need for storage and transportation of hazardous or short-lived chemical products. Furthermore, micro reactors have the potential to increase the safety of dangerous processes such as the fluorination of aromatic compounds and the synthesis of organic peroxides from acid chlorides by accurate temperature control and

prevention of thermal runaway [5] [43]. In case of micro reactor failure, the consequences will be relatively minor due to the small mass of material present in the reactor at a given time.

Chapter-1

The aim of this chapter is to give a proper understanding of the physical aspects involved in two-phase microfluidic systems: from the theoretical point of view to the development of numerical solutions for the flow field.

Chapter 1

COMPUTATIONAL MODELING IN TWO PHASE FLOW MICROFLUIDIC

1.1   Theoretical Background

Microfluidics is defined as continuous where the continuum hypothesis is assumed valid. It states that the macroscopic properties of a fluid is the same as if the fluid were perfectly continuous in structure instead of consisting of molecules. In this case, physics quantities such as the mass, momentum, and energy associated with a small volume of fluid containing a sufficiently large number of molecules are taken as the sum of the corresponding quantities for the molecules in the volume.

The physical properties of the fluid per volume, such as mass density, energy density, force density and momentum density have therefore to be considered. The continuum hypothesis is no longer valid when the system under consideration approaches molecular scale. This happens in Nanofluidics, e.g., in liquid transport through nanopores in cell membranes or in artificially made nano-channels.

Here, you will be exposed to the laws that are the foundation of Microfluidics. The focus is particularly on the Navier-Stokes equations and the conservation of mass, which allow describing the dynamic behavior of fluids in micro-channels [1].

By considering some parameters whose knowledge allows assessing in advance the behavior of the entire system under certain constraints. Will then describe some examples of practical applications, including geometry through which you can get the droplet break-up.

1.1.1 Continuity Equation

Under the continuum hypothesis, the Eulerian concept where the physical properties of the fluid are described in terms of fields, focusing on fixed point in space and observing how the fields evolve in time at these points. The first fundamental equation of fluid mechanics is the continuity equation, expressing the conservation of mass in classical mechanics; this is needs to be considered it is compressible or incompressible fluids.

Take in account of material particle of position *x(t)* and of volume $\mathsf{Y}(t)$ riding along with the flow. The mass *m* of the particle can then be expressed as the local density of the fluid times the particle volume $m = \rho(x,\ t)\ \mathsf{Y}(t)$. The rate of change of this quantity is determined from

$$\frac{d}{dt}\left(\rho[x(t), t]\ \mathsf{Y}(t)\right) = \frac{\partial \rho}{\partial t}\mathsf{Y} + \nabla\rho \cdot \frac{dx}{dt}\mathsf{Y} + \rho\frac{d\mathsf{Y}}{dt}$$

$$= \left[\frac{\partial \rho}{\partial t} + \nabla \cdot (\rho v)\right] \qquad (1.1)$$

where the second equality follows from the definition of the velocity field *dx/dt* = v and the change in particle volume is expressed by the divergence of the velocity field lines $d\mathsf{Y}/dt =$ $(\nabla \cdot v)\ \mathsf{Y}$. Now since the mass of the particle is conserved, thus arrive at the equation of continuity

$$\frac{\partial \rho}{\partial t} + \nabla \cdot (\rho v) = 0. \qquad (1.2)$$

In the first case, density ρ may vary as a function of space and time, while for incompressible fluids ρ is constant in space and time.

$$\nabla \cdot v = 0. \qquad (1.3)$$

In many cases, especially in microfluidics, where the flow velocities are much smaller than the sound velocity in a liquid, the fluid can be treated as incompressible [1]. Notice however that the opposite is not true with a divergence free velocity field and a density constant in time the continuity equation only implies that the density is constant along streamlines.

1.1.2 Navier Stokes Equation

The solution of problems involving two immiscible fluids in contact requires the solution of the Navier-Stokes equations containing the contribution of the surface tension, which allows the description of the phenomena of coalescence and / or breakage of the interface separation.

The Navier-Stokes equations are a system of partial differential equation that describes the behavior of a fluid from the macroscopic point of view. The basic hypothesis is that the fluid can be modeled as a continuous body deformable. They assume therefore the continuity of the fluid under examination, i.e. the system loses its validity in the study of a rare gas. The equations owe their name to Claude-Louis Navier and George Gabriel Stokes.

The predictive efficiency of these equations is paid in terms of computational difficulties. In the general case involve a mix of five scalar equations partial differential equations lie 20 variables. The balance between equations and unknowns is with the definition of the properties of the fluid considered, any field strengths into play and mathematical considerations. Furthermore,

of their non-linearity, the Navier-Stokes equations do not allow almost never an analytical solution (i.e. an exact solution), but only numeric (an approximate solution with a numerical method).

The Navier-Stokes equations are able to fully describe any fluid flow, also turbulent. In particular for a turbulent flow, that is, where the trajectories of the particles flow are no longer constant over time, a numerical approach of calculation is called general mind direct numerical simulation [2]. Due to the fact that the computing resources necessary for their resolution grows with the Reynolds number and that this number can have values of the order of 10^6-10^9, such an approach is technically impossible. Alternative to the numerical simulation can be taken less expensive systems such as the formulation injured equations mediated.

The equations are supplemented by boundary conditions and initial conditions (conditions imposed at the beginning time of the phenomenon to be studied). They can also be integrated by the equation of state of an ideal gas and from the equations of conservation of the individual gaseous species in the case of a gas mixture. The solution of equations provides the field of fluid velocity. From this it will be then possible to trace all the other quantities that characterize the flow. To this end it has developed a branch of fluid dynamics called Computational Fluid Dynamics (CFD).

"The Navier-Stokes equations are a system of partial differential equations that describes the behavior of a fluid from the macroscopic point of view. The underlying assumptions of such a system are that the fluid may be understood as a continuous body deformable." With the term continuous deformable means a three-

dimensional body occupying a certain volume that during its motion is subject to deformation is of volume and shape.

The predictive efficiency of these equations is paid in terms of computational difficulties. They also are able to fully describe any fluid flow, also turbulent. In particular for a turbulent flow, that is, where the trajectories of the particles flow are no longer constant over time, a numerical approach of calculation is generally called direct numerical simulation. In the general case involve a mix of five scalar equations partial differential equations in 20 variables. The balance between equations and unknowns occurs with the definition of the properties of the fluid under consideration, any of the field strengths in play and with mathematical considerations.

Because of their non-linearity, the Navier-Stokes equations do not admit almost never an analytical solution (i.e., an exact solution), but only numerically (an approximate solution with a numerical method). The equations are supplemented by boundary conditions and initial conditions. The solution of equations provides the field of fluid velocity. From this it will be then possible to trace all the other quantities that characterize the flow.

Again by considering a material particle riding along with the flow, the particle momentum is then $p = mv$, with rate of change

$$\frac{dp}{dt} = m\frac{d}{dt}\left(v[x(t),t]\right) = m\left(\frac{\partial v}{\partial t} + v \cdot \nabla v\right) \qquad (1.4)$$

According to Newton's second law this is equal to the sum of the external forces. For a particular particle those are the contact

force from the surrounding fluid $\nabla \cdot \sigma$ ⩒, where σ is the Cauchy stress tensor, together with the external body forces acting on the particle f ⩒ where f is the body force density, e.g. gravity ρg. Thus the arrive at Cauchy's equation of motion

$$\rho \left[\frac{\partial v}{\partial t} + (v \cdot \nabla)v \right] = f + \nabla \cdot \sigma \qquad (1.5)$$

the stress tensor σ is defined such that the contact force F that the material on one side of a small surface patch of area A and outward normal n feels from the material on the other side of the patch is

$$\mathcal{F} = \sigma \cdot nA \qquad (1.6)$$

and it can be shown that σ is symmetric, that is $\sigma_{ij} = \sigma_{ji}$. Conventionally the stress tensor is split according to

$$\sigma_{ij} = -p\delta_{ij} + \tau_{ij} \qquad (1.7)$$

where δ_{ij} is the Kronecker delta and p is the hydrodynamic pressure while τ_{ij} is the so-called deviatoric stress tensor. By definition the hydrodynamic pressure is given in terms of the trace of the stress tensor as

$$p = -\frac{1}{3}\Sigma_k \, \sigma_{kk} = -\frac{1}{3}Tr\sigma, \qquad (1.8)$$

and for a fluid at hydrostatic equilibrium this coincides with the hydrostatic pressure since fluids at rest cannot sustain shear stress. Hence the deviatoric stress tensor

$$\tau_{ij} = \sigma_{ij} + \delta_{ij}\,p \qquad (1.9)$$

is said to be pressure free since by construction $Tr\tau = 0$. With these definitions the Cauchy equation of motion reads

$$\rho \left[\frac{\partial v}{\partial t} + (v \cdot \nabla)v \right] = -\nabla p + \nabla \cdot \tau + f. \qquad (1.10)$$

1.1.3 Energy Equation

Define the field $\mathcal{U}(x,t)$ as the local total energy per unit mass. Then the energy of a material particle can be written as $\mathcal{E} = \rho \mathcal{U} \curlyvee$. The particle energy increases from work done by the external forces $dW = (f + \nabla \cdot \sigma) \curlyvee \cdot v dt$ and from heat sources $q \curlyvee$ acting inside the particle while it decreases from the heat flux q out of the particle surface [1]. Thus

$$\frac{d}{dt}(\rho \mathcal{U} \curlyvee) = (f + \nabla \cdot \sigma) \curlyvee \cdot v + q \curlyvee - \int_s dS \, n \cdot q \qquad (1.11)$$

by Fourier's law the heat flux is $q = -k\nabla T$ where T is the temperature and k is the thermal conductivity. Then applying Gauss' theorem to the surface integral and cancelling out $\curlyvee$ arrive at

$$\frac{\partial (\rho \mathcal{U})}{\partial t} + \nabla \cdot (\rho \mathcal{U} v) = (f + \nabla \cdot \sigma) \cdot v + q + \nabla \cdot (k\nabla T) \qquad (1.12)$$

for an incompressible Newtonian fluid with constant density and isotropic thermal conductivity this reduces to

$$\rho \left(\frac{\partial \mathcal{U}}{\partial t} + v \cdot \nabla \mathcal{U} \right) = f \cdot v + \frac{1}{2} \mu \nabla^2 (v \cdot v) + q + k\nabla^2 T \qquad (1.13)$$

1.1.4 Dimensionless Numbers in Microfluidics

Scaling analysis and dimensionless numbers play a key role in physics. They indicate the relative importance of forces, energies, or time scales in presence and lead the way to simplification of complex problems. Besides, the use of dimensionless parameters and variables in physical problems

brings a universal character to the system of equations governing the physical phenomena, transforming an individual situation into a generic case. The same remarks apply to micro-scale physics. Only forces, energies, and time scales are different, and, even if some dimensionless numbers are the same as the one used at the macro-scale, many are specific to micro-scales [1]. The most widely used dimensionless numbers in microfluidics, after having recalled the fundamental Buckingham's Pi theorem has presented below and the scaling laws and characteristics times.

(a) Buckingham's Pi Theorem

(b) Knudsen Number

(c) Reynolds Number

(d) Capillary Number

(e) Weber Number

(f) Ohnesorge Number

(g) Dean Number

(h) Péclet number

Buckingham's Pi Theorem - Buckingham's pi theorem is a key theorem in dimensional physics [1]. The theorem states that for a system of equations involving n physical variables, depending only on k independent fundamental physical quantities (unities, for example), the system depends only on $p = n - k$ dimensionless variables constructed from the original variables.

At the same time, the use of the theorem is very powerful because it does not involve the form of the equation or system of equations, just the variables intervening in the problem. Also, because the choice of dimensionless parameters is not unique, it

only provides a way of generating sets of dimensionless parameters. The user still has to determine the meaningful dimensionless parameters corresponding to the specific problem. More formally, in mathematical terms,

$$f(q_1, q_2, \ldots\ldots\ldots, q_n) = 0 \qquad (1.14)$$

where the q_i are the n physical variables, expressed in terms of k independent physical units, (14) can be restated as

$$F(\pi_1, \pi_2, \ldots\ldots., \pi_p) = 0. \qquad (1.15)$$

where the π_i are dimensionless parameters constructed from the q_i by $p = n - k$ equations of the form

$$\pi_i = \left(q_1^{m_1}\, q_2^{m_2}\, q_n^{m_n}\right) \qquad (1.16)$$

where, the exponents m_i are integer numbers. For example, if the Navier-Stokes equations for a flow around an obstacle, the variables are the obstacle dimension L, the flow velocity far from the obstacle U, the fluid density ρ, and the fluid viscosity m. Hence, $n = 4$. The units intervening in the problem are to the number of 3: kilogram, meter, and second. The Buckingham theorem then states that there is only $4-3 = 1$ dimensionless parameter characterizing the problem. This parameter is the well-known Reynolds number.

Knudsen number - The Knudsen number defines the transition between micro- and nano-scales. This transition is extremely

important; it defines the lower limit where the continuum hypothesis can be used [1] [2]. The Knudsen number is defined as

$$Kn = \lambda\,L \qquad (1.17)$$

where, L is a representative physical length scale and λ the mean free path. *Kn* is small at the micro-scale, and is larger than 1 at the nano-scale. For a gas at normal conditions, λ is of the order of 1 *m*m, whereas it is smaller for a liquid (5–10 nm).
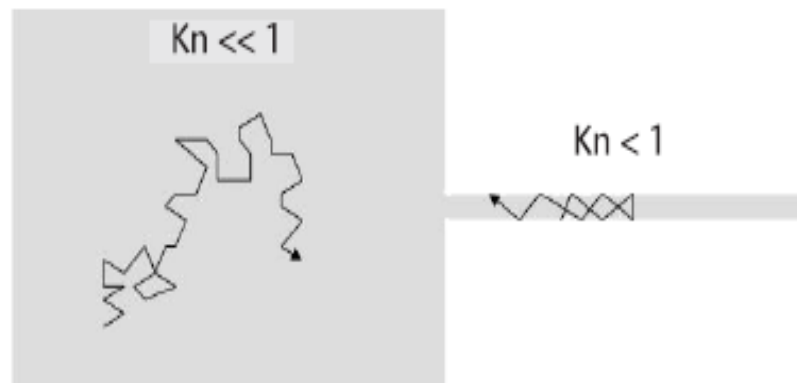
Figure. 1.1 Schematic of microscale (Kn <<1) and nanoscale (Kn >1) chambers.

Hydrodynamic Characteristic Times - In micro-hydrodynamics, four characteristic times are usually defined. These times will be used in the following sections to establish some dimensionless groups:

a)   The convective (or viscous) time scales the time for a perturbation to propagate in the liquid

$$\tau_C = R/V \qquad (1.18)$$

where R is a dimension and V is the velocity of the liquid. Depending on the flow configuration (shear or elongational), the convective time may also be written as

$$\tau_C = \frac{1}{\dot{\gamma}} \; or \; \frac{1}{\dot{\varepsilon}} \qquad (1.19)$$

where, $\dot{\gamma}$, $\dot{\varepsilon}$ are respectively, a shear rate and an elongation rate.

b)   The diffusional time is the time taken by a perturbation to diffuse in the liquid

$$\tau_D = \frac{R^2}{\upsilon} \qquad\qquad (1.20)$$

where, $\upsilon = m/\rho$ is the kinematic viscosity (units m2/s).

c)   The Rayleigh time is a time scale of the perturbation of an interface under the action of inertia and surface tension [3–5]

$$\tau_R = \sqrt{\frac{\rho R^3}{\gamma}} \qquad\qquad (1.21)$$

Newtonian Fluids - The terms of Newtonian fluid (named after Isaac Newton) is defined to be a fluid whose shear stress is linearly proportional to the velocity gradient in the direction perpendicular to the plane of shear [1] [2]. This definition means regardless of the forces acting on a fluid, it continues to flow. For example, water is a Newtonian fluid, because it continues to display fluid properties no matter how much it is stirred or mixed. A slightly less rigorous definition is that the drag of a small object being moved slowly through the fluid is proportional to the force applied to the object. (Compare friction). Important fluids, like water as well as most gases behave to good approximation as a Newtonian fluid under normal conditions on Earth

Let us mention here that usual liquids like water belong to the Newtonian category and polymeric fluids belong to the non-Newtonian category. The Reynolds number characterizes the

relative importance of inertial and viscous forces. It is usually written under the form

$$Re = V\,R\,/\,v \qquad\qquad (1.22)$$

where, V is the average fluid velocity and R is a length characteristic of the geometry.

$$Re = \frac{\rho V^2}{\mu V / R} \qquad\qquad (1.23)$$

The Reynolds number is the ratio of a dynamic pressure-linked to inertia-to shearing stress-linked to viscous forces. In microfluidics, the Reynolds number is generally small, corresponding to a laminar flow regime [1] [2]. Very few microfluidic systems use turbulent flows. It is recalled here that, in enclosures, a number of Reynolds of *2,000* is required to reach the transition to turbulence. A more subtle sub classification can be made for the laminar regime. A very low Reynolds number (less than *0.5*) indicates a creeping flow, for which the Stokes approximation is valid, this is the general case.

However recently, with the development of micro systems for cells handling, larger velocities are often used corresponding to Reynolds numbers in the range from *1-20*. Figure *1.2* schematizes the definition of the Reynolds number for some geometrical configurations.
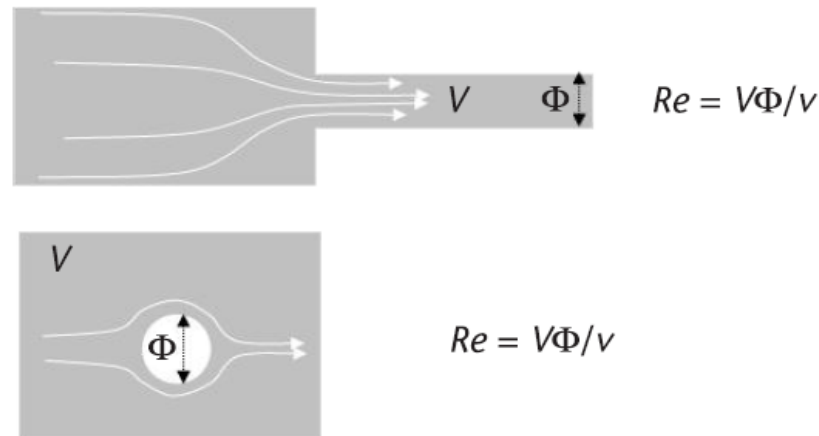
Figure 1.2 Reynolds numbers: (a) Reynolds number in a channel and (b) Reynolds number around a spherical particle.

Capillary Number- *It* is very important in two-phase microfluidics. It compares viscous/elongational forces to surface tension forces. The capillary number can take different forms, depending on the physics of the problem. It can be built using the average velocity, the shear rate, or the elongational rate:

$$Ca = \eta V / \gamma \qquad\qquad (1.24)$$

$$Ca = \eta \dot{\gamma} R / \gamma$$

$$Ca = \eta \dot{\varepsilon} R / \gamma$$

Remarking that the shear stress can be written ηVR, $\eta \dot{\gamma}$, $\eta \dot{\varepsilon}$ depending on the specific configuration, and the capillary pressure γ/R, one immediately sees that the capillary number is the ratio of the viscous forces to the capillary forces [1] [2].

Let us illustrate this remark by two examples. In flow focusing devices (*FFD*), the capillary number is a relevant criterion to predict liquid thread breakup see figure *1.3(a)*. In this case, the capillary number is built on the shear rate (or elongation rate).

As the filament stretches and thins down, the capillary number decreases and when it becomes less than a critical value $Ca_{crit} \sim 0.1$ to 0.01, the surface tension forces break the liquid filament into droplets, minimizing the interfacial area (hence the surface energy); this phenomenon is usually called the Rayleigh-Plateau instability.

In a plug flow, the friction of the plugs with the walls is a function of the capillary number of the liquid of the plugs shown in figure *1.3(b)*.
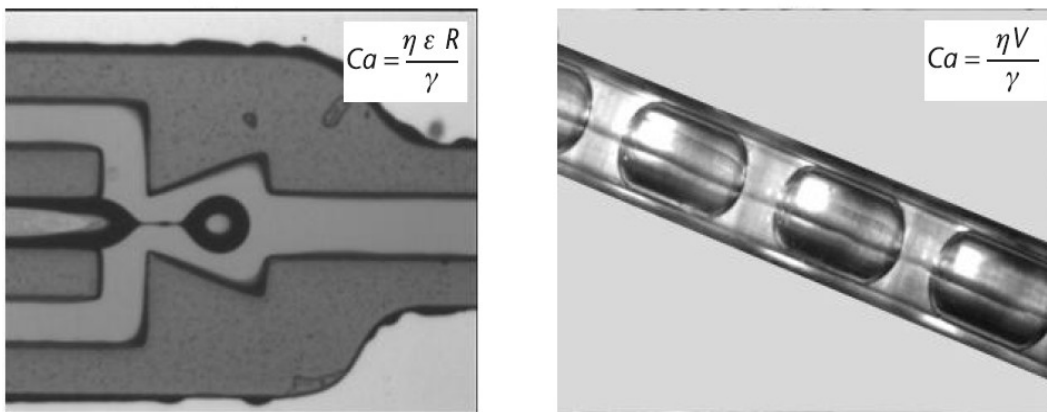
Figure 1.3 (a) Capillary number for an elongating liquid thread in a flow focusing device (FFD) and (b) capillary number for plug flow in a tube.

Weber Number

The Weber number is used to predict the disruption of an interface under the action of strong inertial forces [1]. More specifically, the Weber number is the ratio of inertial forces to surface tension forces

$$We = \frac{\rho V^2 R}{\gamma} = \frac{\rho V^2}{\gamma/R} \qquad (1.25)$$

The numerator corresponds to a dynamic pressure ρV^2 and the denominator to a capillary pressure γ/R. A strong surface tension maintains the droplet as a unique microfluidic entity with a convex interface. If the inertia forces are progressively increased, the interface is first deformed by waves, becomes locally concave, and is finally disrupted.

Ohnesorge Number- It relates the viscous and surface tension forces. It is defined as

$$Oh = \frac{\eta}{\sqrt{\rho \gamma L}} = \frac{\sqrt{We}}{Re} \qquad (1.26)$$

The Ohnesorge number has been shown to be a good criterion to predict the breakup of liquid jets in a gas. Another expression seldom used for the comparison of viscous and surface tension forces is the Laplace number defined by

$$La = {}^{1}\!/_{Oh^2} \qquad (1.27)$$

Dean Number - It is a dimensionless group in fluid mechanics, which occurs in the study of flow in curved pipes and channels [1]. The Dean number is typically denoted by the symbol *De* for flow in a pipe or tube. it is defined as:

$$De = \frac{\rho V D}{\mu} \left(\frac{D}{2R}\right)^{1/2} \qquad (1.28)$$

where ρ is the density of the fluid, μ is the dynamic viscosity, V is the axial velocity scale, D is the diameter (other shapes are represented by an equivalent diameter, see Reynolds number), and R is the radius of curvature of the path of the channel. The Dean number is therefore the product of the Reynolds number (based on

axial flow *V* through a pipe of diameter *D*) and the square root of the curvature ratio.

Péclet Number – It is a dimensionless number relevant in the study of transport phenomena in fluid flows. It is named after the French physicist Jean Claude Eugène Péclet [1] [2]. It is defined to be the ratio of the rate of advection of a physical quantity by the flow to the rate of diffusion of the same quantity driven by an appropriate gradient.

In the context of the transport of heat, the Péclet number is equivalent to the product of the Reynolds number and the Prandtl number. In the context of species or mass dispersion, the Péclet number is the product of the Reynolds number and the Schmidt number.

$$Pe = \frac{u \cdot W}{d} \qquad (1.29)$$

In engineering applications, the Péclet number is often very large. In such situations, the dependency of the flow upon downstream locations is diminished, and variables in the flow tend to become 'one-way' properties. Thus, when modeling certain situations with high Péclet numbers, simpler computational models can be adopted.

1.2   Two Phase Microfluidics

The two-phase flows are characterized by the presence of two phases of the same component and they represent the simplest case of multiphase flows. To be precise it should also use the term

multi component to indicate the flows consist of elements belonging to chemically different phases.

For example, a flow of water and steam is mono-phase component, while a stream of water and air is bi-phase component. The two-phase flows play a crucial role in the systems lab-on-a-chip. They are obtained by sliding simultaneously two different fluids within a single micro channel. May be composed of two immiscible liquids, such as oil and water, or by a liquid phase and a gaseous [2] [3]. Microfluidic applications In two-phase, very often, is useful carry two different fluids in order to prepare them for subsequent analysis, get any reaction or perform chemical analyzes.

The analytical solutions to the Navier–Stokes equation are: the pressure-driven, steady state flows in channels, also known as Poiseuille flows or Hagen–Poiseuille flows. This is major importance for the basic understanding of liquid handling in lab-on-a-chip systems [1] [2] [3].

Poiseuille flow - In a Poiseuille flow, the fluid is driven through a long, straight, and rigid channel by imposing a pressure difference between the two ends of the channel [1]. Originally, Hagen and Poiseuille studied channels with circular cross-sections; as such channels are straightforward to produce. However, especially in microfluidics, one frequently encounters other shapes.

Hydraulic resistance - In section *1.2*, the Poiseuille flow has explained for the pressure-driven, steady-state flow of an incompressible Newtonian fluid through a straight channel that a constant pressure drop Δp resulted in a constant flow rate Q. This result can be summarized in the Hagen-Poiseuille law.

$$\Delta p = R_{hyd} Q = \frac{1}{G_{hyd}} Q \qquad (1.30)$$

The hydraulic resistance can be defined as the property that presents a pipeline to oppose the flow of a fluid inside of it. It may be constant or variable according to the specific operating conditions of the system. In Fluid dynamics, the concept of hydraulic resistance is related to the law of Poiseuille (or also of Hagen-Poiseuille) [1]. It shows that in a conduit where a viscous fluid flows in laminar regime, to parity of the other parameters, the flow rate is proportional to the pressure difference applied across the duct.

The Hagen–Poiseuille law, equation *1.30*, is completely analogous to Ohm's law, $\Delta V = RI$ relating the electrical current I through a wire with the electrical resistance R of the wire and the electrical potential drop ΔV along the wire. The SI units used in the Hagen–Poiseuille law are:

$$[Q] = \frac{m^3}{s}, [\Delta p] = Pa = \frac{N}{m^2} = \frac{kg}{ms^2}, [R_{hyd}] = \frac{Pas}{m^3} = \frac{kg}{m^4 s}$$

The concept of hydraulic resistance is fundamental to the characterization of micro-channels of a microfluidic system. The hydraulic resistance depends strongly on the section of the duct: increases as the length of the pipe L and decreases with the tube section.

Also increases proportionally with respect to the viscosity of the fluid. Below are expressions for the calculation of the hydraulic resistance in the case of some specific conducted to vary the section:
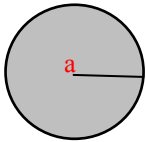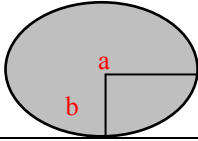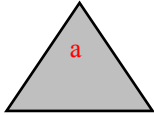
Section of the channel	Hydraulic Resistance
Circle (radius a)	$\dfrac{8}{\pi}\eta L\dfrac{1}{a^4}$
Elliptical (major axis a, minor axis b)	$\dfrac{4}{\pi}\eta L\dfrac{1+(b/a)^2}{(b/a)^2}\dfrac{1}{a^4}$
equilateral triangular (side a)	$\dfrac{320}{\sqrt{3}}\eta L\dfrac{1}{a^4}$
parallel walls (height h, width w)	$12\eta L\dfrac{1}{wh^3}$
Rectangular (altezza h, larghezza w)	$\dfrac{12\eta L}{1-0.63(\frac{h}{w})}\dfrac{1}{wh^3}$
Square (side a)	$\dfrac{12\eta L}{1-0.917*0.63}\dfrac{1}{h^4}$

Table. 1.1. Hydraulic resistance for straight channels with different cross-sectional shapes.

where *L* indicates the length of the channel (not is a sectional dimension), while η is the dynamic viscosity of the fluid. When two channels are connected to form a channel longer, not always the law of Poiseuille turns out to be still valid. Check that the Reynolds number is sufficiently low:
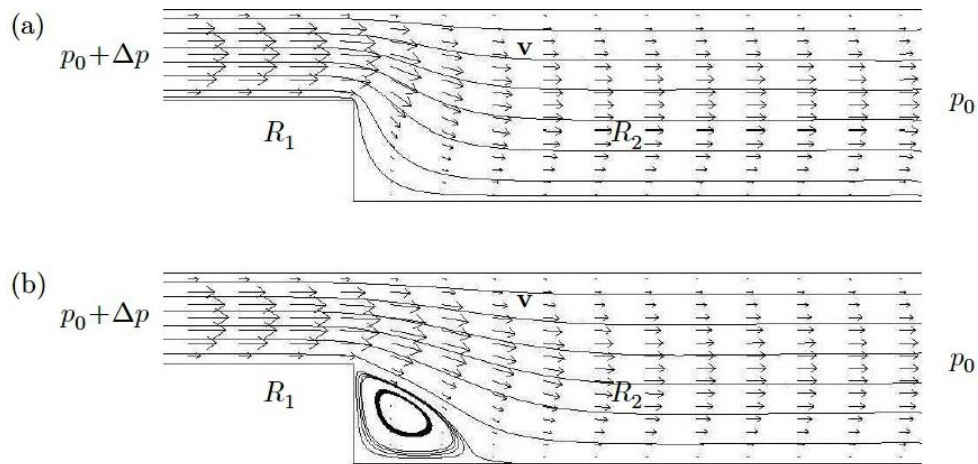
Fig. 1.4. (a) Two channels in series with down Re; (b) Two channels in series with Re too high.

In figure *1.4* shows a case in which the Reynolds number (Re) is sufficiently small: we can assume still valid as the law of Poiseuille and write $\Delta P = (R_1 + R_2)Q$ in the case of figure *1.4(b)* instead *Re* is such as to have the formation of a "convective motion", Poiseuille's law is not applicable.

Assuming a value of $Re \geq 0$ is therefore possible to consider the series of two resistors hydraulic and write so that the equivalent resistance is:

$$R = R_1 + R_2 \qquad (1.31)$$

It is also possible to consider two channels connected in parallel as in figure *1.5*. Assuming the same conditions with respect to the Reynolds number will have the following equivalent resistance:

$$R = \left(\frac{1}{R_1} + \frac{1}{R_2} \right) \qquad (1.32)$$
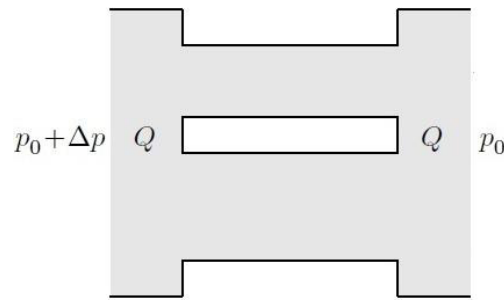
Fig. 1.5. Two channels connected in parallel

Hydraulic Capacity - In the previous paragraph has been discussed the analogy between the Poiseuille's law and Ohm's law: it evidently known as the change in pressure ΔP and the flow rate Q (volume V of unit of time) correspond respectively to the potential difference ΔU and the current (charge q of units of time) [1].

Similarly to the case of resistance, starting from the definition of electric capacity

$$C = \frac{dq}{dU} \qquad (1.33)$$

that the concept of hydraulic capacity given by the following expression:

$$C_{hyd} = -\frac{dV}{dP} \qquad (1.34)$$

where the minus sign indicates a reduction of the volume as the pressure increases.

The hydraulic capacity exists because neither the real fluids nor the channels containing them are totally rigid, but have certain elasticity. Their volume changes, often even of a small amount, varying the environmental pressure. This implies the property of an element such as a channel or a tank to store a greater or lesser

amount of fluid, which results in a determined value of hydraulic capacity. Generally it can be considered constant and the hydraulic capacity given by the following expression:

$$C = \frac{\Delta V}{\Delta p} \qquad (1.35)$$

In the *SI* is measured in *m³/Pa*. Until now in microfluidic technology, it was possible to realize elements of hydraulic capacity variable by making use of elastic materials that change their shape depending on the amount of liquid they receive.

1.3   Computational Fluidic Dynamics (CFD).

Theory and modeling methods can be conveniently classified into four groups, depending on the length and times scales to which they imply

a)   The electronic scale of description in which matter is regarded as made up of fundamental particles (electron, protons, etc.) and is described by quantum mechanics;

b)   The atomistic level of description, in which matter is made up of atoms, whose behavior obeys the laws of statistical mechanics;

c)   The mesoscale level, in which matter is regarded as composed of blobs of matter, each containing a number of atoms; and

d)   The continuum level, in which matter is regarded as a continuum, and the well-known macroscopic laws (equations of continuity and momentum conservation, constitutive equations such as Fourier's law, etc.) apply.

For most fluids, the scale of tens or hundreds of micrometers is well suited to the standard continuum description of transport processes, even though surface forces play a more important role than in macroscopic applications. Continuum methods for computations of two fluids flows are based on macroscopic conservation laws for mass, momentum, and energy [1] [2]. They rely on the coupling of a method for description of the phase evolution often expresses the conservation of phase with a solver for the momentum equation and the energy equation. Here, the full non-linear problem and do, therefore, not consider methods that are limited to Stokes flow, such as the boundary integral method.

In the following, first various methods for description of the interface evolution and then consider the coupling of these algorithms with equation describing the transport of momentum, species mass and energy. Detailed information about these balance equations can be found in various text books.

There are two main numerical methods for simulating multiphase flow in microfluidics: interface tracking methods and interface capturing methods. The latter class of methods is ideal for simulation of immiscible two-fluid systems.

Interface Tracking Methods – In interface tracking methods (or sharp-interface methods) the computational mesh elements lies in part or fully on fluid-fluid interfaces. Such methods, including boundary-integral methods, finite element methods, and immersed boundary methods, are a very accurate instrument for simulating the onset of breakup and coalescence transitions but encounter difficulties in simulating through and the past transitions [3].

Interface Capturing Methods – Simulations through breakup and coalescence transitions using interface capturing methods (lattice – Boltzmann and lattice gas, constrained –interpolation-profile, level set, and volume of –fluid, couple level set, partial miscibility-model and phase field methods) do not require mesh cut and connect operations because the mesh elements do not lie on the interface, but rather the interface evolves through the mesh.

The fluid discontinuities (e.g. *density*, *viscosity*) are smoothed and the surface tension force is distributed over a thin layer near the interface to become a volume force (surface tension being the limit as the layer approaches zero thickness). Interface capturing methods are then ideal for simulating breakup and coalescence in immiscible two-fluid systems (and the effect of surfactants) and for three or more liquid components, being especially powerful for microchannel design.

1.3.1 Level set.

Flow problems with moving interfaces or boundaries occur in a number of different applications, such as fluid-structure interaction, multiphase flows, and flexible membranes moving in a liquid. One possible way to track moving interfaces is to use a level set method. A certain contour line of the globally defined function, the level set function, then represents the interface between phases. With the Level Set application mode you can move the interface within any velocity field [2].

The level set method is a technique to represent moving interfaces or boundaries using a fixed mesh. It is useful for problems where the computational domain can be divided into two domains separated by an interface. Each of the two domains can

consist of several parts. Figure *8-13* shows an example where one of the domains consists of two separated parts. The interface is represented by a certain level set or iso-contour of a globally defined function, the level set function. In *COMSOL* Multiphysics, is a smooth step function that equals zero in a domain and one in the other, across the interface, there is a smooth transition from zero to one. The interface is defined by the φ *0.5* iso-contours, or the level set, of. *Figure 8-14* shows the level set representation of the interface in figure *1.6*.
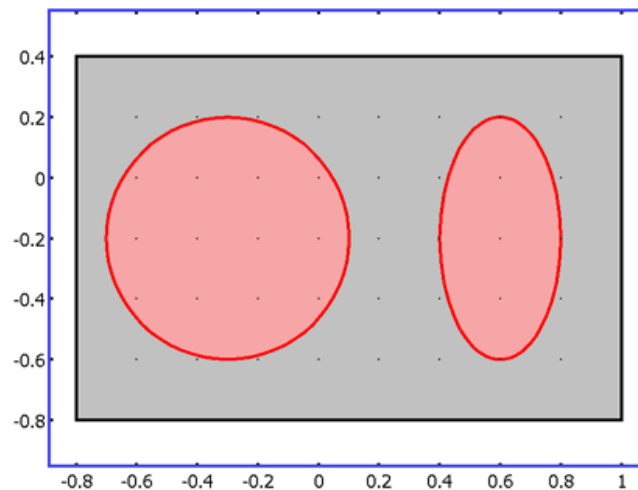
Fig.1.6. Example of two domain divided by an interface. In this case, one of the domains consists of two parts. Figure 8-14 shows the corresponding level set representation
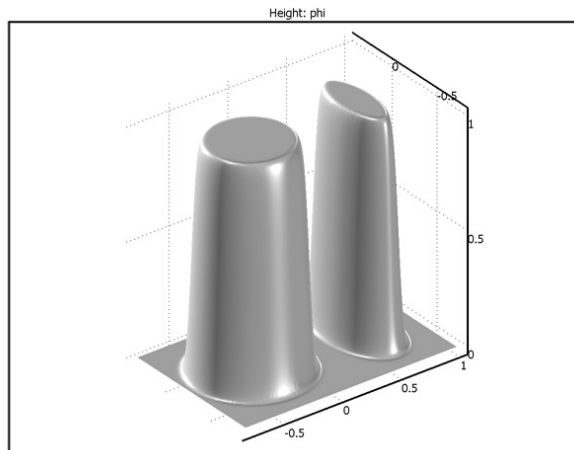
Fig. 1.7. Surface plot of the level set function corresponding to Figure 1.

Numerical methods for interfaces of zero thickness can be divided into two main groups depending on the type of the grid. In the first group, moving unstructured grids are used and the interface is treated as a boundary.

The interface is represented by a set of cell edges; this allows a precise representation of interfacial jumps in the physical variables on the zero thickness interfaces without any smoothing. Such methods are often based on the arbitrary Largranian-Eulerian formulation, where the interface is resolved by a moving mesh [2]. Local mesh adaptations including mesh coarsening and mesh refining can be performed for both the interior and the interface elements to maintain good mesh quality, to achieve enough mesh resolution, to capture the changing curvature, and to obtain computational efficiency. However handling topological transitions of fluids particles such as coalescence, breakup and pinch-off requires rather complex algorithms.

In this review, the focus is on the second group of methods. In these the momentum equation is solved on a structured grid and an interface representation and advection algorithm is required to

define its motion across the computational domain. These methods may be divided into two classes. In front-capturing methods, the interface is implicitly embedded in a scalar field function defined on a fixed Eulerian mesh, such as a Cartesian grid. The second category is given by Lagrangian front-tracking methods, in which the interface is explicitly represented by Lagrangian particles and its dynamics is tracked by the motion of these particles. Among the front-capturing methods are the volume-of-fluid (*VOF*) and level set (*LS*) method which are, at least in their simplest version, relatively simple to implement. An early Lagrangian method is Marker in Cell (*MAC*) method where a fixed number of discrete Lagrangian particles are advected by the local flow.

The distribution of these particles identifies the regions occupied by a certain fluid. Lagrangian techniques emerged with the front-tracking (*FT*) method which uses surface markers. *FT* methods can give a more precise evolution of a deforming interface, but they may be relatively complex, with their need to book-keep logical connections among surface elements [2] [3]. In the following, discussion of the level set methods in a brief.

The level set method was introduced by osher and sethian as a general technique to capture a moving interface. It has subsequently been applied to two phase flows as well as in many other fields. The basic idea of the level set method is to represent the interface by the zero level set of a smooth scalar function

$$\phi(x) : R^D \to R, \qquad \Gamma = \{x : \phi(x) = 0\}.$$

Thus, the position of the interface is only known implicitly through the nodal values of ϕ. In order to extract the position of the interface, an interpolation of the ϕ data on the grid points must be performed. One often mentioned advantage of the level set method

is its ability to handle topological changes and complex interfacial shapes in a simplified way. In practice, the level set function ϕ is initialized as the signed distance from the interface. For description of the interface evolution the phase indicator function in

$$\frac{DX_{\pm}}{Dt} = \frac{\partial X_{\pm}}{\partial t} + u \cdot \nabla X_{\pm} = 0; \text{ is replaced by } \phi.$$

This level set equation is solved with high-order numerical discretization schemes in time and space, e.g. third-order total variation diminishing (*TVD*) Runge-Kutta schemes and third or fifth order Hamilton-Jacobi (*HJ*) weighted essentially non-oscillatory (*WENO*) schemes. Under evolution in time ϕ does not retain the property of a signed distance function and may develop steep and very small gradients. This results not only in inaccurate calculation of the interface normal vector and curvature but also in severe errors regarding mass conservation. For improved mass conservation of level set methods it is essential that ϕ stays a smooth function throughout the entire simulation. In order to achieve this, a reinitialization step is introduced, where the level set function is transformed into a scalar field that satisfies the properties of a signed distance function and has the same zero level set.

This reinitialization of ϕ is done in regular time intervals, often after each time step, but less frequent reinitializations are also common. For this reinitialization essentially two different methods are used in literature. Fast marching methods solve the Eikonal equation $|\nabla \phi| = 1$ by computing the signed distance value for points in the computational domain or in a narrow band near the

interface. A more efficient and popular approach is to use a partial differential equation to reinitialize the level set function. Sussman et al. proposed to solve the following transient problem to steady state.

$$\frac{\partial \phi}{\partial \tau} = sgn(\phi_0)(1 - |\nabla \phi|)$$

$$\phi(x, \tau = 0) = \phi_0(x) \qquad (1.36)$$

Here, τ is the virtual time for reinitialization, ϕ_0 is the level set function at any computational instant, and sgn(x) is a smoothed signum function which Sussman et al. approximated numerically as

$$sgn(\phi_0) = \frac{\phi_0}{\sqrt{\phi_0^2 + L_\epsilon^2}} \qquad (1.37)$$

Here, L_ε is a small length scale to avoid dividing by zero, usually chosen as the mesh size. Equation *1.37* has the formal property that ϕ remains unchanged at the interface and converges to $|\nabla \phi| = 1$ away from the interface. Russo and Smereka showed that the discretized version of equation *1.37* can displace the zero level set and may lead to substantial errors due to the reinitialization; as a remedy they proposed a fix for the redistance step discretization of Sussman et al [2]. recently, Hartman et al. presented two new improved formulations of the methods of Sussman et al. and Russo and Smereka for differential equation-based constrained reinitialization of the level set method.

Different temporal discretization schemes for solution of equation *1.37* were investigated by min. However, even with a frequent reinitialization step the level step method tends in long time simulations to shrink convex iso-surfaces, i.e. it leads to mass

loss. To correct this mass loss, global as well as local mass correction steps have been proposed to explicitly enforce mass conservation.

1.3.2 Phase field.

The phase field method offers an attractive alternative to more established methods for solving multiphase flow problems. Instead of directly tracking the interface between two fluids, the interfacial layer is governed by a phase field variable. The surface tension force is added to the Navier-Stokes equations as a body force by multiplying the chemical potential of the system by the gradient of the phase field variable [2].

The evolution of the phase field variable is governed by the *Cahn-Hilliard equation*, which is a *4th-order PDE*. The Phase Field application mode decomposes the Cahn-Hilliard equation into two second-order *PDE*s. For the level set method, the interface is simply convected with the flow field [2] [3].

The Cahn-Hilliard equation, on the other hand, does not only convect the fluid interface, but it also ensures that the total energy of the system diminishes correctly. The phase field method thus includes more physics than the level set method. The free energy of a system of two immiscible fluids consists of mixing, bulk distortion, and anchoring energy. For simple two-phase flows, only the mixing energy is retained, which results in a rather simple expression for the free energy.

The phase field method which is a special kind of diffuse interface method it stems from physical modeling. In diffuse interface (*DI*) methods, the infinitely thin boundary of separation

between twp immiscible fluids in the sharp interface limit is replaced by a transition region of small but finite width, across which physical properties vary steeply but continuously. The *DI* treatment can be motivated physically/thermodynamically or numerically as a regularization of the sharp interface limit. Anderson et al. mention three main advantages of diffuse interface (*DI*) methods. First, from a computational point of view, modeling of fluid interfaces as having finite thickness greatly simplifies the handling of topological changes of the interface, which can merge or breakup while no extra coding is required.

Second, the composition field has physical meanings not only on the interface but also in the bulk phase. Therefore, this method can be applied to many physical states such as miscible, immiscible, and partially miscible ones. Third, the method is able to simulate contact line motion as the contact-line stress singularity in the immediate vicinity of the contact line is removed. The most significant advantage in the present context is, however, that explicit tracking of the interface is unnecessary and all governing equations can be solved over the entire computational domain without any a priori knowledge of the location of the interfaces [2]. Phase field (*PF*) models can be considered as a particular type of *DI* models that are based on fluid free energy.

The basic idea is to introduce a conserved order parameter or phase-field ϕ, to characterize the two different phases. This order parameter changes rapidly but smoothly in the thin interfacial region and is mostly uniform in the bulk phases, where it takes distinct values φ_+ and φ_-, respectively. The interfacial location is defined by the contour level $(\varphi_+ + \varphi_-)/2$. The interface

dynamics is modeled by an evolution equation for φ, the Cahn-Hilliard equation.

$$\frac{\partial \varphi}{\partial t} + (u \cdot \nabla)\varphi = \nabla \cdot \left(M\nabla\mu_\varphi\right) \qquad (1.38)$$

Here, $M(\varphi)$ is a diffusion parameter, called the mobility. The chemical potential, μ_φ, is the rate of change of free energy with respect to φ and is given by

$$\mu_\varphi = \frac{d\psi}{d\varphi} - \varepsilon_\varphi^2 \nabla^2 \qquad (1.39)$$

For the bulk energy density $\psi(\varphi)$ different formulations are used in the literatures which depend on the choice for $\varphi_\pm$. Commonly used forms are examples.

$$\psi = \varphi^2(1 - \varphi^2) / 4 \; for \; \varphi_+ = 1, \; \varphi_- = 0 \qquad (1.40)$$

and $\psi = (\varphi + 0.5)^2 \, (\varphi - 0.5)^2 \; for \varphi_\pm = \pm 0.5.$ \qquad (1.41)

With equation *1.39,* Cahn-Hilliard equation *1.38* involves fourth-order derivates with respect to φ.

This makes its numerical treatment more complex as compared to the Navier Stokes equation which involves only second order derivates. The parameter ε_φ in equation *1.39* is a capillary width indicates of the thickness of the diffuse interface. The Cahn number $Cn \equiv \varepsilon_\varphi / L_c$ relates ε_φ to a characteristic macroscopic length L_c.

An important issue in the phase field method is the resolution of the interface thickness. Jacqmin used $\varphi_\pm = \pm 0.5$ and

defined ε_φ to be the distance from $\varphi = -0.45$ to $\varphi = 0.4$. He and Kasagi claimed that the phase field method allows the accurate calculation of two-phase flows on fixed grids with interfaces only two cells wide when $\varepsilon_\varphi = \Delta x$ is used. Zhou et al. achieved grid convergence when the grid size in the interfacial region is less than or equal to ε_φ. Yue et al. however, reported an interface thickness of approximately $7.5\varepsilon_\varphi$ so that about *10* grid points are required to resolve it. *Ding et al.* developed a *DI* method with the volume fraction as an order parameter and applied it to several two-phase flow test cases with large density ratio. The authors found that the method can accurately conserve global mass but requires rather many grid points to achieve a smooth variation of dependent variables in a sufficient narrow interfacial region.

The issue of mass conservation of the phase field method was studied in detail by *Yue et al.* for the case of a single drop in a quiescent fluid. While the phase-field variable was globally conserved, the drop could shrink spontaneously as φ shifted from its expected values in the bulk phases. The mass loss of the drop was proportional to both, the ratio between the domain and drop volume, and the Cahn number $Cn = \varepsilon_\varphi / R_0$, where R_0 is the radius of the drop.

The mass loss became negligible if Cn was small enough; recommended values are below *0.01*. Furthermore, it was found that there exists a critical drop radius R_c for a given computational domain size and value of ε_φ so that drops smaller than R_c eventually disappear.

1.4   Phase field for Two Phase Flow Microfluidics

To model the flow of two different, immiscible fluids, where the exact position of the interface is of interest, you can use the Two-Phase Flow, Phase Field application modes. It accounts for differences in the two fluids' densities and viscosities and includes the effect of surface tension and gravity [1] [2]. For incompressible fluids, the application mode uses the equations,

$$\rho \frac{\partial u}{\partial t} + \rho(u \cdot \nabla)u = \nabla \cdot [-pI + \eta(\nabla u + \nabla u^T)] + F_g + F_{st} + F_{ext} + F \qquad (1.42)$$

$$\nabla \cdot u = 0 \qquad (1.43)$$

$$\frac{\partial \phi}{\partial t} + u \cdot \nabla \phi = \nabla \cdot \frac{\gamma \lambda}{\varepsilon^2} \nabla \psi \qquad (1.44)$$

$$\psi = -\nabla \cdot \varepsilon^2 \nabla \phi + (\phi^2 - 1)\phi + \left(\frac{\varepsilon^2}{\lambda}\right)\frac{\partial f_{ext}}{\partial \phi} \qquad (1.45)$$

The four forces on the right-hand side of equation *1.42* are due to gravity, surface tension, a force due to an external contribution to the free energy, and a user-defined body force. The volume fraction of fluid *2* is computed as

$$V_f = min(max([(1 + \phi)/2], 0), 1) \qquad (1.46)$$

where the min and max operators are used so that the volume fraction has a lower limit of 0 and an upper limit of 1. The density is then computed by

$$\rho = \rho_1 + (\rho_2 - \rho_1)V_f \qquad (1.47)$$

and the dynamic viscosity according to

$$\eta = \eta_1 + (\eta_2 - \eta_1)V_f \qquad (1.48)$$

where ρ_1 and ρ_2 are the densities and η_1 and η_2 are the dynamic viscosities of fluid *1* and fluid *2*, respectively. The surface tension force is conveniently implemented as a body force:

$$F_{st} = G\nabla_\varphi \qquad (1.49)$$

where G is the chemical potential *(J/m³)*. In addition to the surface tension force, there is also a term that accounts for gravity. The gravity force is:

$$F_g = \rho g \qquad (1.50)$$

where g is the gravity vector. A force arising due to user-defined sources of free energy is computed using:

$$F_{ext} = \left(\frac{\partial f_{ext}}{\partial \phi}\right) \nabla \phi \qquad (1.51)$$

The mean curvature (m^{-1}) is computed by the following expression:

$$k = 2(1 + \phi)(1 - \phi)\frac{G}{\sigma} \qquad (1.52)$$

1.5   COMSOL Platform.

COMSOL Multiphysics provides an integrated workspace environment for the modeling and simulation of systems that involve the interaction of several physical phenomena. It allows the modeling of transport phenomena of mass, momentum and energy. It also allows the analysis of different physical systems involving both fluid phenomena, acoustic, electromagnetic.

COMSOL Multiphysics is a finite element analysis, solver and Simulation software / *FEA* Software package for various physics and engineering applications, especially coupled phenomena, or multiphysics. *COMSOL* Multiphysics also offers an extensive interface to *MATLAB* and its toolboxes for a large variety of programming, preprocessing and post processing possibilities. The packages are cross-platform (*Windows*, *Mac*, and *Linux*). In addition to conventional physics-based user interfaces, *COMSOL* Multiphysics also allows for entering coupled systems of partial differential equations (*PDEs*).

The *PDEs* can be entered directly or using the so-called weak forms (see finite element method for a description of weak formulation). Commercial finite elements (*FE*) based packages for various applications including computational fluid dynamics (*CFD*) is *COMSOL* multiphysics which was formerly known as *FEMLAB*. The Microfluidics Module brings easy-to-use tools for the study microfluidic devices and rarefied gas flows. Important applications include simulations of Lab-On-a-Chip (*LOC*) devices. In addition to enhanced interfaces for single phase flow, Microfluidics Module users will have dedicated interfaces for two-phase flow using the level set, phase field, and moving mesh methods. Each of these interfaces includes surface tension forces, capillary forces, and Marangoni effects. The chemical diffusion and reactions for dilute species interfaces included in the Module enable the simulation of processes occurring in lab-on-chip devices. For simulating rarefied gas flows, you can use the specialized boundary conditions that activate flow simulation in the slip flow regime. A free molecular flow interface using the fast

angular coefficient method allows for simulations where the molecular mean free path is much longer than the geometric dimensions. In addition, a dedicated user interface for transitional flow is included.

1.6   COMSOL verses other Platforms

The analysis of microfluidic systems is done via the use of software performing the iterative calculation of the differential equations that define the behavior of the system. Among the best known are *ANSYS, CFX*, Fluent, *KIVA, NUMECA, PHOENICS, STAR-CD, STAR-CCM* and *COMSOL* v*3.5a*. Although *ANSYS* and *COMSOL* offered an interface for coupling of electromagnetism with fluid flow and heat transfer, *COMSOL* provided a more flexible model setup as compared to *ANSYS*, though it required more memory.

The versatility, flexibility, and usability of *COMSOL* can easily be extended with its add-on modules as well as through manipulation of its underlying technical scripting language *COMSOL* Script or external programming language Math Works *MATLAB*. The library from the *ES* Module provides examples with arbitrary couplings to other application modules in i, such as complicated coupling analyses (*Li et al. 2006*). The user can also easily use the no conservative equation formulations for applications of convection and conduction in porous media in the *ES* Module. Furthermore, material properties source/sink terms, and boundary conditions can all be made arbitrary functions of the dependent variables during model design.

The *CAD* Import Module from version 3.5 supports the Para solid file format from Siemens *PLM* Software throughout the *CAD* import process, making it more robust and efficient than before as well as more compatible with third-party engineering and scientific applications.

Although *CAD* parts are not converted to *COMSOL* geometry objects as part of the import process, the user can individually repair and de-feature parts in an assembly, which gives additional flexibility when parts require different repair and de-featuring tolerances.

Furthermore, the robustness of the meshing process is substantially enhanced by meshing directly on the Para solid geometry representation. An advancing-front mesh generator creates higher quality meshes for *2D* and *3D* surfaces. Prisms and one-click hex-to-tet meshing and prism-to-tet meshing capabilities are possible options.

A swept meshing functionality using an *N*-to-*1* surface method makes meshing layered structures simple, fast, and easy.

Although *COMSOL* has the potential to solve any ground water problem associated with flow, heat transfer, and solute transport, if the desired model is not covered by predefined *PDE* templates, the user must be sufficiently knowledgeable of the physics of the problem as well as the theory of applied mathematics and finite elements to build a template.

Unfortunately, there is no simple way to overcome problems if fatal errors (e.g., Null Pointer Exception) are encountered during the building and debugging of the template.

The major advantages of *COMSOL 3.3* are its capacity to couple many different physics at a time as well as the capacity of building a parametric model using *COMSOL* script. It is to note that routines in *COMSOL* script are ready for optimization purposes. One of the drawbacks is its limitation in terms of memory and in solving huge models. It is an acceptable offset, except that the simulation on *COMSOL 3.3* was *30* times faster than *ANSYS*.

Chapter-2

The aim of this chapter is begin by computational modeling issue studies devoted to standard droplet generator for separation and segmented flow, bubble and drop formation, breakup and coalescence and then with increasing complexity in large scale microfluidic processors, bubble logic i.e. bubble to bubble hydrodynamic interaction provides an on-chip process control mechanism integrating chemistry and computation. This concept has been implemented using COMSOL multiphysics 3.5a software. These show the non-linearity, gain, bistability and programmability required for scalable universal computation.

Library of Computational Modeling for Microfluidic Circuit Design

2.1   Computational Modeling Issues

Before starting work on the logic gate in question has been taken into consideration and analyzed the signal generator to be used as input for the same. As such it was chosen the T-Junction, which was analyzed under various operational aspects and implemented in COMSOL environment, with various configurations, using the Phase Field computational method.

2.2.1 Physical Properties of the fluids

Two channels merge at a right angle. The main channel carries the continuous (or 'carrier') fluid and the orthogonal channel (hereafter 'inlet channel') supplies the fluid that will be dispersed (hereafter 'dispersed' or 'discontinuous' fluid).

The channels have rectangular cross-sections, and there are only three geometrical parameters that define the size and shape of the T-junction: the width w of the main channel, the width of the channel supplying the discontinuous fluid and the height h of the channels. The fluids used for the simulations were chosen as shown in the table *2.1*.

CONTINUOUS PHASE	DISPERSE PHASE
Ultra pure water	*Air*
	Hexadecane

Table. 2.1 Two Immiscible Fluids used in our Analysis

Especially, the simulation has been performed using Ultra pure water as continuous phase and disperse phase as Hexadecane with the organic solution consists of hexadecane (*Sigma-Aldrich*, viscosity η_o = *3mPas*) as the solvent and an oil-soluble surfactant (Span80, Sigma-Aldrich) at 2 wt %. The surfactant *Span80* has a neutral polar head and an unsaturated linear tail of *17* carbons, making it quasi-in-soluble in water, with a water/oil partition coefficient of *5.5x10⁻⁴* [5].

To compare the performs of the geometry for droplet formation and flow patterns, the simulation has been carried out by considering Air as a disperse phase and compared at the end of the section *2.13*. To make it more streamlined and flowing the treatment, it was decided to exhibit summarizes the parameters related to the physical and numerical simulations carried out and described below. The expressions of the two inputs of the device were.

Physical properties of Water:

Density of water $(\rho_W) -\ 1x10^3 \left[\frac{kg}{m^3}\right]$

Viscosity of the water $(\eta_W) - 1.95x10^{-3}\ [Pa*s]$

Physical properties of Hexadecane:

Density of Hexadecane $(\rho_H) - 773\ \left[\frac{kg}{m^3}\right]$

Viscosity of Hexadecane (η_H) - $3x10^{-3}[Pa*s]$

Physical properties of Air:

Density of air $(\rho_A) - 1.225 \left[\frac{kg}{m^3}\right]$

Viscosity of Air $(\eta_A) - 18.27x10^{-6}[Pa*s]$

Surface Tension:

Surface tension of water and air (σ_{WA}) -0.072 $\left[\frac{N}{m}\right]$

Surface tension of water and oil (σ_{WH})- $51.1x10^{-3}$ $\left[\frac{N}{m}\right]$

The Material/Coefficients Library is a framework for a number of extensible databases with properties for a broad collection of physical, elastic, electromagnetic, fluid, piezoelectric, and thermal properties of materials as well as heat transfer coefficients.

2.2.2 Numerical Properties

After the system has been fixed geometry and boundary conditions, defines all the physical and numerical parameters which allow modeling properly the microfluidic system. Among the many parameters there is, for example, the velocity of the two fluids in input, the surface tension, the room temperature atmospheric pressure. In the simulation of all cases were fixed logical constants listed in the following:

    a)   Reference Pressure (P) = 1 [atm]

    b)   Reference Temperature (T) = 293 [K]

If the velocity boundary condition, increase it gradually from zero to its actual value during a short initial time interval using the built-in Heaviside smoothing function *flc1hs* (*t-delta t, delta t*). In addition to the constants were set at the following numerical expressions for the velocity of the fluids

a) *Continuous phase (Q_1)* $= \dfrac{F_1 x\ 10^{-6}}{3600} * ramp\ \left[\dfrac{m^3}{s}\right]$

b) *Disperse phase (Q_2)* $= \dfrac{F_2 x\ 10^{-6}}{3600} * ramp\ \left[\dfrac{m^3}{s}\right]$

2.2.3 Input Profile

The flow profile explains the way in which the flow of a fluid behaves or is likely to behave in a pipeline based on its velocity and viscosity. Once this is known, it is possible to start to decide which of the many different types of flow meter available is best suited to the demands of the application. The term 'Flow Profile' is generally understood to refer to a vector diagram of the conditions within the pipe and an example is shown in figure *2.1*.

The main cause of the viscosity is an internal property of a fluid that offers resistance to flow. The degree to which the fluid resists flow in turn affects the velocity of flow through the pipeline. Imagine stirring a spoon in a bowl of water, for example. With nothing to impede it, the spoon travels quickly and easily through the water. Now imagine stirring honey, which is more difficult to stir because it has a higher viscosity than water.

The same applies to the flow of fluid through a pipe. As the level of resistance, or shear rate increases, the way in which the fluid behaves will change. By profiling the flow of a fluid through a pipeline, it is possible to find out how it behaves and from there to narrow down the choice of flow meters to those best able to cope with the conditions of the application. There are three types of flow, each of which is linked to the velocity of the fluid.

Laminar flow - Occurs at stable, low flow rates and is the most predictable type of flow. The fluid settles into streamlined tiers

which are prevented from merging by the viscous forces within the liquid and move in the same direction at a constant speed. Fully Developed Laminar Profile is parabolic in form see in figure *2.1*.

Transitional flow - Occurs when an increase in velocity causes distortions in the flow. This leads to mixing of the tiers within the fluid, resulting in the fluid exhibiting both laminar and turbulent characteristics at different points throughout the pipeline. The profile is unstable and complex- it may be parabolic as in laminar, flatter as in turbulent flow or a combination of both.

Turbulent flow – This type of flow occurs at faster flow rates. Mass distortions in flow result through the formation of eddies and whorls which themselves randomly fragment into smaller distortions, causing blending of the tiers within the fluid. Fully Developed Turbulent Profile is not fixed, but changes with the Reynolds number, approximating a flatter shape than the parabolic, as also shown in figure *2.1*.
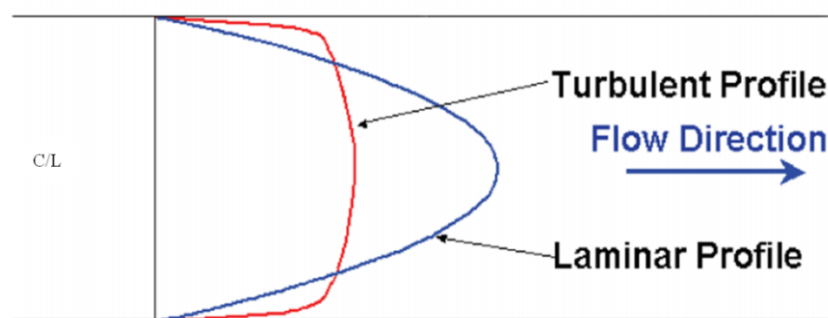

Figure. 2.1 Vector diagram to indicate the different types of flow

Once the Reynolds number is known it can be matched against a flow meter's Reynolds range to help pick the one that is best able to meet the demands of the application [1].

a)   *Re < 2000 = Laminar flow.*

b)   *Re lies between 2000 – 4000 = Transitional flow.*

c)   *Re >4000 or above =Turbulent flow*.

2.2.4 Input flow rates

The input flow rates which have been used in this computational model were described briefly in the following section *2.2*. The input flow rates estimated from set of computational modeling to achieve the range of flow rates to satisfy the logics.

CFD models	Input flow rates (µl/s)		Velocity (m/s)		Reynolds number		Capillary Number
	Phase-1	Phase-2	Phase -1	Phase -2	Phase-1	Phase-2	
And/or type -1	0.2	0.2	0.07	0.07	33.7	33.7	0.00027
And/or type-2	0.111	0.0889	0.0123	0.0098	55.35	11.36	0.000216
Not gate	0.056	0.041	0.00848	0.0062	102.5	3.993	0.000144
Toggle switch	0.1024	0.4	0.0102	0.044	19.18	5.55	0.000379

Table. 2.1. Input flow rates of computational models with reynold's, and Capillary number

2.2.5 Boundary Conditions

All the boundary conditions are applied for Two-Phase Flow, Phase Field application mode. The boundary condition used on the phase field function depends on whether the boundary is an inlet, an outlet, or a wall or symmetry boundary and inlets specifies the volume fraction of fluid *2*. The boundary conditions for the Incompressible Navier-Stokes application mode are grouped into the following types:

Wall is the standard and default boundary condition for a stationary solid wall. The *No Slip* condition prescribes that is, that the fluid at the wall is not moving. The motion of the interface on the boundary due to advection is zero and so the no-slip boundary condition is used in the momentum equation:

$$u = 0 \qquad\qquad (2.1)$$

The *Wetted wall* boundary condition is suitable for walls in contact with the fluid interface shows in red color of boundary condition as wetted wall of *135°*.

Initial Fluid Flow - To specify the initial position of the interface, use the Initial fluid interface boundary condition on interior boundaries. During the initialization step, the boundary condition sets the phase field function to *0*. For the transient simulation of the fluid flow, the boundary is treated as an interior boundary.

Inlet boundary condition offers two ways to specify an inlet velocity. The first is to set the velocity equal to a given vector u_0: $u=u_0$ the other is to specify a normal inflow velocity: $u = -nU_0$, Note that the boundary normal, n, points out of the domain.

Velocity - This boundary type contains different ways to specify conditions on a boundary where the fluid is supposed to enter the domain. Notice that the formulations contained in this boundary type all appear, some of them slightly modified, in the Outflow boundary type as well. Hence, there is nothing in the mathematical formulations that prevents a fluid from leaving the domain through boundaries where have specified the Inlet boundary type.

Outlet boundary type contains different ways to specify conditions on a boundary where the fluid exits the domain. Note that all of the formulations in this type can be found, possibly slightly modified, in other boundary types as well.

Hence, there is nothing in the mathematical formulations that prevent a fluid from entering the domain through boundaries where have set the Outflow boundary type. Setting outlet conditions for the Navier-Stokes equations is not a trivial task. A general rule of thumb, however, is that if there is something interesting happening at an outflow boundary, extend the computational domain to include this phenomenon.

Pressure, No Viscous Stress –This boundary condition specifies vanishing viscous stress along with a Dirichlet condition on the pressure:

$$\eta(\nabla u + (\nabla u)^T)n = 0, \ p = p_0 \qquad\qquad (2.2)$$

It is a numerically stable boundary condition that admits total control of the pressure level along the entire boundary. However, if the inflow is not normal to the boundary, this condition is an over specification. In case the solution turns out to have a non-normal inflow velocity, there are two choices. Either, move the boundary farther away to a location where the inflow is normal to the boundary or, use a stress type boundary condition.

Note that this condition is identical to the Pressure, no viscous stress condition for Outflow boundaries. Hence, depending on the pressure field in the rest of the sub-domain, a boundary with this condition can very well become an outflow boundary. The

black color shows the outlet of the boundary conditions where there is zero pressure and no viscous force.

The blue color shows the boundary type as inlet of the two T-Junction where the velocity has been applied. The yellow color shows the boundary condition where the expression of the velocity is applied. The pink color show the initial fluid flow of the fluids and to compute an initial solution respecting the contact angle, apply a Continuity condition on the interior boundary. Using the Initial fluid interface condition usually provides a smooth and physical interface faster than when using the Continuity condition shown in Table. *3.3*.
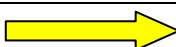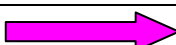
Settings	Colors	Conditions
Inlet		Laminar flow F_1 & F_2
Outlet		Pressure no viscous stress
Wall		Wetted wall
		No slip
Interior		Initial fluid flow
		Continuity

Table. 2.3. Boundary conditions.

2.2.6 Sub-domain Settings

The sub-domain settings describe the physics on a model's main domain, which is divided into subdomains and set different values for each sub-domain using settings of the following types:

a)   Coefficients that define the PDE on the sub-domain. The PDE coefficients are available for PDE modes and the weak form modes.

b)   Material properties, sources, and sinks that define the physics in the sub-domain. These properties are available in the physics modes and in the COMSOL Multiphysics modules. The software performs the translation into PDE coefficients automatically. It has been explained below.

2.2.7 Chip Geometry

In *COMSOL* Multiphysics can import and export *2D CAD* drawings on the *DXF* file format, a common format for *2D CAD* drawings. To create geometry for mesh generation and finite element analysis, *COMSOL* Multiphysics requires a high degree of accuracy within the *CAD* drawing. Sometimes the *DXF* geometries contain small gaps and exceedingly short edges that make it impossible to create a valid *2D* solid or a valid mesh.

COMSOL Multiphysics provides repair tolerance settings to remove short edges and close small gaps during *DXF* file import. The repair tolerance in *COMSOL* Multiphysics specifies the largest distance between the end points of curves allowed in the imported geometry. A *DXF* file contains groups of objects in different layers. This section provides a step-by-step example demonstrating how to use Boolean operations to combine solid objects. The Boolean operations can significantly speed up generating complex geometries. The following example shows how to create *2D* composite solids starting from primitive solids.

A solid object consists of an exterior boundary and an interior part. The boundary consists of edge segments. For example, a primitive solid rectangle has a boundary consisting of

four line segments and one sub-domain; a primitive solid circle has a boundary consisting of four circular arcs and one sub-domain.

Sometimes a solid object has interior boundaries that divide it into more than one sub-domain. Consider a square divided into four parts or subdomains. The subdomains can represent regions with different physics or material properties. It can also by inserting additional points and boundaries to control the mesh inside a solid object. All the geometry has been explained below.

2.2.8 Meshing

A mesh is a partition of the geometry model into small units of simple shapes. It is possible to create free, mapped, extruded, revolved, swept, and boundary layer meshes. The mesh generator creating free meshes, also referred to as the free mesher, and is the only mesher that can be used on all types of geometry objects.

For a *2D* geometry the mesh generator partitions the subdomains into *triangular* or *quadrilateral mesh elements*. If the boundary is curved, these elements represent only an approximation of the original geometry [3].

The sides of the triangles and quadrilaterals are called *mesh edges*, and their corners are *mesh vertices*. A mesh edge must not contain mesh vertices in its interior. Similarly, the boundaries defined in the geometry are partitioned (approximately) into mesh edges, referred to as *boundary elements*, which must conform to the mesh elements of the adjacent subdomains. If there are isolated points in the geometry, these also become mesh vertices.

Figure. 2.2. Example of creating refines mesh using COMSOL multiphysics 3.5a

When trying to solve a problem that does not converge, or having solved a problem where the solution does not seem properly resolved, there is often a need for re-solving the problem using a finer mesh. In these situations it is sometimes easier to refine the existing mesh than to regenerate the mesh from scratch using finer mesh settings.

It is only possible to refine free meshes containing triangular elements, or tetrahedral elements, in *2D* and *3D*, respectively. Techniques for computational analysis can be classified by the particular method with which these equations are discretized as finite difference, finite volume, finite elements and boundary elements methods.

Finite Element Method (*FEM*) enjoys many of the advantages of the finite volume (*FV*) method, most importantly the ability to handle unstructured grids and irregular geometries. The most significant advantage of the finite element method from the microfluidics's point of view is the relative ease with which the weak formulation allows for the application of boundary conditions and the extraction of boundary information [3].

This is particularly relevant for the flux or gradient-based boundary conditions commonly encountered in applied electrical fields, transport systems with surface phase reactions and thermal analysis involving convection heat transfer.
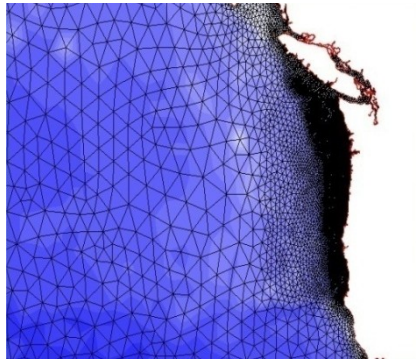
Figure. 2.3. Finite Element Method (FEM)

A disadvantages of finite element methods, consists in the numerical difficulties associated with handling highly irregularly shaped elements (e.g., large aspect ratios or highly curved) or large ranges in element size within a single mesh. In lab-on-chip devices, the relevant length scales can range over seven orders of magnitude, from double-layer thickness in (*nm*) to channel length (*cm*) and thus it is often difficult to avoid using such elements while maintaining a computationally traceable problem.

2.2   T-junction Computational Modeling (CM) for Droplet Generators

The two-phase microfluidics allows generating a motion to bubbles or drops inside the fluidic circuits. The formation of bubbles is done using particular geometries in which the fluid injected in the fluid "carrier", form initially a small drop that subsequently stretches until it breaks. This phenomenon is closely related to the effects of dynamic viscosity and to those of the

surface tension. The relationship between these two parameters is represented by the value assumed by the Capillary Number (*Ca*).

For low enough values of *Ca*, the forces acting on the surface of the droplet are balanced by the viscous forces, and it will be presented with elongated ellipsoidal shape, and with the major axis lies along the direction of maximum deformation; with values of more of *Ca* a certain critical value, the drop will not be a stable system, in fact the viscous forces will no longer be balanced by the surface, and it will be subject to the phenomenon of rupture and dragged fluid "carrier". It is useful to introduce the basic mechanism that breaks a liquid channel into droplets under the action of surface tension: the Rayleigh–Plateau instability.

(a)   *(b)*

(c)   *(d)*
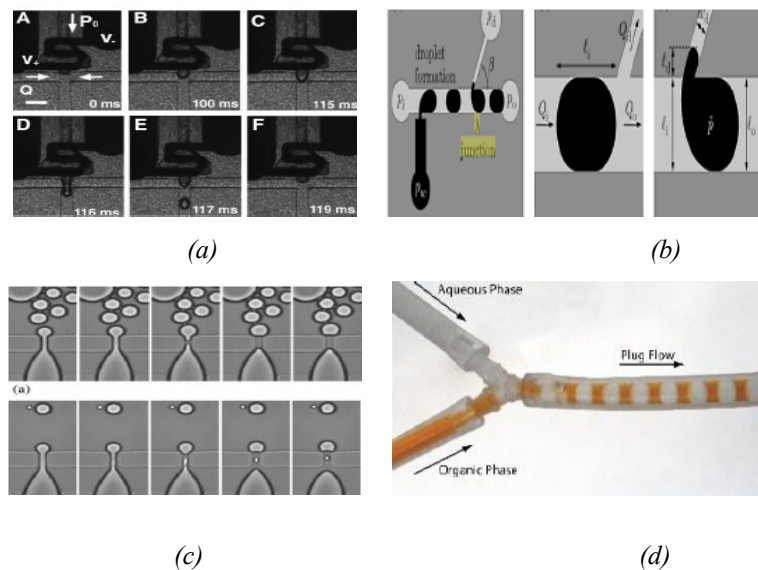
Figure. 2.5. (a) Generator of bubbles orifice. (b) Generator boils at λ-junction. (c) Generator boils at thermal resistance. (d) Generator boils at Y-junction.

A detailed review of this instability is given by Eggers. The instability is caused by pressure fluctuations inside the liquid due to small variations in the local curvature; such variations grow to

eventually break the liquid film into drops, through a so-called finite time singularity. Although the canonical analysis is done for a cylindrical fluid layer, the route to the singularity is quite general since surface tension causes the fluid in most cases to take the cylindrical geometry as it approaches the breaking point.

An understanding of the physical mechanisms is therefore useful whenever drop pinching occurs, as shown for example in figure *2.5*. In the case of the simple breakup of a liquid cylinder, one can obtain the wavelength of the first unstable mode from simple energetic arguments. This wavelength is $\lambda = 2\pi r$, where *r* is the radius of the unperturbed cylinder.

Indeed, the surface energy cost favors drop formation if the drop is large enough to reduce the total area of the interface. Although this is not the most unstable mode, experimental measurements show that the two modes are close, so that the perimeter of the channel gives a good approximation for the size of the bubbles. The formation of the bubbles can be achieved with different geometries such as:

a) T-junction;
b) Orifice;
c) λ-junction;
d) Y-junction.

2.2.1 Parametric CM

The T-junction is one of the most used for the formation of bubbles and is already being used in the production of emulsions in food, cosmetics and pharmaceutical products. The properties and the quality of an emulsion typically depend on the size and

distribution of the drops; the T-junction allows creating them in a uniform and easily controlling their production. A T-junction is nothing but a junction where they meet at right angles the two rectilinear channels that transport the two fluids.
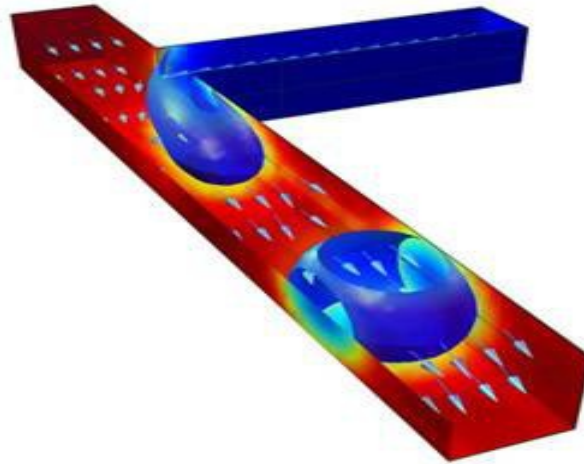
Figure. 2.4. Simulation of T-junction with bubble formation.

The formation of the bubble depends on the Ca but also by other parameters such as the volume fraction and therefore the reach of the fluids themselves. Perhaps the most popular microfluidic device used for the generation of droplets is a T-junction geometry in figure *2.6*, first incorporated into a microfluidic chip by Thorsen et al., and, subsequently used for formation of droplets and bubbles, for characterization of mixing in segmented liquid–liquid and liquid–gas flows, for formation of double emulsions and in a host of analytical applications. Most of these applications require precise control over the formation of the immiscible fluid segments.

COMSOL Model of Droplet breakup T-junction demonstration control, and developed an analytical understanding, of the

mechanism of break-up for a flow-focusing system generating micro-bubbles at low values of the capillary number. Generation of liquid drops in a flow-focusing setup has also been demonstrated and characterized.
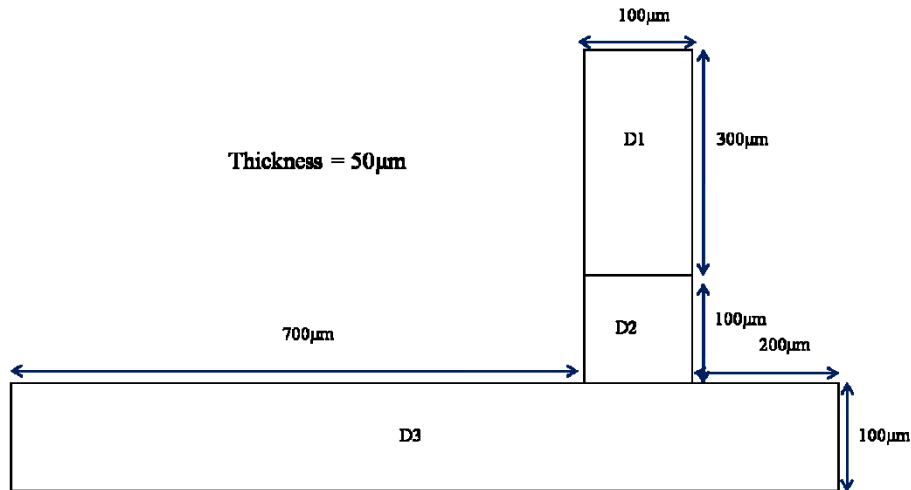
Figure. 2.6. COMSOL Model of Droplet breakup T-junction

Here the process of break-up and the scaling of the size of the discrete fluid elements produced in the T-junction geometries over a range of typical values of rates of flow and viscosities of the fluids. As a starting point of the study, after examining the example provided in the library of models, was carried out geometry to it inspired. Below are explained the steps followed for the design.

In figure *2.7*, shows the dimensions with which the device has been realized. It can be seen how the geometry is divided into three sub-domains: *D1*, *D2*, and *D3*. The different sub-domains are so set: *D1* with oil (dispersed phase), *D2* with water (continuous phase), *D3* with water (continuous phase). The constants, as well as the physical parameters for the two fluids and the numerical expressions have already been explained above. For the simulation were chosen: F_c= 0.4, F_d =0.2.
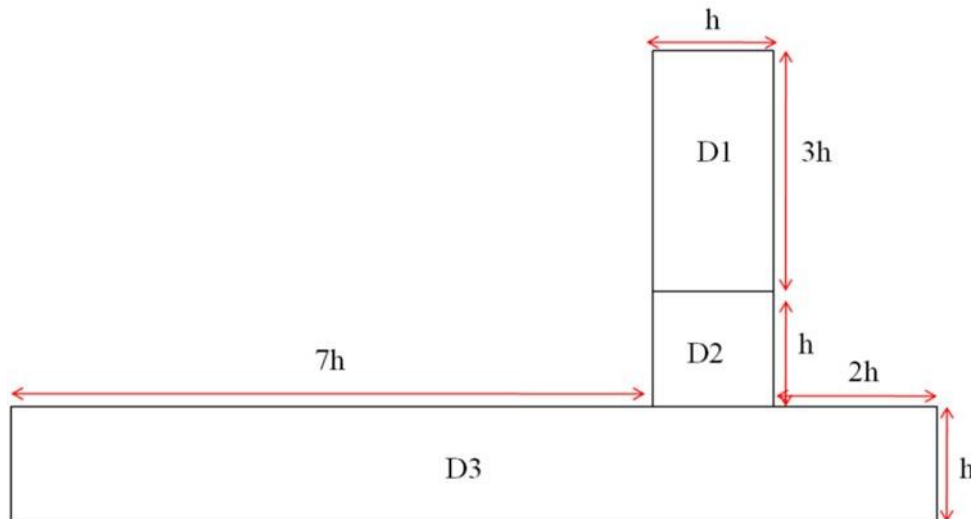
Figure: 2.7 Standard Geometry T-junction Bubble Generators

As a starting point of the study, after examining the example provided in the library of models, was carried out geometry to it inspired. In figure *2.7* shows the dimensions with which the device has been realized. It can be seen how the geometry is divided into three sub-domains: *D1*, *D2*, and *D3*.

The different sub-domains are so set: *D1* with oil (dispersed phase), *D2* with water (continuous phase), *D3* with water (continuous phase). The constants, as well as the physical parameters for the two fluids and the numerical expressions will be explained detail.

From this model have been deducted basic proportions for the realization of a general geometry T-Junction, and the order of magnitude of the flow rate at the inlet. Referring to what has been learned proceed to the realization of all devices of this type exposed in the rest of the discussion. Taking its cue from the lessons learned, the new geometry and it was done by a study of the mutual proportions between the two flow rates.
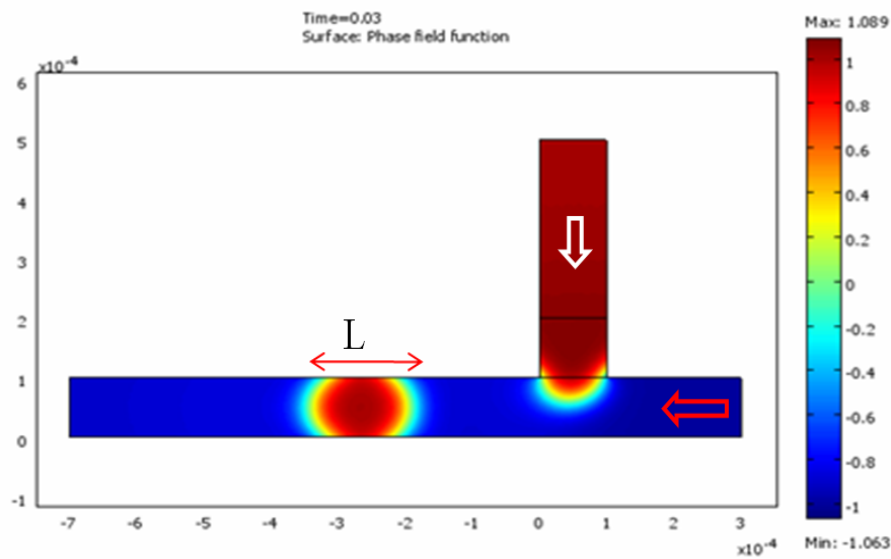
Figure. 2.8 it shows the interface between the two immiscible fluid and length L of the droplet.

Observing the geometric proportions expressed in the previous paragraph, is made up of a geometry having height *h* as *50μm* and width *w* as *50μm*. In this way the bubbles of hexadecane in water has been produced. Figure *2.2* illustrates schematically the geometry of a T-junction. Two channels merge at a right angle and the main channel carries the continuous (or 'carrier') fluid and the orthogonal channel (hereafter 'inlet channel') supplies the fluid that will be dispersed (hereafter 'dispersed' or 'discontinuous' fluid).

2.2.2 Parametric CM with Long Channel

Expanding on the above analysis, it was decided to evaluate the behavior of some devices with elongated channel than the standard size. For these tests were used two different geometries with the following characteristics and for each of the geometries, were evaluated in the channels of progressively increasing length has shown in the table *2.4* with constant thickness *50μm*.

Channel Length Constrains –The parametric computational model of the standard size has been demonstrated above. The long length of the channel is one of an important parameter which decides the shape of the bubble and makes different from the standard geometry, so the "*n*" parameter of the length of the channel has been changed for different values to understand the behaviors of the geometries but rest of the parameters were maintained.
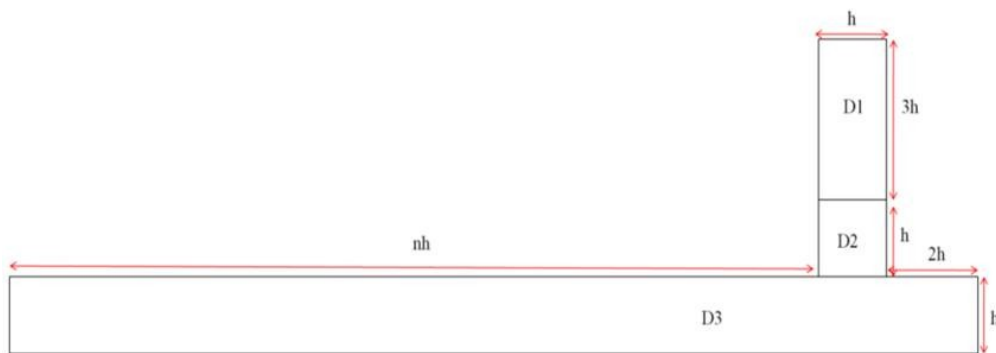
Figure. 2.9. Standard Geometry with long channel

Carrier Flow constrains **-** From the analysis of the elongated length of the channel two fundamental concepts of the T junction to perform the operation.

$$F_c = 2 * F_d \qquad (2.3)$$

h [μm]	Minimum F_{water} (m³/h)	μl/s	Maximum F_{water} (m³/h)	μl/s	ratio(f_w/h) min (μ)	ratio(f_w/h) max (μ)
Water-Hexadecane						
50	0.014	0.0038	2	0.555	0.000076	0.0111
100	0.026	0.0072	4.1	1.138	0.000072	0.0114
150	0.039	0.0108	6.1	1.694	0.000072	0.0113
200	0.052	0.0144	8.1	2.26	0.000072	0.0113
400	0.104	0.0288	16.3	4.52	0.000072	0.0113

Table. 2.4. Maximum and Minimum Continuous Phase F$_{water}$ for varies height as h in μm.

$$0.072 \times 10^{-3} < \frac{f_{carrier} \ [\mu L/s]}{h[\mu m]} < 11.2 \times 10^{-3} \qquad (2.4)$$

For these reasons, it is presented the need to determine the intervals of operation appropriate for the proper functioning of each individual device T-Junction. The steps taken to achieve the operating ranges within which can find a stable operating point for the devices has been shown.
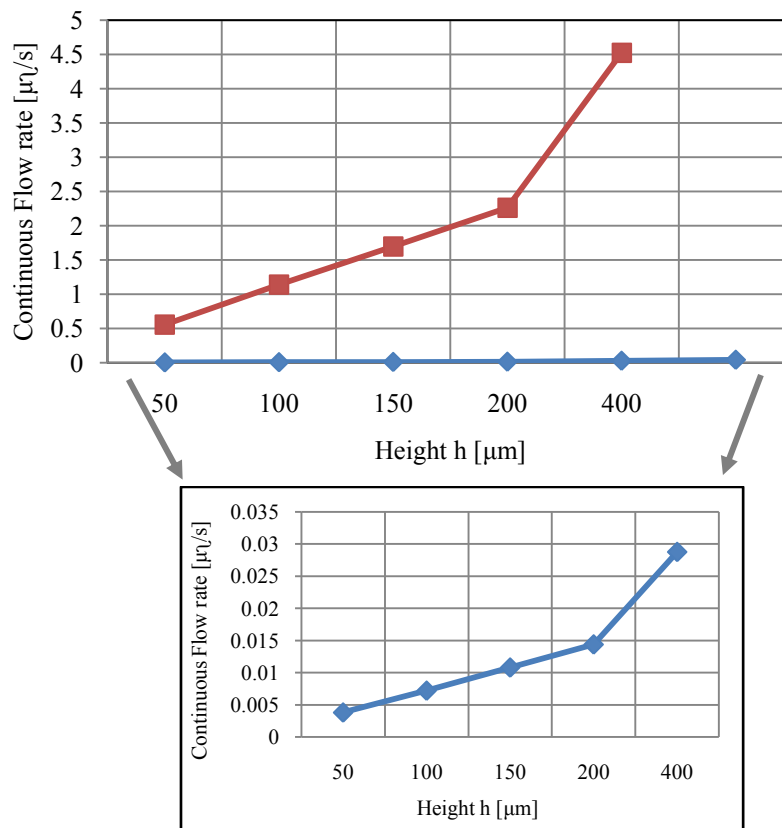
Figure. 2.10. Flow rates maximum which guarantee the formation of bubbles from well-defined contours in the different devices and shown and the flow rates that ensure the minimum break-ups in the different devices.

Tests were carried out on *5* different T-Junctions made up of using the proportions obtained previously: keeping the thickness constant and equal to *50μm*, has been changed the parameter *h* with

the following values. Through simulations, it has been determined the maximum and minimum values of the two flow rates for which the devices have a correct behavior. It takes account of the fact for all these tests, has been used in the proportion specified above.

The equation *2.4* is derived from the above mentioned simulations in table *2.4* which gives the ratio of minimum and as well as for maximum F_{water} approximately can be applicable for bubble formation in varies geometries. The figure *2.10* shows graphically that the flow rates maximum which guarantee the formation of bubbles from well-defined contours in the different devices as shown and the flow rates that ensure the minimum break-ups in the different devices.

Channel length constrains- From this study it was evidenced that the break-up occurs in the same conditions of T-Junctions standard. Since the lengthening of the channel (with a consequent increase of the hydraulic resistance), it was noticed that the bubbles tended to disappear along the path.

Water-Hexadecane							
h = 50μm							
Min f_w = 0.0038	Max f_w = 0.555						
n	Length L(μm)	$F_{water[\mu l/s]}$	m³/h	$F_{hexadecane\ [\mu l/s]}$	m³/h	Ratio $F_{water}/F_{hexadecane}$	Ratio F_{water}/L
7	350	0.0245	0.090	0.01225	0.045	2.00	0.00007
25	1250	0.0833	0.307	0.0417	0.154	2.00	0.00007
50	2500	0.1667	0.615	0.0833	0.307	2.00	0.00007
100	5000	0.3472	1.281	0.1736	1.02509	1.25	0.00007

Table. 2.5. Results of simulations for the channel height h = 50μm of "n" length μm.

Water-Hexadecane							
h =100μm							
Min f_w	0.0072	Max f_w	1.138				
n	Length L(μm)	$F_{water[μl/s]}$	m^3/h	$F_{hexadecane\,[μl/s]}$	m^3/h	ratio $F_{water}/F_{hexadecane}$	Ratio F_{water}/L
7	700	0.049	0.181	0.0245	0.090	2.00	0.00007
25	2500	0.194	0.718	0.0972	0.359	2.00	0.00007
50	5000	0.350	1.292	0.1750	0.646	2.00	0.00007
100	10000	0.778	2.870	0.6250	2.306	1.24	0.00008

Table. 2.6. Results of simulations for the channel height h = 100μm of "n" Length in μm.

Therefore the two set of simulation where worked out for height is *50μm* by varying the parameter length *"n"* and also for height *100μm*. it is worked on the values and the proportion between the flow rates for the permanence of the bubble up to the end of the channel using the equation *2.4* where the following results shown in figure *2.11* and *2.12* height *h* versus continuous and disperse phase in microlitre per second. It has been carried out with continuous phase fluid ultra pure water and disperse phase fluid hexadecane for varies length *"n"* a shown in table *2.5* and *2.6* elaborately.
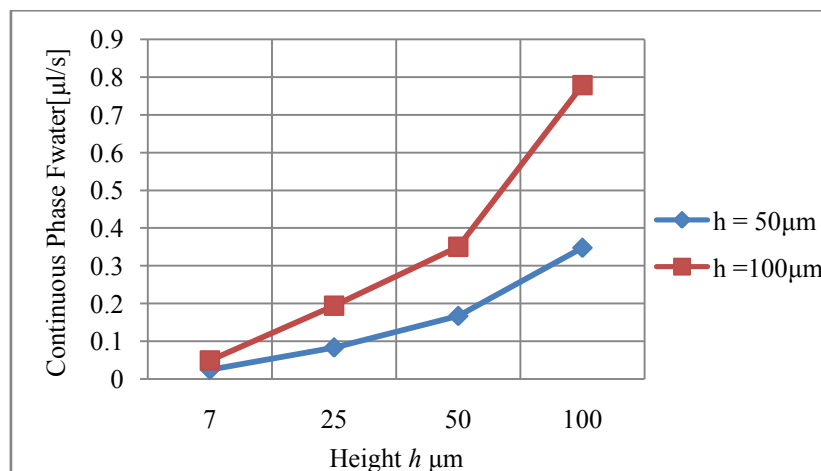
Figure. 2.11. Flow rate minimum of the continuous phase to vary the length of the channel for the permanence of the bubble.
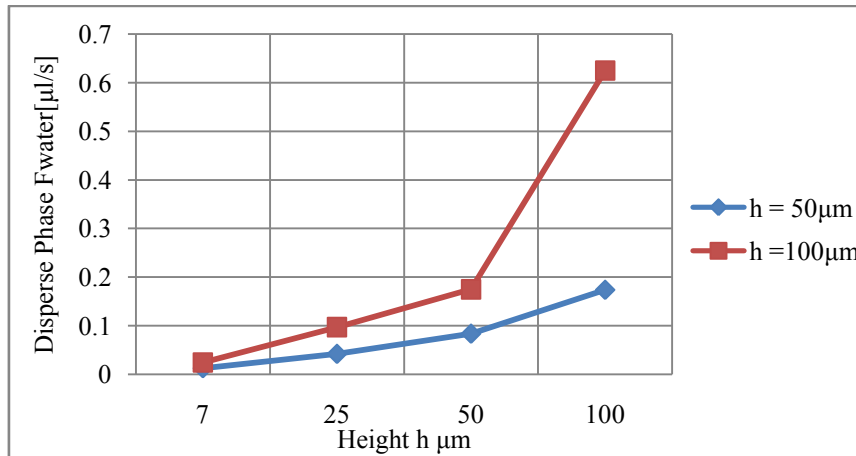
Figure. 2.12. Minimum flow rate of the dispersed phase to vary the length of the channel for the permanence of the bubble.

2.2.3 Flow Pattern Generation

The flow pattern has been described to see the effect of shear by varying the relative flow rates of the two liquids. A large array of ordered and disordered patterns were found, as shown in Figure. *2.13*. In addition to the flow focusing geometry, the T-junction has been used to form drops. In this flow, the drop forming fluid is injected slowly from the lateral-channel of the T into a stronger main-channel flow of the surrounding fluid.

The shear from the flow forces bubbles to shed from the junction with size depending on the relative flow rates [4]. For very low *Ca*, it is the size of the channels that determines the scale of the ejected drops, as in the case of a drop falling from a pipette. Similar systems to the one above were used for example by *Tan et al*. and *Yi et al*. Both groups demonstrate the ability to produce drops of a few microns, down to a fraction of a micron, as the main-channel flow rate, hence the local shear, is increased. The computational has been carried out by four different geometries for

20 different flow rates *(µL/s)* using water as continuous phase and air/hexadecane as disperse phase.
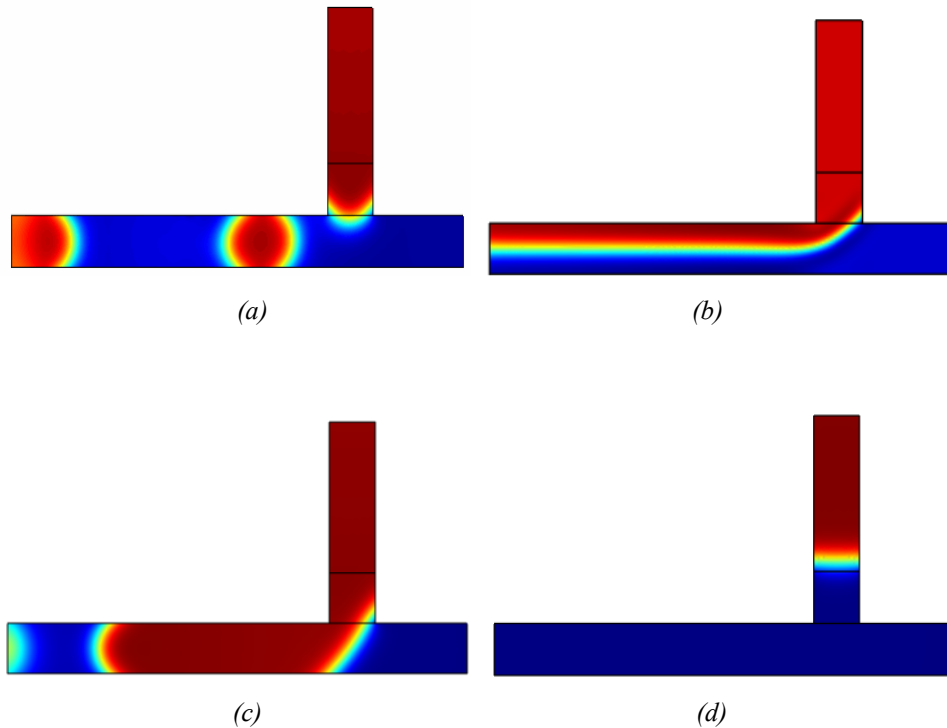
Figure. 2.13. Flow patterns of T-Junction for different flow rates (µL/s) (a) bubble pattern (b) laminar flow (c) slug formation (d) water flux.

Water-Hexadecane - For a discussion of the relation of two phases flow by changing the order of continuous and disperse phases see figure *2.14* where the continuous phase order increases and disperse phase order is less than the order 1, then the result were water flux with no droplet formation due to the fast flow of continuous than disperse phase as shown in blue color.

Contrarily, when the continuous phase order decreases and disperse phase order is greater than *1*, then the result were disperse flux with no droplet formation due to the fast flow of disperse than continuous phase as shown in black color. The bubble/droplet formations occurred especially when the order of the continuous phase and disperse phase is *0.01* for geometry which has height

50μm. The red color dot in figure *2.14* points the range of bubble/droplet formation due to the order of continuous and disperse phase.

The laminar flow reached when continuous phase is one order lesser than the disperse phase and vice versa. The slug formed when the disperse phase order is greater than the continuous phase. The figure gives an idea of the shifting behavior exactly for the given order of two phase starts from continuous phase flux, bubble/droplet formation, slug/plug formation, laminar flow, and disperse phase flux. The essential bubble/droplet, slug or laminar behavior lies between the region of water flux and oil flux based on the order of two phase flow.
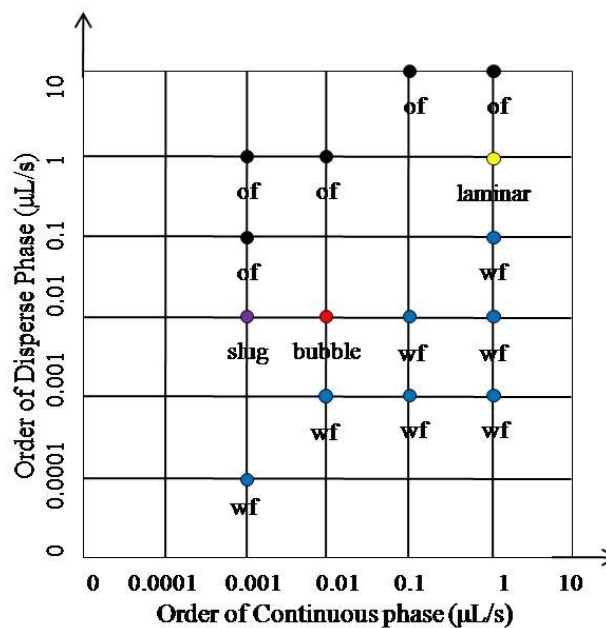
Figure. 2.14 Order of Continuous Phase versus Order of Disperse Phase for the geometry which has the height 50μm.

The relation between the geometries and the flow rate for bubble/droplet formation has been clearly shown in figure *2.15*. The simulation has been carried out by injecting ultra pure water as continuous phase and oil i.e. hexadecane as disperse phase for the

20 varies combination of flow rates in four different standard geometry using height *h* as *100μ - 600μm*. The bubble/droplet and slug formation achieved for all the geometries when the flow rate within the order of *0.001 – 0.1* flow rate *(μL/s)*. The pattern has maintained even for all the attempted geometries using the flow rates *(μL/s)*.

Flow continuous (μl/s)	Flow disperse (μl/s)	F_c (m³/h)	F_h (m³/h)	Height h in μm				
				25-50	100	150-200	400	500-600
0.0056	0.0056	0.02	0.02	bubble	bubble	slug	wf	Wf
0.0056	0.0556	0.02	0.2	slug	slug	slug	slug	Slug
0.0556	0.0556	0.2	0.2	bubble	bubble	bubble	bubble	bubble
0.0556	0.5556	0.2	2	laminar	laminar	laminar	laminar	Slug
0.5556	0.5556	2	2	laminar	laminar	bubble	bubble	bubble
0.5556	5.5556	2	20	of	of	of	laminar	laminar
5.5556	5.5556	20	20	laminar	laminar	laminar	laminar	laminar

Table 2.7. Various behaviors for the given height h of the geometries and the order of flow rate respectively.

The apparent behavior of bubble/droplet formation established at figure *2.15(a)* is based on the condition were the continuous phase (F_c) and disperse phase (F_d) are equal for height *h* less than *100μm*.

$$F_c = F_d \qquad (2.5)$$

When the disperse phase is less than the continuous phase by *10* gives the behavior of continuous flux for all the geometry as well as disperse phase is greater than continuous phase into *100* gives disperse flux behavior.

$$F_d < \frac{F_c}{10} \ \text{gives Continuous phase flux} \qquad\qquad (2.6)$$

$$F_d > F_c \ast 100 \ \text{gives Disperse phase flux} \qquad\qquad (2.7)$$
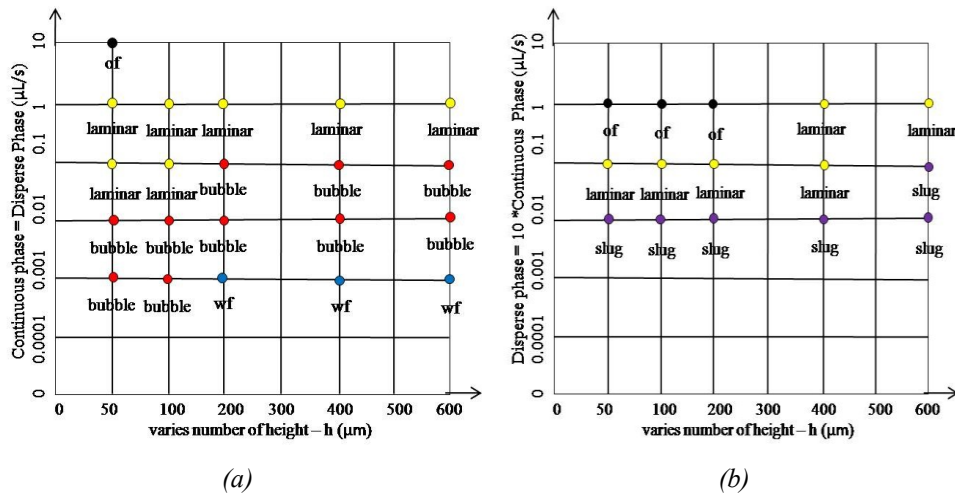
Figure. 2.15 (a) varies number of height versus $F_c = F_d$ and (b) varies number of height versus $F_d = 10\ast F_c$

$$F_d = 10 \ast F_c \qquad\qquad (2.8)$$

The figure *2.15(b)* has been plotted for the condition where disperse phase is equal to 10 times of continuous phase gives an appropriate behavior as slug pattern at the range *0.01 μL/s,* then shifts to laminar flow and reaches the oil flux at the end as shown for all geometries.

In the equation *2.8,* shows the pattern shifts from disperse phase flux (*of*), laminar flow (*laminar*), slug formation (*slug*) and finally gives the behavior of continuous phase flux (*wf*) for the given flow rates respectively. When the height is greater than *400μm,* the pattern starts from disperse phase flux and gives the laminar flow due to the geometry and at the last finish with continuous phase flux for the respected given flow rates.

Water-Air – The behavior of two phase fluids such as ultra pure water and oil i.e. hexadecane as already shown in the previous paragraph. The disperse phase is considered as air instead of hexadecane to compare and to understand the two different behaviors.

The shifting patterns were appeared as same as which starts from continuous flux (*wf*), bubble/droplet formation (*bubble*), and disperse phase flux (*of*). For height *h 50μm* the bubble/droplet formations occurred at the order of continuous and disperse phase as *0.1μL/s*.
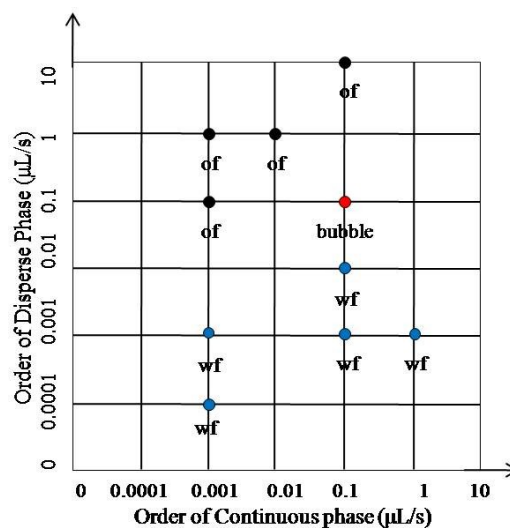
Figure.2.16. Order of Continuous Phase versus Order of Disperse phase for height h 50μm of the geometry.

The pattern shifting is demonstrated by applying the condition explained in the equation *2.5* and also shown in figure *2.17(a)* for particularly applied fluids especially when the height $h \geq 200\mu m$ gives the bubble/droplet formation at *0.01* to *0.1μL/s* and shifts to laminar flow instead at height *h* as 600μm, the bubble/droplet formation appeared at *0.1 to 1μL/s*.

—
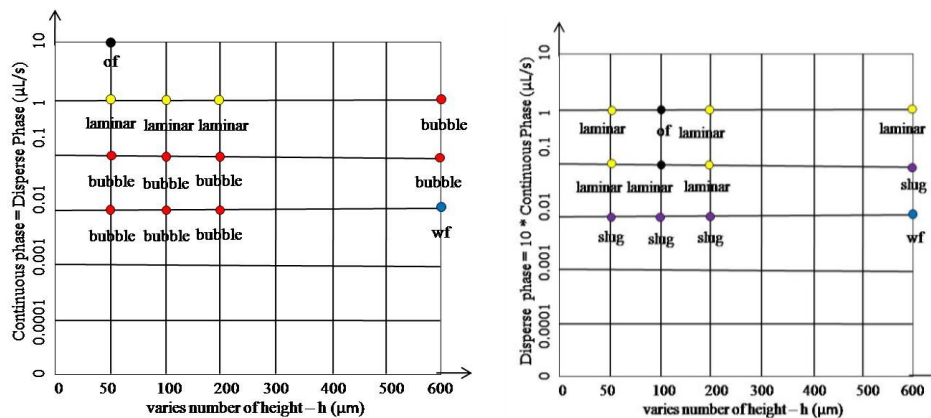
Figure. 2.17. (a) Increasing order of height versus $F_c = F_d$ and (b) Increasing order of height versus $F_d = 10 * F_c$

The figure *2.17(b)* has been illustrated for the condition explained in equation *2.8* gives the slug formation behavior at *0.01μL/s* for the increasing order of varies height *h μm*. Especially to mention in this context, at height *200μm* for the continuous phase as *20* and disperse phase *0.2* and *2* gives the same behavior as bubble flow.

Continuous Phase (F_c)	Disperse Phase (F_a)	h=50μm	h=100μm	h=200μm	h=600μm
20	0.2	wf	wf	bubble	wf
20	2	wf	wf	bubble	wf

Table. 2.7. Peculiar behavior of bubble/droplet formation for height h=200μm and the two phase fluids as water and air.

Bubble Dynamics-The droplet formation in two-phase microfluidic channel systems has been comprehensively studied for both immiscible liquid-liquid flows and gas-liquid flows in the above sections. Droplet formation was studied for various inlet conditions and the droplet size was compared with an analytical result known as the scaling law.

The gas phase was found to form bubbles, which are carried forward by the liquid phase for certain combination of flow rates for the gas and the liquid which has already explained in briefly in the previous section. The three practical aspects of bubble dynamics are examined in detail:

(i) The formation of drops and the dominant interactions depending on the geometry in which they are formed.

(ii) The transport of drops, namely the evaluation of drop velocity induced by the presence of the drop, the break up time, and the simulation time.

Continuous phase versus disperse phase - the study of bubble velocity has been carried out using two different geometry designed based on the height *h=50μm*, and *h=100μm* considering the two phase fluid of ultra pure water as continuous phase and hexadecane as disperse phase. The works were carried out in two stages:

a)   Variation of the flow-rate of the continuous phase (F_c), while keeping fixed the one of the dispersed phase (F_d).

b)   Variation of the flow-rate of the dispersed phase (F_d), keeping fixed the one of the continuous phase (F_c).

Water-Hexadecane					
Height – 50µm					
Continuous Phase (F_c)	Disperse Phase (F_d)	Break up time [s]	First bubble formed at Time [s]	Simulation Time[ms]	Velocity of the bubble [mm/s]
0.2	0.2	0.0114	0.0214	129	35
0.4	0.2	0.0096	0.0163	143	52.24
0.9	0.2	0.0128	0.0169	146	85.36

Table. 2.2. Result of Simulations of the channel height h-50μm for correct bubble break up
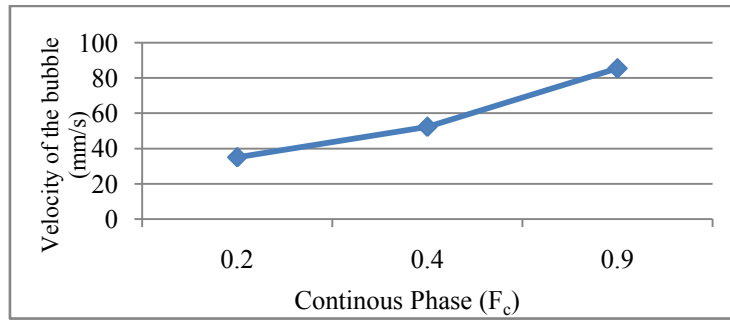
Figure. 2.18. Continuous phases F_c versus Velocity of the bubbles (mm/s) for height h=50μm

Water-Hexadecane					
Height – 50µm					
Continuous Phase (Fc)	Disperse Phase (Fd)	Break up time [s]	First bubble formed at Time [s]	Simulation Time[ms]	Velocity of the bubble [mm/s]
0.4	0.1	0.0215	0.0293	143	44.87
0.4	0.3	0.0072	0.0129	145	61.4
0.4	0.4	0.0063	0.0111	136	72.92

Table. 2.3. Results of Simulations of the channel height h-50μm for correct bubble break up
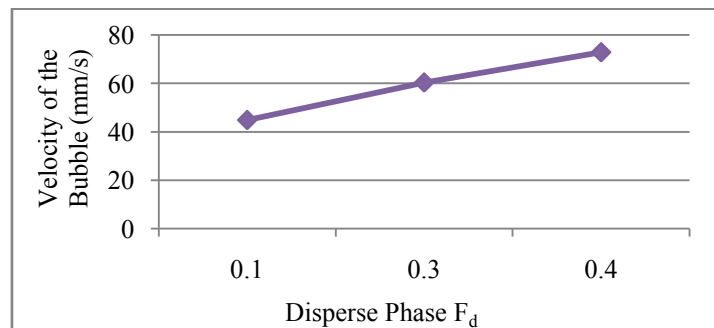
Figure. 2.19. Disperse phases F_d versus Velocity of the bubbles (mm/s) for height h=50μm.

F_c	F_d	*BREAK UP TIME* [s]	*TIME TO FIRST BUBBLE* [s]	*SIMULATION TIME* [s]	*VELOCITY OF THE BUBBLE* [mm/s]
0.02	*0.04*	*No break-up*	-	-	-
4	*2*	*No break-up*	-	-	-

Table. 2.5. Simulation Results where there is no break up for the bubble and a laminar flow

a)   The flow rate of the continuous phase must be greater than or equal to that of the dispersed phase. In particular, for optimum operation, it is chosen to set based on the equation *2.3*.

b)   Changing the order of magnitude of the flow rate, the same device is not working properly.

c)   Unbalancing excessively the ratio between the flow rates in favor of one of the dispersed phase, shows the condition of stratified flow on the other hand, do not get the break-up.

Water-Hexadecane					
Height – 100µm					
Continuous Phase (Fc)	Disperse Phase (Fd)	Break up time[s]	First bubble formed at time[s]	Simulation time [ms]	Velocity of the bubble [mm/s]
0.2	0.2	0.022	0.067	100	15.9
0.4	0.2	0.011	0.055	100	25
0.8	0.2	0.003	0.057	100	42

Table. 2.4. Results of Simulations of the channel height h-100µm for correct bubble break up.
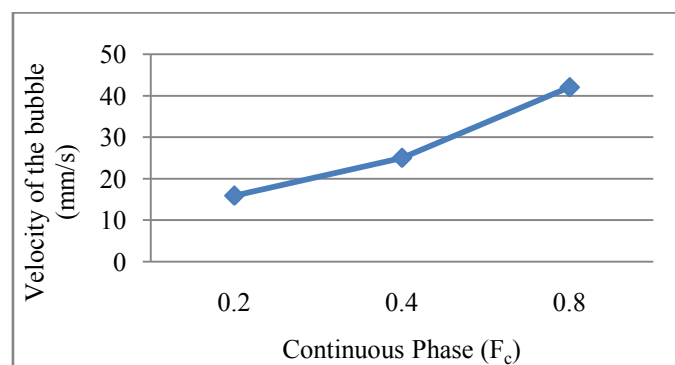
Figure.2.20. Continuous phases F_c versus Velocity of the bubbles (mm/s) for height h=100µm

Water-Hexadecane					
Height – 100µm					
Continuous Phase (Fc)	Disperse Phase (Fd)	Break up time[s]	First bubble formed at time[s]	Simulation time [ms]	Velocity of the bubble [mm/s]
0.2	0.2	0.022	0.067	100	16.4
0.2	0.4	0.0235	0.045	100	25
0.2	0.8	0.0645	0.0755	100	42.6

Table. 2.5. Results of Simulations of the channel height h-100µm for correct bubble break up
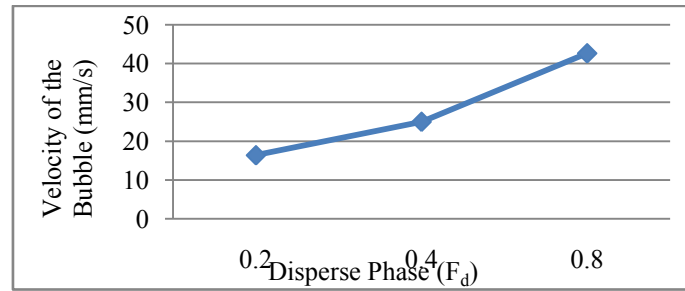
Figure.2.21. Disperse phases F_c versus Velocity of the bubbles (mm/s) for height h=100µm

2.2.4 CM Comparison: Water-Air Versus Water-Hexadecane

The two disperse phases air and oil i.e. hexadecane has been tested out by maintained water as continuous phase. The four standard geometries and the *20* different flow rates (*µL/s*) have maintained to see the variation of two disperse phases.

As in the previous section *2.1* the physical properties of two disperse phases has been explained that the density and viscosity of air is less than the oil i.e. hexadecane. The figure gives the idea that the points maintained the prototype. Nevertheless, the response of air compare to the hexadecane is tolerable to create bubble pattern to maintain the prototype of graph. But specifically the highlighted pink color points shows formation of weak air bubble flow that the response proves the prototype.

Common Behaviors of water-Hexadecane and water-Air							
Flow continuous (µl/s)	Flow disperse (µl/s)	$Fc(m^3/h)$	$Fh(m^3/h)$	h=50	h=100	h=200	h= 600
0.0056	0.0056	0.02	0.02	Bubble	bubble	slug	wf
0.0056	0.0556	0.02	0.2	Slug	slug	slug	slug
0.0556	0.0556	0.2	0.2	Bubble	bubble	bubble	bubble
0.0556	0.5556	0.2	2	Laminar	laminar	laminar	slug
0.5556	0.5556	2	2	Laminar	laminar	bubble	bubble
5.5556	0.0556	20	0.2	Wf	wf	wf	wf
5.5556	0.5556	20	2	Wf	wf	wf	wf
5.5556	5.5556	20	20	Laminar	laminar	laminar	laminar

Table. 2.6. Common Behaviors of water-Hexadecane and water-Air phase varies height h
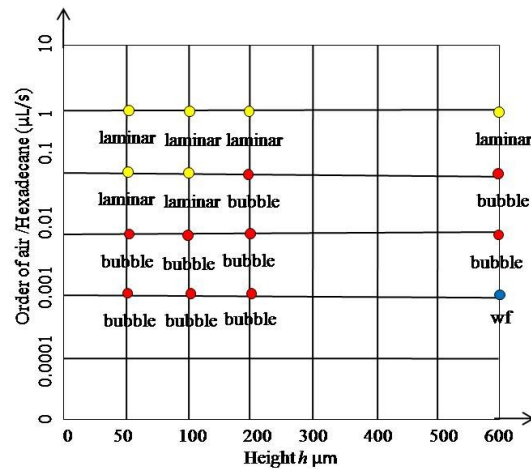
Figure. 2.22 Comparison of two different disperse phases

To complete the analysis, has been changed the fluid relative to the dispersed phase, in order to generalize as much as possible the results previously obtained. Therefore the hexadecane was replaced with air. Through the tests carried out, it was noted that the principle of operation of the devices remains unchanged. Furthermore, to achieve the same average speed of the bubbles along the channel, it is necessary to maintain a relationship between the flow rates such that:

$$Q_{1.2WH} \simeq 99\% \, Q_{1,2WA} \qquad (2.4)$$

The results obtained are expressed below from the table *2.2* and *3.1*:

F1 (CONTINUOUS PHASE)	F2 (DISPERSE PHASE)	BUBBLE BREAKUP TIME [S]	TIME OF FIRST BUBBLE [S]	SIMULATION TIME [S]	VELOCITY OF THE BUBBLE [mm/s]
0.202	0.202	0.0126	0.0225	162	44.87
0.404	0.202	0.0108	0.0175	135	61.40
0.404	0.404	0.0064	0.0112	132	72.92

Table. 3.1. Results of simulations with water and hexadecane
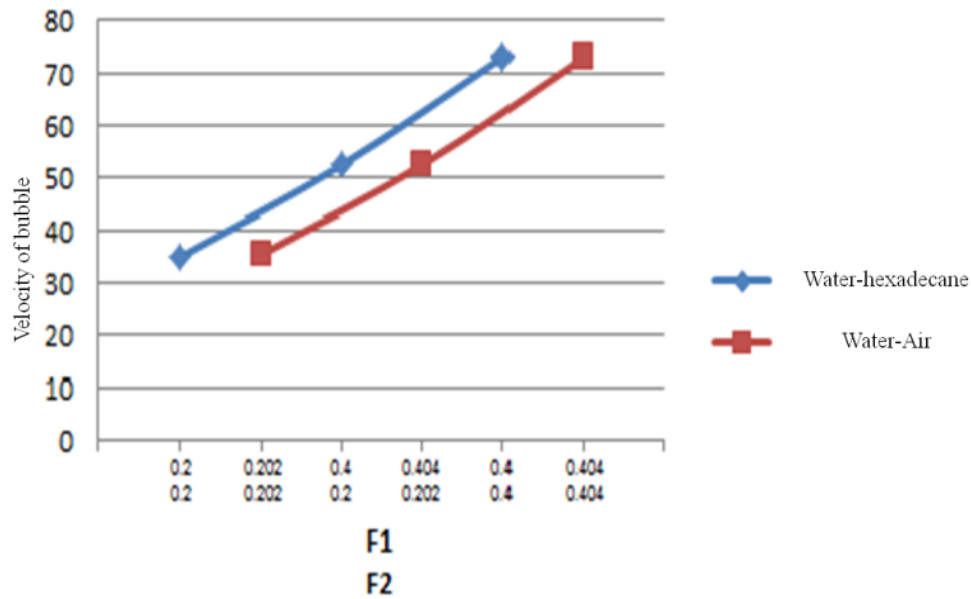
Figure. 2.23. Comparisons between the (F_1 & F_2) water-hexadecane and Water-Air versus Velocity of bubble

2.3   Bubble Logic

Nonlinearity is introduced into an otherwise linear, reversible, low–Reynolds number flow via bubble-to-bubble hydrodynamic interactions. A bubble traveling in a channel represents a bit, providing us with the capability to simultaneously transport materials and perform logical control operations. These show the nonlinearity, gain, bistability, synchronization, cascadability, feedback, and programmability required for scalable universal computation. With increasing complexity in large-scale microfluidic processors, bubble logic provides an on-chip process control mechanism integrating chemistry and computation [5] [8] [9].

However, pneumatic elastomeric micro valves require external macroscopic solenoids for their operation, and cascadability and feedback are currently lacking in microfluidic control architectures. Several reaction chemistries have been

implemented in segmented-flow two-phase micro-reactors, where individual nanoliter droplets traveling inside microchannels are used as reaction containers.

Figure. 2.24. Bubble logic devices

On-chip droplet management requires external control of individual gates. Devices that exploit the dynamics of droplets inside microchannels would make high-throughput screening and combinatorial studies possible, but passive techniques have not provided control over individual droplets. The bubble logic demonstrates that implements universal Boolean logic in physical fluid dynamics. This provides a droplet-level, internal, inherently digital flow control mechanism for microfluidic processors.
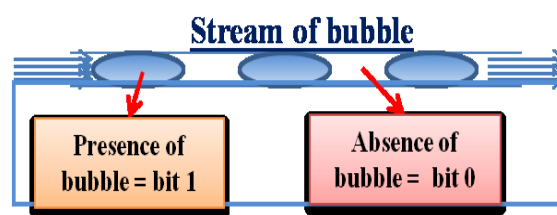
Figure.2.25 Stream of bubble

A bubble traveling in a microchannel can represent a bit of information as well as carry a chemical payload, making it possible to integrate chemistry with computation for process control. Bubble logic preserves the information representation from input to output; thus, devices can be cascaded, allowing implementation of combinatorial and sequential Boolean logic [6] [8] [9]. A bubble

can be transported to a desired location in a complex microfluidic network via a series of logic gates corresponding to an equivalent Boolean circuit. Purely hydrodynamic fluidic logic was used to build a trajectory controller, an all-fluidic display, nondestructive memory, and a simple computer.

Because the high Reynolds numbers required for inertial interactions cannot be maintained in the microscopic geometries needed for higher operating speeds and increasing integration, fluids with non-Newtonian polymer additives have been used to realize a constant flow source and a bi-stable gate.

Boolean logic in a Two-phase Newtonian fluid was implemented by changes in flow resistance. Bubble logic, based on hydrodynamic bubble-to-bubble interactions, is more similar in bit representation to theoretical billiard ball logic based on the elastic collision of particles [5].

These schemes all conserve information, because during logic operation a bit is neither created nor destroyed. The pressure-driven flow of bubbles in an interconnected microfluidic network can be described with a simplified dynamic flow resistance model.

The pressure drop due to a long bubble flowing in a channel, where the bubble radius in an unbounded fluid is greater than the channel width and the continuous phase completely wets the channel surface, is nonlinear. For small flow rates, this increased flow resistance is primarily due to viscous dissipation in the thin film of liquid surrounding the bubble [6] [8][10].

With the presence of surfactant molecules on the air-water interface, viscous dissipation in the lubrication film further

increases as a result of the no-slip boundary conditions at the interface.
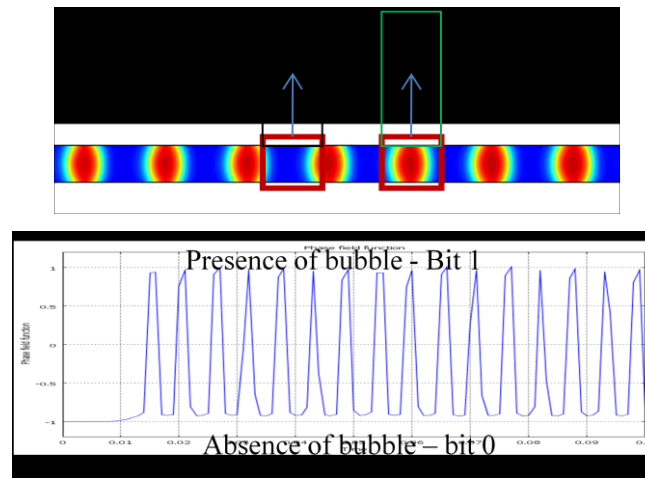
Figure. 2.26. Bubble bit Representation (up) and the graph of bit representation (down).

In this case, the pressure drop across a finite-length bubble is also linearly dependent on the bubble length until it reaches a critical value, beyond which it is constant. When a bubble traveling in a microchannel arrives at a bifurcation with low capillary number (where the bubble does not split because surface tension dominates the viscous stress), it chooses the branch with highest instantaneous flow.

With an increased flow resistance due to the presence of a bubble in a microchannel, flow lines in surrounding interconnected channels can be perturbed. The nonlinearity in such a system arises from the introduction of interfacial force terms from the boundary conditions due to the presence of a free surface at the fluid interfaces. These nonlinear time-dependent interactions are the basis of our bubble logic gates. In the implementation oil bubbles has been produced in water (continuous phase). It has been explained *AND/OR/NOT* gates using two different geometries and a toggle flip-flop by applying bubble logic below. The modulators

program the device by producing a precisely timed sequence of bubble/droplets, resulting in a cascade of logic operations within the microfluidic channel sequence, exploiting the control of the path of the generated bubbles.

The aim is to build a consistent computational fluid dynamics model of the process modeled by Navier Stokes Equation and phase field formulation to track the interface between the two fluids [10].

These are the input flow rates of two phase fluids applied in *AND/OR* gates. On one hand water and hexadecane fluids input range lies in *0.02-0.2* to provide the bubble/droplet formation, on the other hand water-air fluids input range lies in *0.02-2*. The logic gates have been proved with these flow rates is suitable to satisfy the bubble logic.

Water-Hexadecane-T-junction					
Flow continuous (µl/s)	**Flow disperse (µl/s)**	**Fc (m³/h)**	**Fa (m³/h)**	**h=50µm (And-Or-I)**	**h=100µm (And-Or-I)**
0.0056	**0.0056**	**0.02**	**0.02**	bubble	bubble
0.0056	0.0556	0.02	0.2	slug	slug
0.0556	**0.0556**	**0.2**	**0.2**	bubble	bubble

(a)

Water-Air-T-junction					
Flow continuous (µl/s)	**Flow disperse (µl/s)**	**Fc (m³/h)**	**Fa (m³/h)**	**h=50µm (And-Or-I)**	**h=100µm (And-Or-I)**
0.0056	0.0556	0.02	0.2	slug	slug
0.0556	**0.0556**	**0.2**	**0.2**	bubble	bubble
0.5556	**0.5556**	**2**	**2**	bubble	bubble

(b)

Table. 3.2. Input flow rates applied in AND/OR Gate which has height h= 50μm and 100μm

2.3.1 Computational modeling for the AND/OR Logic Gates-1.

As has already been mentioned in the introduction of this elaborate, one of the main applications of microfluidic today concerns the realization of "Lab-on-a-chip": these are devices that allow achieving, in a single chip of a few millimeters, operations (such as synthesis, separation, analysis, etc) which would have required the use of several laboratories.

One of the limitations of Lab-on-a-chip is the need to use, for the various operations for control architectures of macroscopic externals such as pneumatic valves, pumps, syringes, computers. however, in continuous development study of a digital logic microfluidics, said "bubble logic" or logic in bubbles, whereby it is possible to realize a system of internal control of flows and of individual bubbles in the devices microfluidics.

The logic bubble, and microfluidic circuits that are based on this logic, will be the main topic of this chapter, after an introduction to digital logic electronics. The microfluidic *AND/OR* Gate in figure 3.6 is a microfluidic device experimental proposed by the two engineers Manu Prakash (*Cambridge, MA* (*USA*)) and Neil Gershenfeld (Somerville, *MA* (*USA*)). The computational model and the meshing type of the computational model and the logic cases were explained in the following sections.

Benchmark Experimental Model - This is where the reference is made for the realization of the *CFD* model. With this design, for which has been employed water, as fluid "carrier", and nitrogen for the bubbles, is able to simultaneously implement the logical operations *AND & OR*.

The geometry is planar, the thickness of all channels is equal to 7μm, and instead their length is not explicitly indicated. As regards the width of each channel, that of the channels *A* and *B* measure *5μm*, that of channel *A+B* is equal to *65μm*, while the width of the channel *A·B* size *4μm [6]*.

Channels *A* and *B* receive in input a constant flow of water (with a 2% surfactant "*Tween 2*" in solution) via syringe pumps. The flow rate of the inlet water is equal to *Q=l.25μL/s*, the surfactant is used to stabilize the interfacial surface of the bubbles which will form. Therefore mentioned bubbles are generated thanks to a geometry T-junction.

For the generation of the same is used nitrogen at a constant pressure of *0.5psi [6]*. The evaluation of the behavior of the logic gate was made by requiring two inputs the flow rate *QA = QB = 0.25 μL/s*: When a single bubble, from channel A or channel B, reaches the central joint of the logic gate, will flow into the exit channel with the greatest flow instantaneous. In this case, therefore, the bubble will cross the channel *A+B*. In the case in which two bubbles, from *A* and *B*, simultaneously reach the central joint, there will be one that will flow through the channel *A+B*, while the other will flow through the channel *A·B*.

INPUTS		OUTPUTS	
A	B	AND	OR
0	1	0	1
1	0	0	1
1	1	1	1

(a) (b) (c)
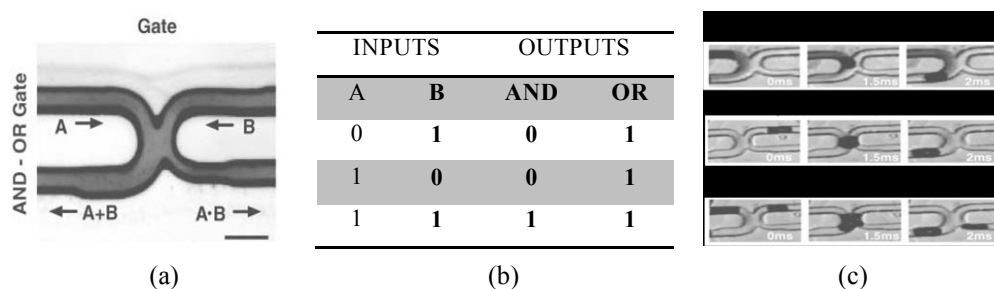
Figure. 2.27. (a) AND/OR Gate (b) Truth Table of AND/OR Gate (c) Logic Cases

In general, the bubble that comes in advance at the central joint always take the channel *A+B* (as the latter presents less resistance to flow), increasing the hydrodynamic resistance of the same and pushing the other bubble at the channel *A·B*. In any case, two bubbles coming from the input channels only interact if arrive at the junction with a delay $\tau_0 \sim 0.5ms$ relative to one another. All cases logic for this microfluidic device to bubbles is summarized in figure *2.27*.

It is recalled that the logical value *1* corresponds to the presence of a bubble in the channel, while the logical value corresponds to the absence of bubbles.

Meshing - The mesh applied in this geometry is extended mesh has number of degree of freedom is *49463*. The *2D* domain of the *AND/OR* logic is discretized using an unstructured finite element grid with *5520* elements using sub-domain mesh parameter method as triangular. The base mesh of number of mesh point is *3043*.

Figure. 2.28. Refined Meshing of the Geometry

Geometry properties – The first step towards the realization of the computational model is certainly the implementation of AND/OR gate geometries are:

➢ AND/OR gate geometry height-*50μm*

➢ AND/OR gate geometry height-*100μm*

Referring to the measures outlined in the Patent for the logical port microfluidics. The two T-junctions at the top of the model produce a train of input air bubbles considering flow rate for height *50μm* and *100μm* of water and air respectively of *0.25μL/s & 0.0038μL/s* and *0.864μL/s & 0.307μL/s*.

(a)

(b)
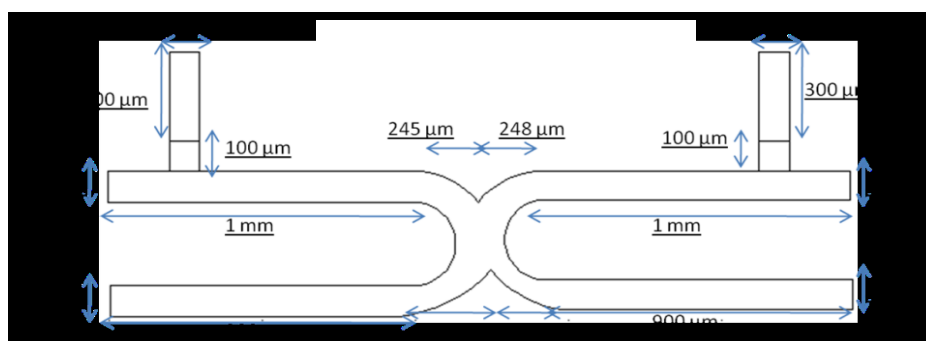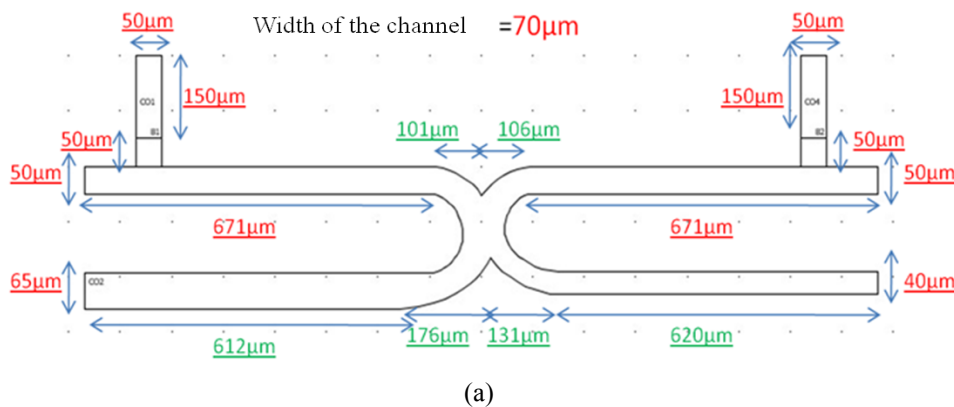
Figure. 2.29. Geometry of the AND/OR gate universal computation (a) height h=50μm (b) height h=100μm

All measurements are given in microns. Only those in red were however detected by the Patent [9] of the microfluidic device

in question. The same document also lacks the details of the two T-junction. To size the rest of the geometry, has made reference to the illustrations, which are present in the same Patent, obtaining the missing measures through proportionally. To obtain the correct functioning of the computational model, the geometry has been divided into *5* sub-domains as shown in the following images. The *AND/OR* logic gate which has height *h=100μm* has designed with assumptions to compare the behavior and the response of the two geometries.

The universal computation *AND/OR* gate type-I is designed using the concept of standard geometry which has the thickness of the geometry and the width of the geometry is *50* and *100μm²* respectively. The two different colors represent the fluids that have been used in the simulation of the logic gate: water in blue as fluid "carrier", and air in red for the bubbles.

By setting the water as fluid*1* and air as fluid*2*, the *5* subdomains have been configured in the following manner *D1*, *D2* and *D4* set has water flow and *D3* and *D5* has air.
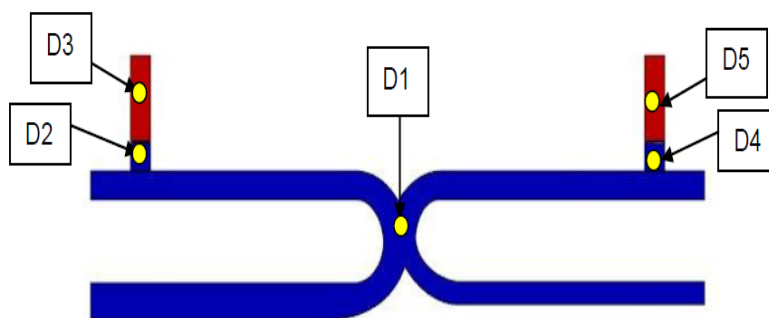
Figure. 2.30. Subdomain settings of AND/OR gate universal computation

Logic Cases - The produced train of bubbles always enters in the *OR* gate (+) which has a channel wider with less resistance than the

AND gate (·) and therefore directing a bubble arriving later to the former gate (·). The output signal from one gate to perform as an input signal for many gates can be realized by splitting bubbles at the center of the geometry.

For each case, the values acquired by the phase field variable allow to detect the presence of disperse/continuous phase represented by a bit *1/0*. Looking at the contour of air bubble, the signal shows when there is presence of air bubble by increasing its amplitude, and vice versa when there is no bubble. The following four cases are detected through the simulations:

Case: 0-0 input flows have been set at *A&B=0*, that produces no bubbles and gives the output at *OR & AND* as '*0*'. The phase-field graph confirms that in all the *4* point it is '*0*' indicating no passage of bubble.

Case: 0-1 When the bubble travelling in a microfluidic channel arrives at a bifurcation with low capillary number (where bubble does not split because surface tension dominates the viscous stress), it chooses the branch with highest instantaneous flow. With an increased flow resistance due to the presence of a bubble in a microchannel, flow lines in surrounding interconnected channels can be perturbed. The non-linearity in such a system arises from the introduction of interfacial force terms from the boundary condition due to the presence of a free surface t the fluid interface [6].

These non-linear times dependent interactions are the basis of bubble logic [6] [10]. In case *0-1*, the input flows have been set as *A=0 & B=1* producing a bubble at time *t=1.7ms* from T-junction

(B) and giving the output at *AND=0 & OR=1* as a passage of bubble in *OR* gate at time *t= 4.3ms* as shown in figure *4.0(c)-(d)*. The phase field graph explains that there is an input at *B* and output at OR with a sinusoidal signal confirming the dynamics.

Case: 1-0 input flows have been set as *A=1 & B=0*. This produces a bubble at time *t=1.7ms* from T-junction *(B)* and gives the output *AND=0 & OR=1* meaning passage of bubble in *OR* gate at time *t= 4.3ms* as shown in figure *2.31(e)-(f)*. The signal of the phase field graph can be always representative of the dynamics.

Case: 1-1 - *AND/OR* bubble logic gate that evaluates both *AND* (.) and OR (+) simultaneously as in necessary to satisfy bit conservation. The first bubble arriving at the junction always enter *A+B (OR)* (wider channel with less resistance), increasing the output flow resistance of *A+B* and thus directing a bubble arriving later to *A·B (AND)*.

In case *1-1*, the input flow has been set as *A=1 & B=1*. This produces a bubble at time t=1.6ms from both T-junction *(A&B)* giving the output *AND=1 & OR=1* at time *t= 4.2ms* as shown in figure *2.31(e)-(f)*. The phase field graph explains with a sinusoidal signal that there is an input at *A & B* and output at both *OR & AND* gate as a passage of bubble.

A

B

AND

OR

(a)
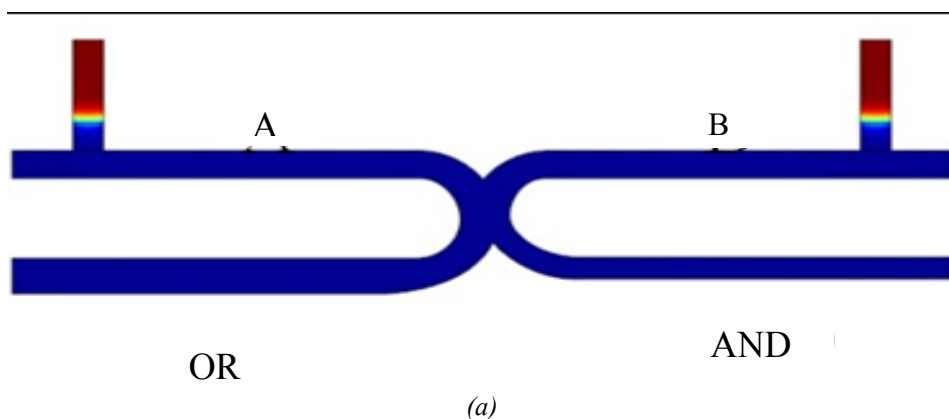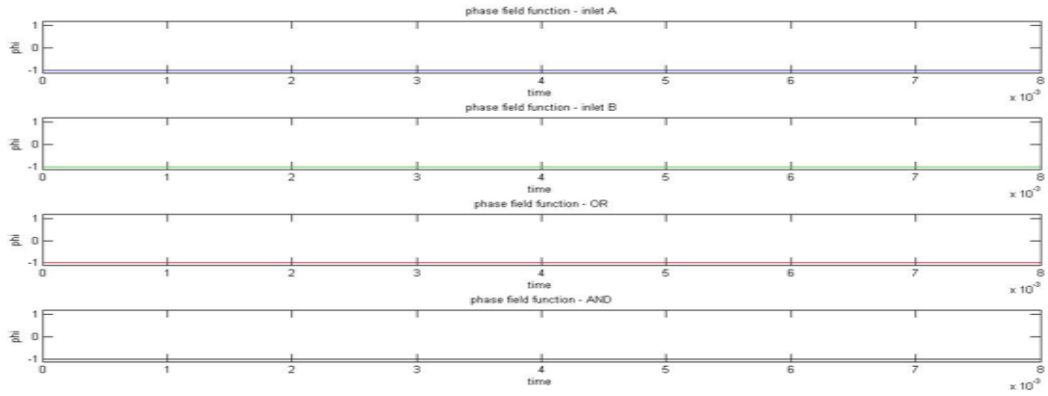
(b)
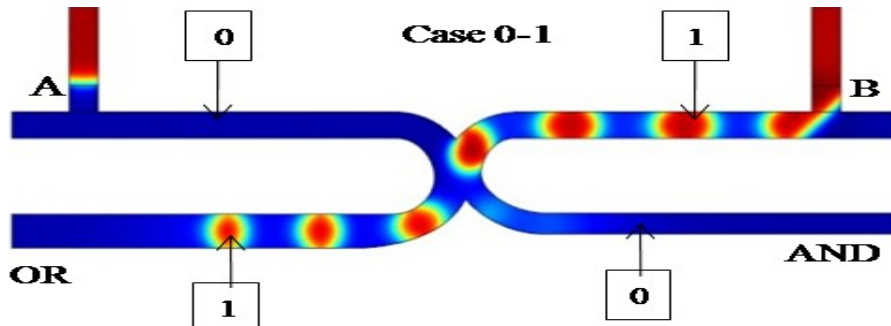
(c)
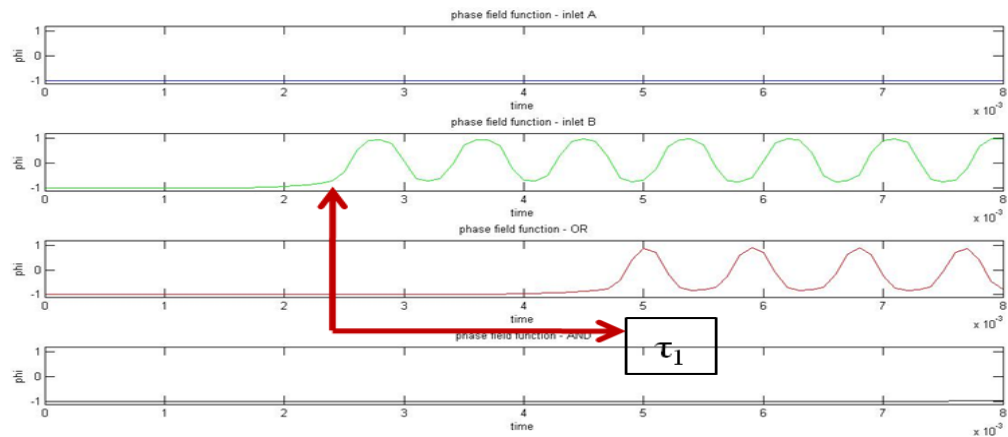
(d)
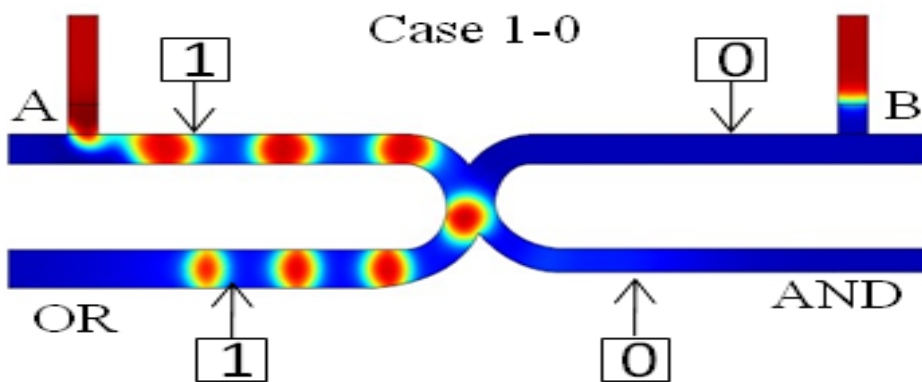
(e)
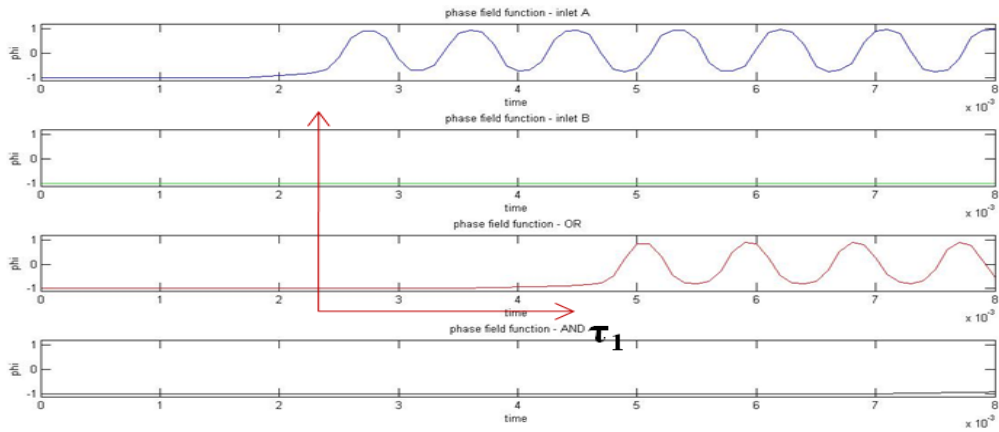
(f)
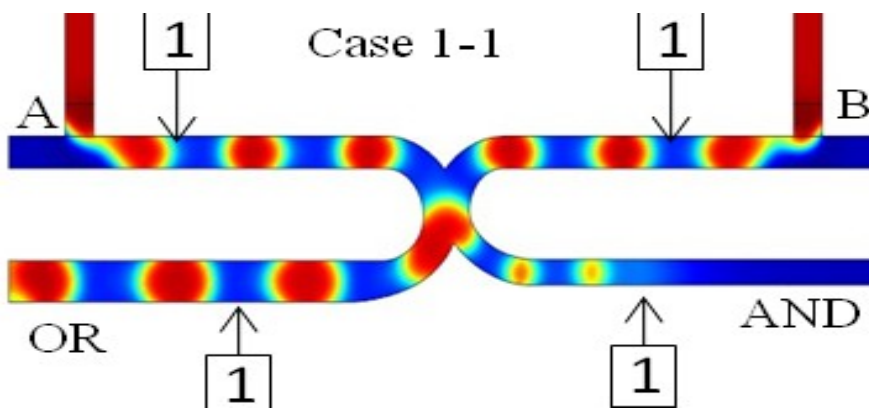
(g)
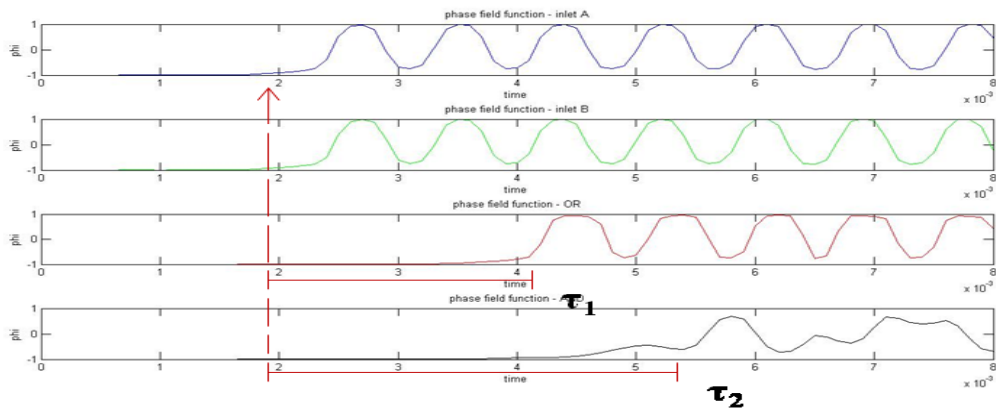
(h)

Figure. 2.31. AND/OR Logic Cases and Phase Field Graph (a)-(b) Case: 0-0; (c)-(d) Case: 0-1; (e)-(f) Case: 1-0; (g)-(h) Case: 1-1

2.3.1.1   Focus on two different type of disperse phase (air versus Hexadecane)

From the previous analysis, the water-air and water-hexadecane in the section *2.2.4* illustrates that the disperse phase air generates bubble faster than the hexadecane. Applying the concept in the computational modeling of universal logic gates using the flow rate mentioned above in the section *2.3*.   To compare the response of two different disperse phase by applying the flow rate of water and air/hexadecane as *0.1667µL/s* and *0.1667µL/s*.

Case 0-1 – The figure *2.32* shows the case *0-1(a)* is the input of the *AND/OR* port *B* and satisfy the logic by allowing the bubble at *OR* gate in figure *2.32(b)*. The response of both the disperse phase is almost same, infact the size of the bubble generated by water-air and water-hexadecane is also same but the bubble generated by water-hexadecane is stronger than the water-air even for the break up. See the graph *2.32(b)*   of the bubble at the OR logic gate response.
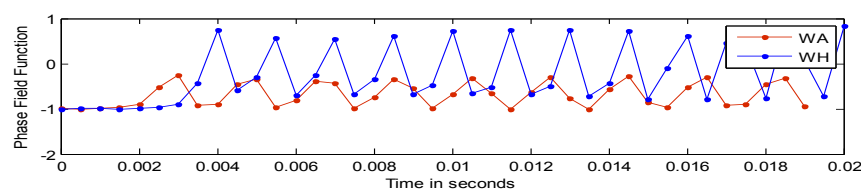
(a)
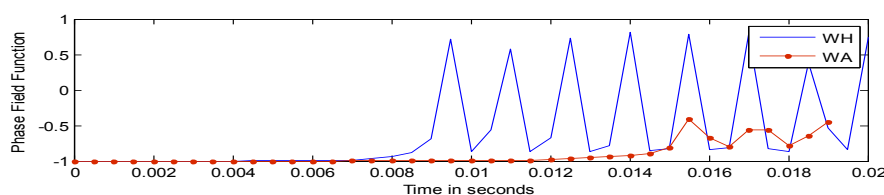
(b)

Figure. 2.32. Case 0-1 (a) Input portB. (b) Output at OR gate

Case 1-0 – The figure *2.33(a)* shows the case *0-1(a)* is the input of the *AND/OR* port *B* and satisfy the logic by allowing the bubble at *OR* gate in figure *2.33(b)*. In this case, compare to the above comment the response at the OR logic gate is respectable. The simualtion time is longer than *case 0-1* for the bubble to to satisfy the logic.
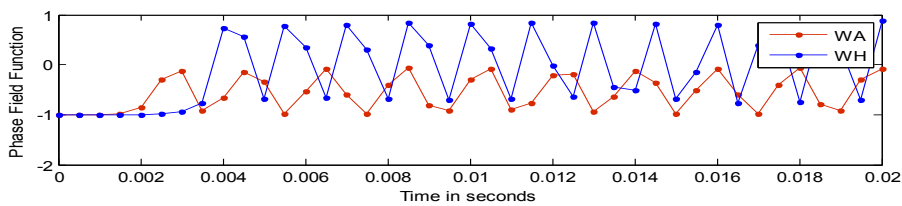

(a)
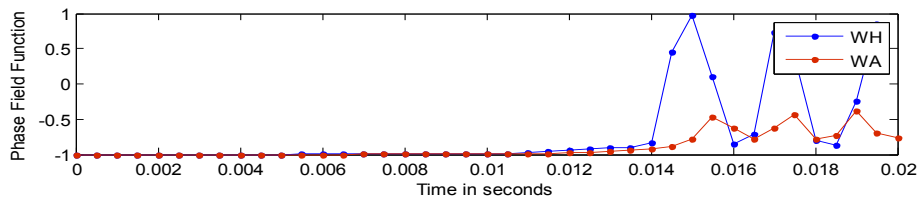
(b)

*Figure.2.33 Case 1-0 (a) input at port A (b) output at AND gate.*

Case 1-1 The comparison of two disperse phase in the case when port*A* and port*B* is *1*, *AND&OR* gate gets the bubble. The response is almost the same when compare to the logic condition but take a look at the figure *2.34(a)-(b)* that the bubble formation has some delay with water and air. The bubble formation of water-air is lighter than hexadecane.
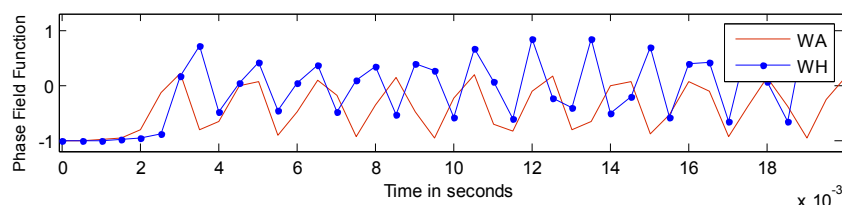
(a)
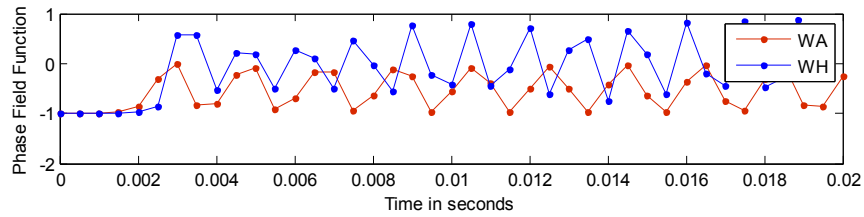
(b)
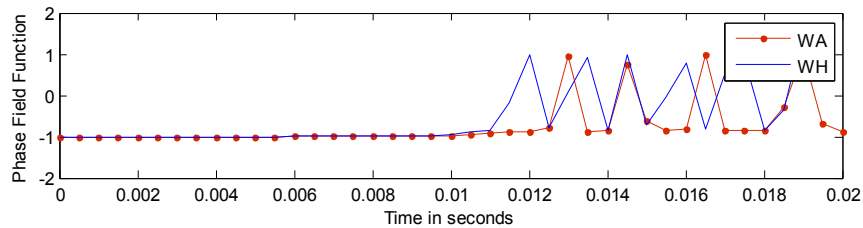
(c)
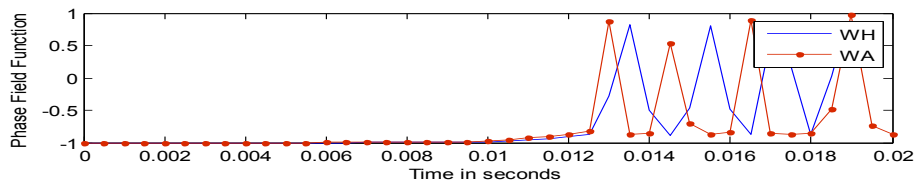
(d)

Figure. 2.34.Case 1-1 (a)-(b) input port A and B (c)-(d) output at port OR & AND

Thus the standard model shown in figure *2.7* can be a basement to design any kind of geometry and the equation generated flow rate can be applicable for any geometry to produce bubble flow. The apprendix shown the table coloumn of different response using flow rates for the geometry respectively.

2.3.2 Computational modeling for the AND/OR Logic Gates-2

The experimental design was taken from the work of scholars Lih Feng Cheow, Levent Yobas, and Dim-Lee Kwong Institute of Microelectronics in Singapore, published in January *2007*, bibliographic source.
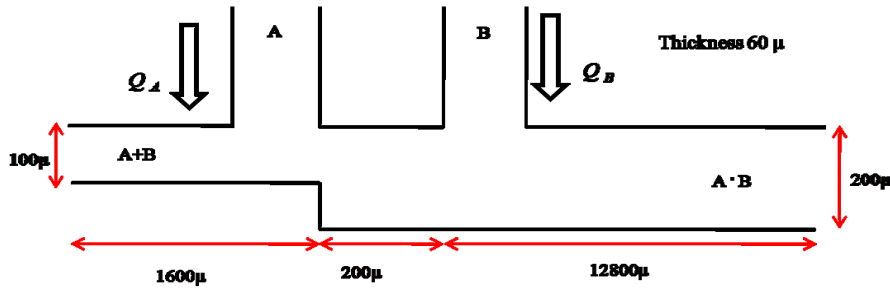
Figure. 2.35. Geometry schematic of the logic gate AND-OR

Schematically it is geometry like the one shown in the following figure has shown in figure *2.35* where *A* and *B* are the two inputs, the left branch is the output *O* and the right branch of the *AND* output. The channels are designed so as to achieve a balance between the hydraulic resistances that ensures the correct logical operation [7].

Benchmark Model - The experimental device just described is served as a starting point for the creation of a new *CFD* model of *AND-OR* logic gate. It describes what should be the proper functioning of the device in question: the drop from B will always OR branch, which offers less resistance [7].
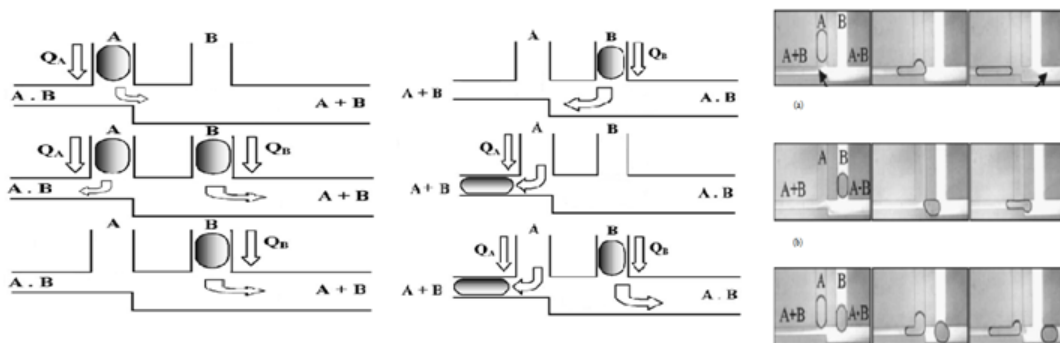
Figure 2.36. Operation of the logic gate (a) Case 0-1; (b) Case 1-0; (c) Case 1-1;

In the absence of drop from *B*, a drop from *A* is directed towards the branch *OR*, since the resistance offered by the latter less than the channel *AND*. In the presence of a drop from *B*, the

resistance offered by the channel increases and *OR* is transformed, then the drop from *A* crosses the canal *AND*. This operation is expressed in the figure.

Geometry - In figure shows the dimensions with which the device has been realized. It can be seen how the geometry is divided into five sub-domains: *D1*, *D2*, *D3*, *D4*, and *D5*. Note that are not specified all sizes of generators, because they are two T-Junctions standards in figure *2.37*. The flow rate of two fluids water and hexadecane are *0.111μL/s* and *0.0889μL/s*.
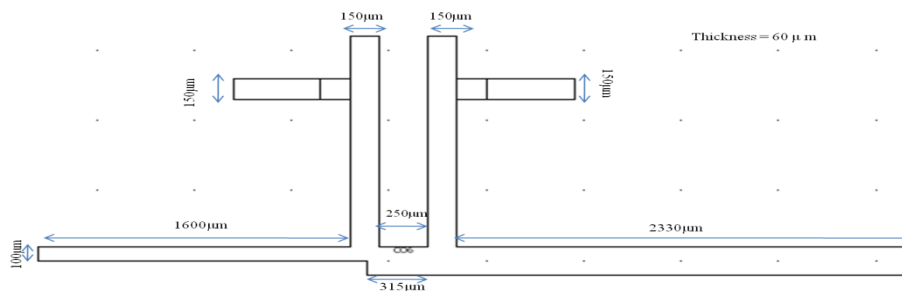
Figure. 2.37. Geometry of AND/OR gate.

Meshing – It performs a discretization of the domain by means of a mesh composed of *11195* triangular elements: Given the complexity of the problem, it is required a very dense mesh to ensure a proper functioning of the logic. It has in fact been initialized, refined twice in full, additional time for domains with wet walls and one last time along the canal ring. Once this is done, it can be assumed that the phase of the design of the door.
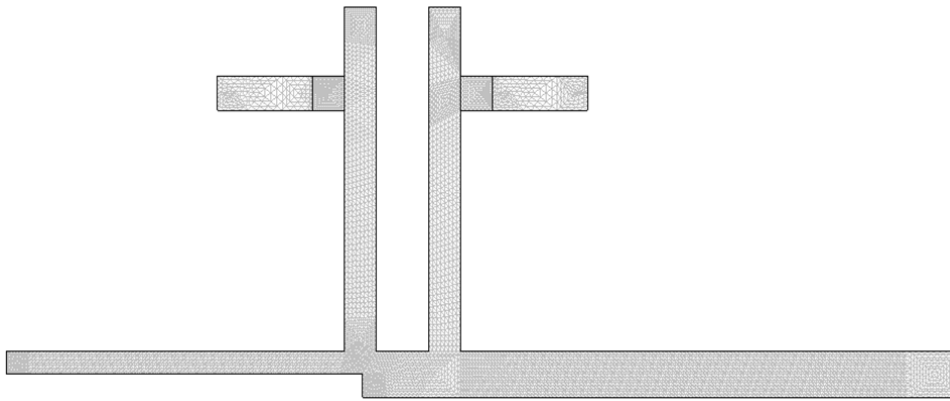
*Figure. 2.38. Refine meshing of AND/OR gates*

Logic Cases - On completion of the design phase, the simulations of the different logical cases, so as to be able to check the actual operation of the door. After completing the simulations for the different logical cases, it was considered a parameter of great significance in the study of a logic gate: the propagation delay. The propagation delay is the time it takes the gate to the output switches from when a switchover occurs at the input. It was assessed by analysis of the Phase Field function: it presents in fact, a peak at points where there are two phases then, evaluating it in input and in output to the door, one can verify the passage of a bubble and calculate the time employed.

Cases: 0-1 - In this case the input *B* is held high by activating the relevant T-Junction, and low input *A* thus the bubbles generated go towards the exit *OR*, in fact this happens.

It proved to be particularly important the choice of flow rates, more precisely the relationship between the dispersed phase is the continuous phase which, as already stated, amounts to *8%*: in this way are obtained larger bubbles that are well adapted to the

channel (more wide compared to that of T-Junctions) both as magnitude that as consistency, managing to get well-defined exit.

If this logic is what turned out to be less of a problem with the implementation, but gave important information on the inputs. By comparing the results in the input and output of the Phase Field function was obtained $\tau=0.3s$.
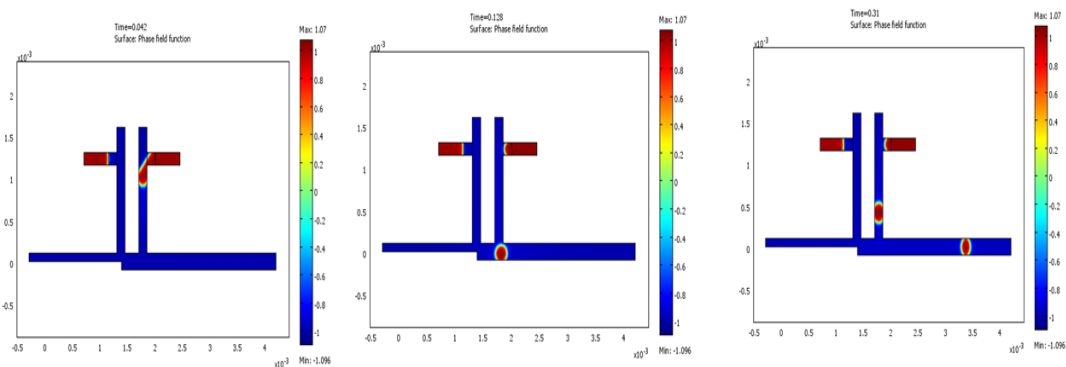
(a)
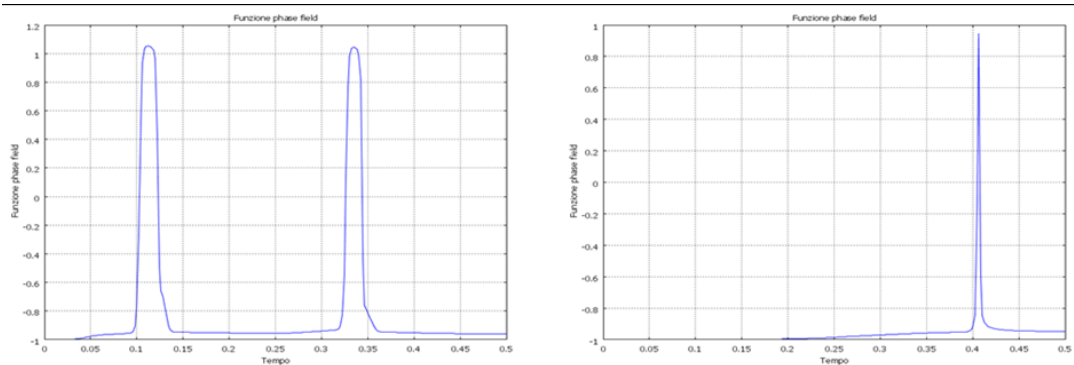
(b)

Figure. 2.39. (a) AND/OR logic case 0-1 (b) Phase field function

Cases: 1-0 - This is the mirror image of the previous case, in fact, is held high the input *A* and input *B* low, and it is expected that the bubble flowing along the channel OR, as actually occurs.

This is the case more delicate for the port in question, since the need of the right balance in geometry that allows the bubble to

flow to the *OR* channel with no signal from *B*, but not when the input is high. To achieve the purpose, initially was carried out a purely static approach, considering only the hydraulic resistance offered by the channels; there is, however, realized that this was not sufficient for a proper functioning of the dynamic logic gate, therefore it was decided to combine all 'previous analysis also an improvement of the geometric configuration such as to render the device completely efficient. This improvement consists of an offset of *65μm* channel *AND* over the output of its T-Junction. From simulations it is further noted, a dynamic quite slow compared to other cases, and this is confirmed also by an increase of the propagation delay. By comparing the results in the input and output of the Phase Field function was calculated *t=0.6s*
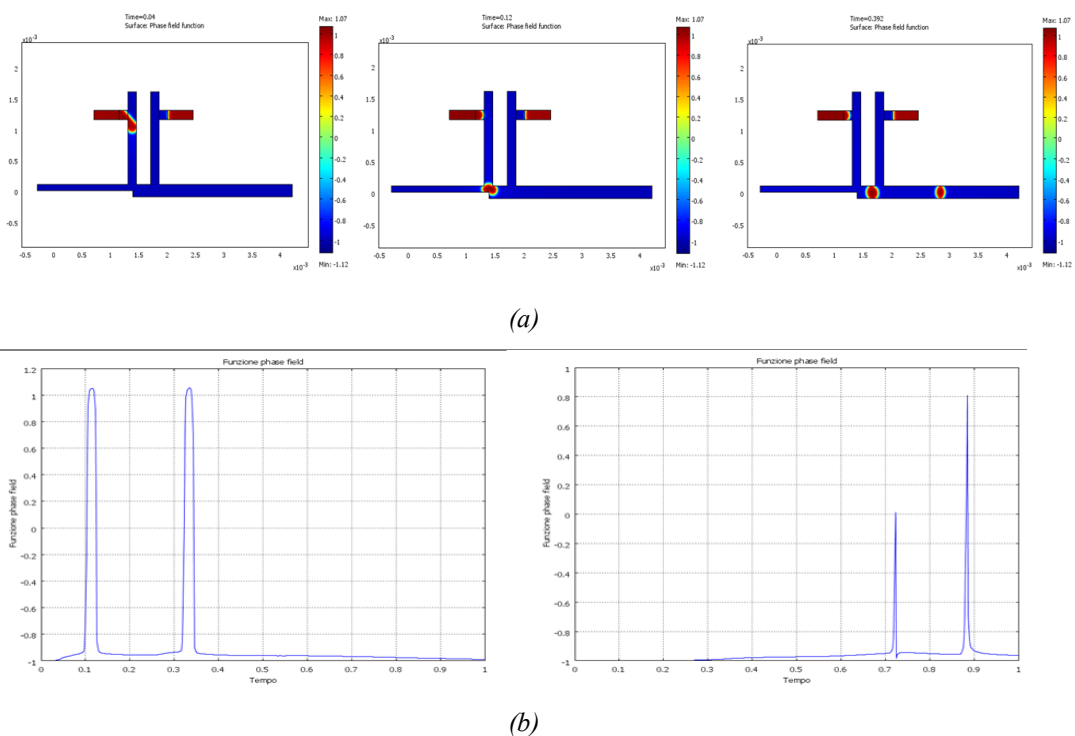

(a)

(b)

Figure. 2.40. (a) AND/OR logic case 1-0 (b) Phase field function

Cases: 1-1 - In this case, both inputs are high and consequently also both outputs. More precisely, the drop from *A* should slide

along the channel *AND*, while that coming from the input *B* should flow along the channel *OR*; what is in fact verified. This case logical needs of a particular matching with in case a *1-0* since the increase in resistance caused by the presence of bubble (from B) in *O* channel must be sufficient to divert the drop from *A* to port *AND*. Comparing the results in the input and output of the Phase Field function was obtained τ =0.2 s for the output *AND* & $\tau=0.15s$ for output *O*.
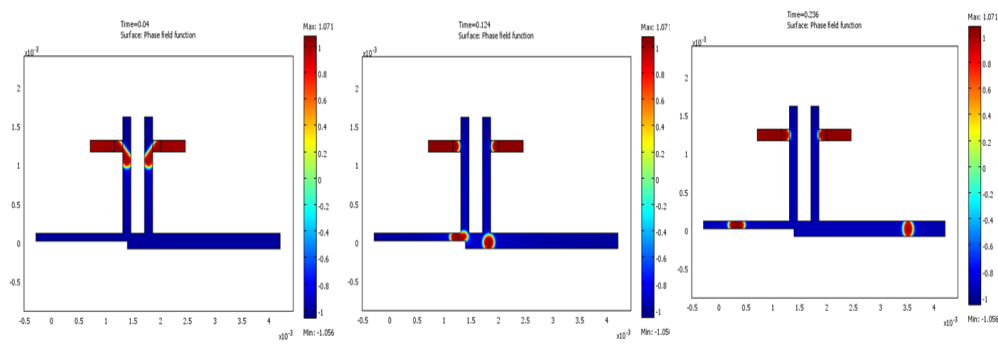
(a)
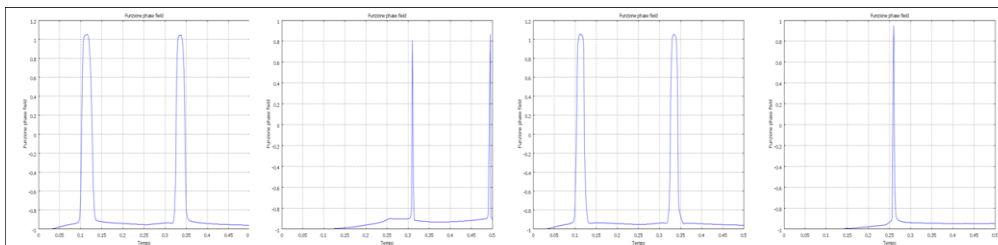
(b)

Figure. 2.41. (a) AND/OR logic case 1-1 (b) Phase field function

Through computational model analysis of the T-Junction, it was possible to determine the geometric proportions that allow a numerical stability and achieve a dynamic characterization of the system, thus allows, from the flow of fluid input, the frequency the bubbles which will generate.

This activity has been of considerable benefit when the face of the work on the logic gate: being able to characterize the generators, it has been possible to better adapt the size, as well as the speed and timing of the bubbles so as to contribute significantly to correct operation of the logic of the door.

For the implementation of the same has proved very useful the realization of the equivalent electric circuit, through which, given the correspondence between the Ohm's law and the Poiseuille Law, it was possible to perform a preliminary analysis fundamental in phase planning. The importance of Computational Fluid Dynamics in the design of a logic gate microfluidics, as a preliminary step with respect to an actual physical realization of the devices has shown.

2.3.3 *Computational modeling for the NOT Logic Gate*

The logic gates are devices that perform particular operations that are adjusted by the recognition of the output pulses. The recognition output must respect the Boolean algebra that is, the concept of true (logical 1) and false (logical 0) that corresponds to the passage in electronics or less current [7].

From the circuit point of view, they are made by means of a transistor technology, usually *CMOS*, and are characterized by various parameters such as operating temperature, maximum applicable voltage, power supportable, but also related to design parameters such as the fan-in that is the number of inputs and fan-out number of outputs. The logic gate *NOT* expresses the logical negation, i.e. if input a pulse true (1) in the output pulse will have a false (0). It is characterized by a single fan-in and fan-out a

multiple. As can be seen placed in a variable input, the output will have the same variable is denied, also known as complementary.

Benchmark model - For the realization of the device was taken cue from an article by *L.F. Cheow et al, Digital microfluidics: Droplet based logic gates*, the microfluidic *NOT* gate has been implemented through the model in figure *2.42*.

This configuration has two inputs and three outputs. Inputs *A* and *S* having as fluid flows *QA* and *QS* respectively: "*A*" is the pulse that carries information bit: *1* if there is a bubble in the channel at 0 if it is absent. "*S*" represents the control input: is always active. The outputs that are three are respectively the first on the left is the output *A* of the central. *A'* is the negation respectively while the output of *S* is called Drain. The principle of operation of this microfluidic device consists of two parts:
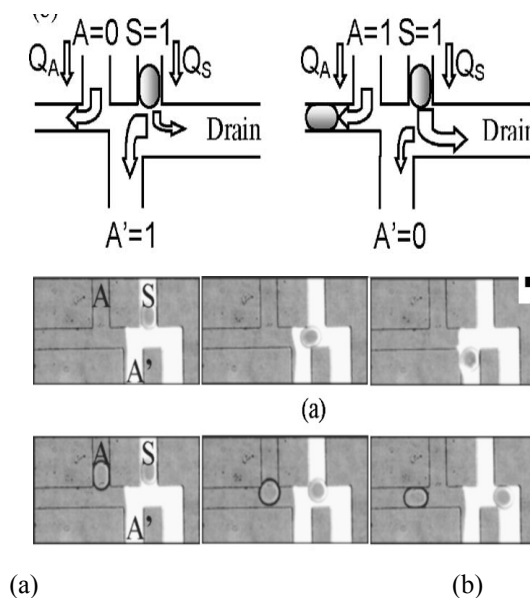

Figure. 2.42. (a) NOT logic gate in microfluidics (b) NOT gate Logic cases

a)   If the output channel of A is present a bubble, the bubble is coming from S Drain addressed in the output in such a way as to have the conditions of *A = 1 A' = 0* and Drain *= 1*.

b)   If the input channel of A there is no bubble, the bubble from S is directed into the outlet channel A 'in order to have the final condition *A = 0 A' = 1* Drain *= 0*. This system can be represented by an equivalent electrical circuit that represents the hydraulic resistance provided by the channels:

Geometry - Studying the system of Article [15] already mentioned has been recreated geometry for microfluidic NOT gate that is able to emulate the behavior of its dual electric. In figure *2.43* is proposed geometry with dimensions in meters used for all tests described below.

        As can be seen were used as generators input of the T-Junction already detailed in chapter *3* that have an *h = 100* micron, which shall perform the task of generators of bits. On leaving the T-Junction is true is proper geometry of the logic gate *NOT* in order to facilitate the task of the simulator *COMSOL* has been integrated with the channel end of the generator making it a unique piece. The subdomains are been set in the following way:
        • *D1A* and *D1S* with Hexadecane;
        • *D2A* and *D2S* with water;
        • *D3* with water.

        From the technological point of view that this system is constructed through a material called Polydimethylsiloxane *PDMS* (material derived from Sloane, silicon compound and oxygen, defined as polymer), having a lithographic pattern of thickness

equal to *60* microns (thickness), the all implemented on a silicon wafer, presents as a fluid continuous phase of the water with the addition of *2%* of *SPAN80* (a surfactant used with the aim of lowering the surface tension between the two fluids), while fluid as the dispersed phase is used the silicon oil.
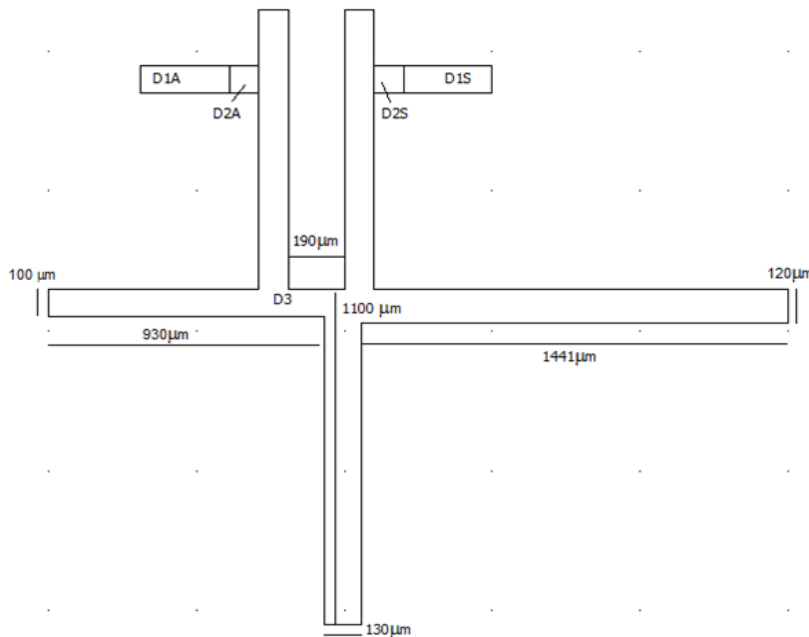

Figure. 2.43 Geometry of NOT logic gate

Meshing - During the creation of the model must be considered the best method of resolution by the simulator of the many variables involved. The mesh helps the simulator to pay attention to the most important points of the geometry. After several tests it was concluded that the most appropriate mesh for the operation of the door were those shown below in figure *2.44*.

The mesh proposals in the previous figure have been realized through a first base mesh, which later has been refined and made more accurate, to make better the processing of data by the simulator has finished even more the mesh in domains *D2* and *D3*.
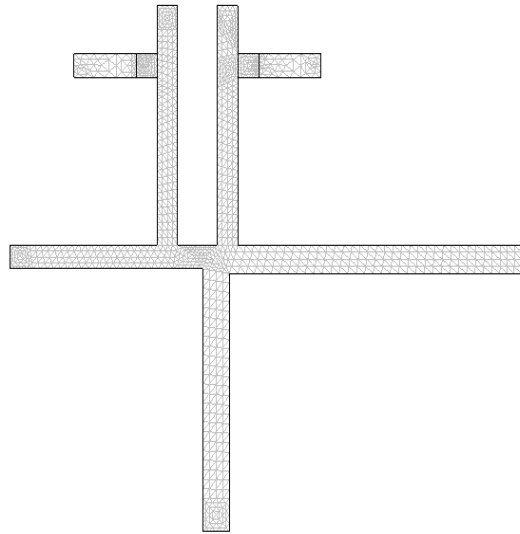
Figure. 2.44. Refine Meshing of NOT Gate

Logic cases *-* There were two logic cases of *NOT* gates computational modeling and phase field function were explained following below. The flow rate of two fluids water and hexadecane are *0.056μL/s* and *0.041μL/s*.

Cases: 0-1 – The logical case *0-1* is characterized by a cancellation of the flow-rate in the entrance of bit "*A*", while the control input "*S*" has a flow rate set to the value that was selected in the previous paragraph. The bubble coming out of the T-Junction "*S*" due to the resistance of channel chooses the path to her easier going into channel *A'*.

The phases of the case shown in Figure *0-1* will *2.45(a):* Now let's consider the propagation delay of this case. Unfortunately in this case, the simulation is not gone perfectly successful, that is, the bubble fails to arrive at the exit and then was taken a point closer; however, and the trend is shown in Figure *2.45(b)* input output. From this graph shows a propagation delay of approximately *0.173s*. This, however, must be considered a

dummy value due to the fact that the simulation cannot be considered fully completed.
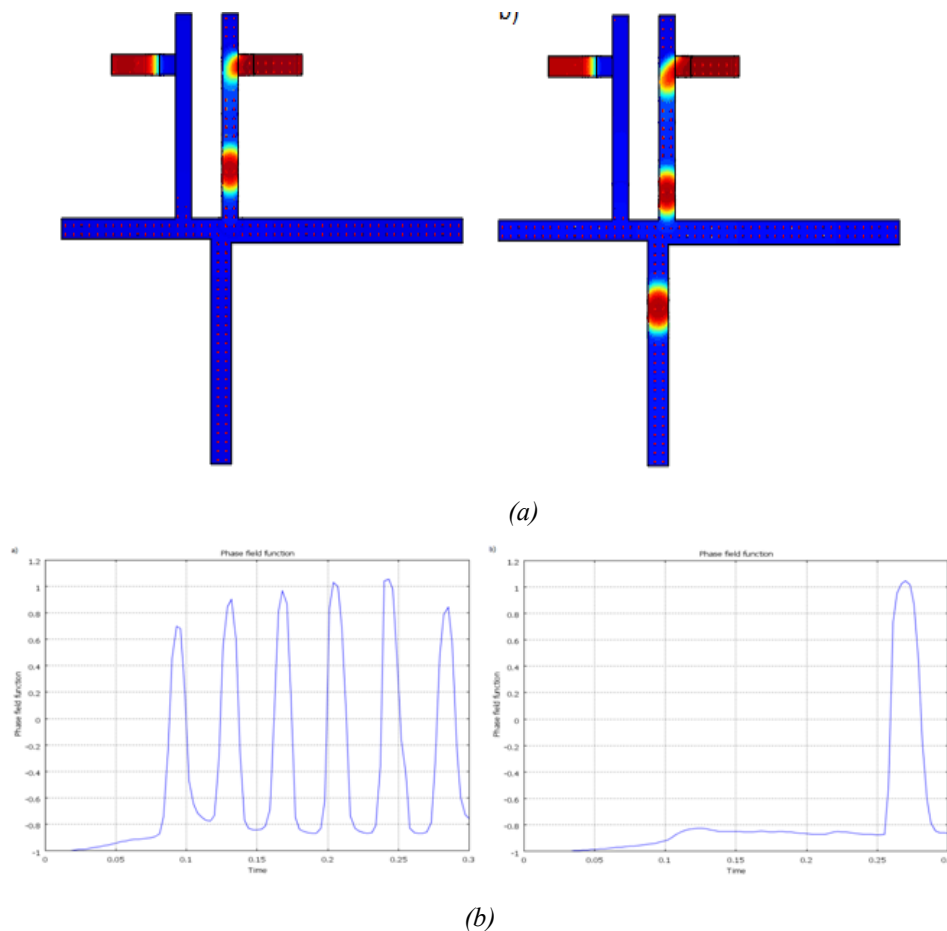

(a)

(b)

Figure. 2.45. (a) NOT gate logic case 0-1 and (b) Phase filed function

Cases: 1-0 - The Case Logic *1-1* has the two inputs working. The bubbles in this case present in both channels of the T-Junction "*A*" and "*S*". The bubble coming from the input bit is the default output "*A*", while the bubble from "*S*" sees a large resistance in the channel "*A* " due to the presence of the bubble in the output channel "*A*" and prefers go to the channel that is less resistance than the output of the "Drain". The phase of the case has shown in figure *2.46(a)*.

Wanting to make a further comparison with electric gates an important factor to consider is the propagation delay. I.e. the time that elapses between the input and the output of the signal. In this case, it is assessed the time that passes between the input of the bubble in the domain *D3* and the output has shown in figure *5.3(b)*. The graph shows that the delay of the first bubble is *0.05s* to start from T-junctions.
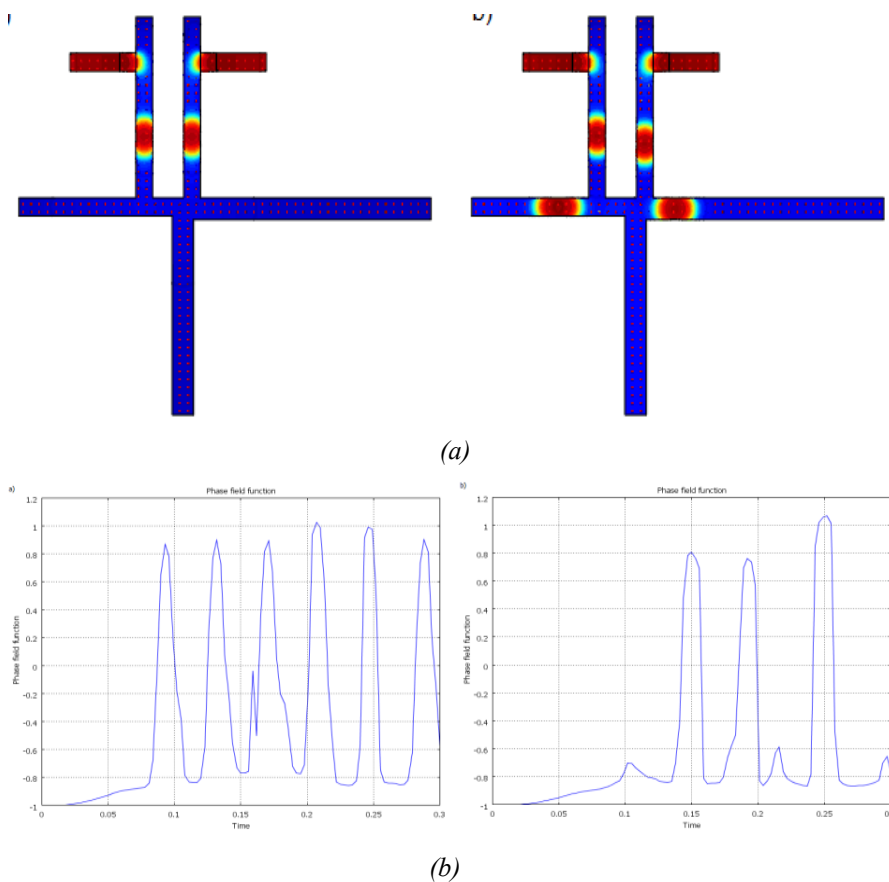

(a)

(b)

Figure. 2.46. (a) NOT gate logic case 1-1 and (b) Phase filed function

2.3.4 *Computational modeling for the Flip Flop Memory circuit*

It is capable of on-demand trapping and release of individual bubbles, implemented as a Flip-Flop memory [6] [10]. It has been explained through the experimental model satisfying the bubble logic, meshing and logic cases.

Benchmark Experimental Model - A bubble minimizes its surface energy by adopting a shape with the smallest surface area. The device holds a single bubble indefinitely until it is toggled by another bubble arriving at the inlets, dislodging the stored bubble by flow through the channel connecting the lobes. Although the incoming bubble are much longer than the Rayleigh plateau Criteria for breakup. The presence of a bubble in the Flip-Flop ensures that the incoming bubble travels to a single lobe without breakup.
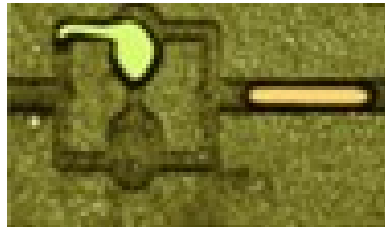
(a)

TOGGLE	*UP*	*DOWN*	*UP+1*	*DOWN+1*
1	*1*	*0*	*0*	*1*
1	*0*	*1*	*1*	*0*

(b)
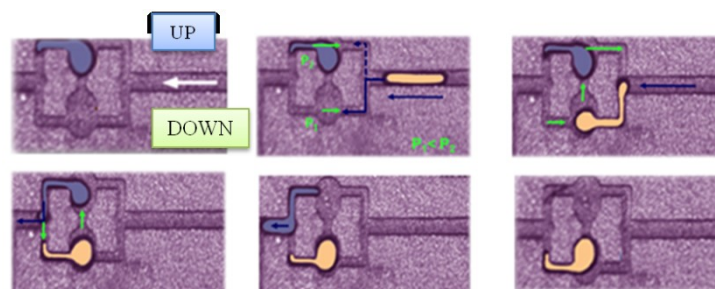
M. Prakash and N. Gershenfeld, Microfluidic Bubble Logic, 9 FEBRUARY 2007 VOL 315 SCIENCE

(c)

Figure. 2.47. (a) Toggle switch (b) Truth Table of Toggle switch (c) Switching cases

Geometry - The reading has been noted at two points in red marks in figure *2.48.* The sequence of frames shot and phase field

contours are shown in figure *2.50(a)* giving a clear view of the working principle of the flip-flop memory circuit.
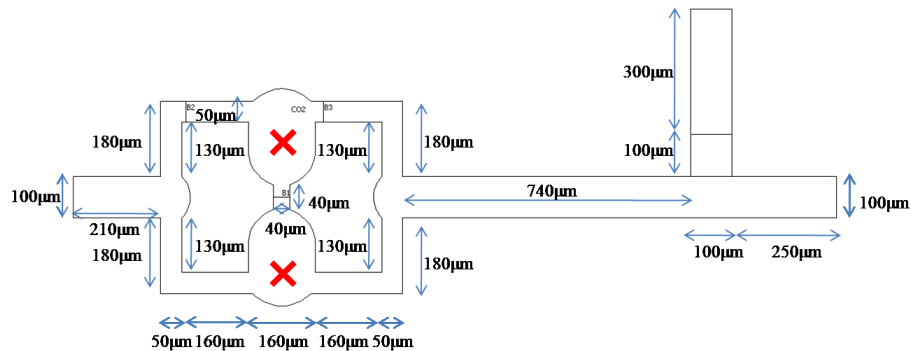

Figure. 2.48. Toggle or Flip-flop Switch Geometry

Meshing – The mesh applied in this geometry is extended mesh has number of degree of freedom is *35080*. The *2D* domain of the Toggle switch is discretized using an unstructured finite element grid with *5676* elements using sub-domain mesh parameter method as triangular. The base mesh of number of mesh point is *3009*.
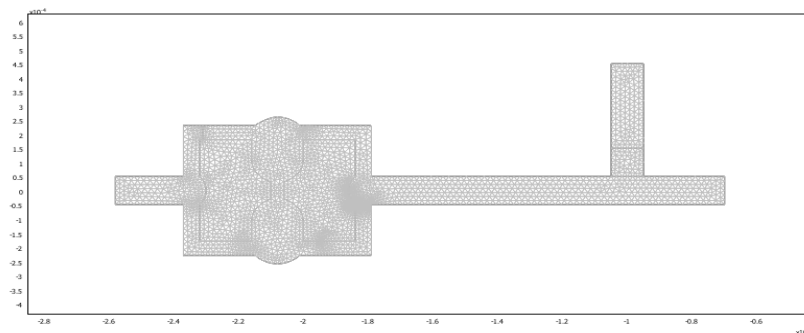

Figure. 2.49. Refined Meshing

Logic cases - The given flow rate for water and air is set respectively to *0.1024µL/s* and *0.4µL/s*. The results of the phase-field signals are shown in figure *2.50(a)-(b)*. The device holds a single bubble indefinitely until it is toggled by another bubble

110

arriving from the T-junction; dislocated the stored bubbles by flow through the channel connecting the two lobes.

The bubble is stored in one lobe and no input of bubble from the T-junction at the initial time *t=0* as shown at the extreme left in figure *2.50(a)*. The change of resistance due to the presence of a bubble ("*toggle*") at time *t*=2.8 ms at the T-junction branch make the stored bubble in the upper lobe moving slowly towards the exit channel as shown in figure *2.50(a1)*. Then due to the presence of a bubble in the upper lobe, the new incoming bubble passes through the down lobe at time *t*= 4.8 ms and then is stored there as a locked information in figure *2.50(a2)*.
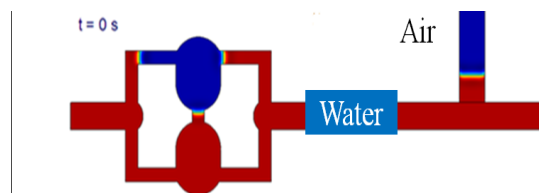
(a)
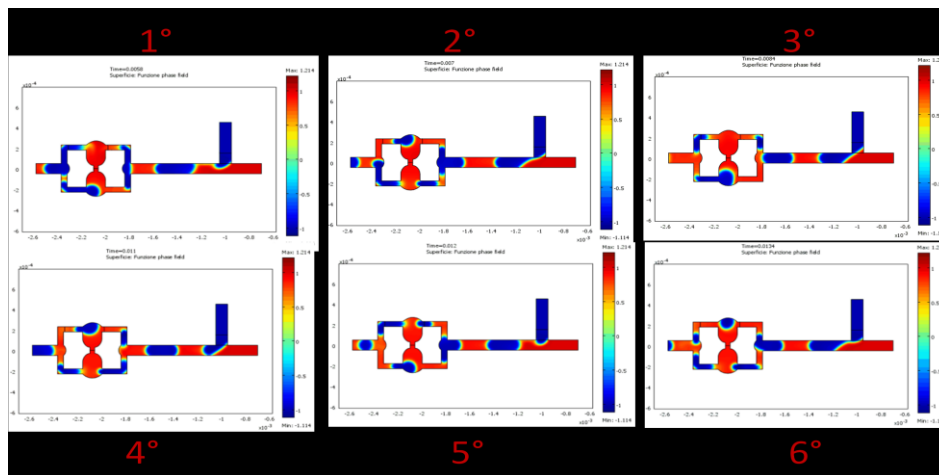
(b)
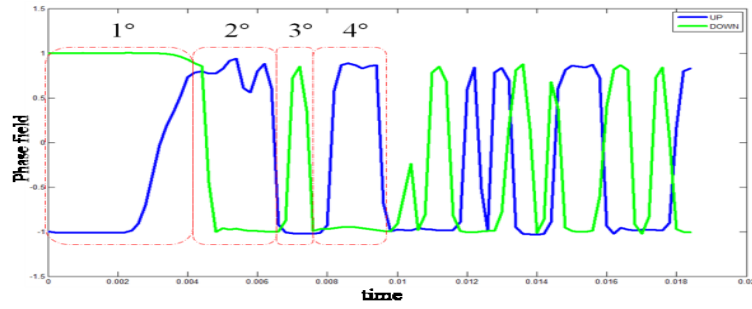
(c)

Figure. 2.50. (a) Computational modeling of Toggle switch (b) six switching cases (c) Phase field function

Chapter-3

The study in the context of micro-optofluidics analysis have allowed to define in some detail the integrated system used to Thorlabs has provided for the experiments in micro-optofluidics. In particular, the characterization of the microfluidic detection devices has been used in the experimental studies of two-phase flow. In addition, the analysis carried out in the various micro-channels fixed unique features in terms of flow rates for each dimensions. The key issue is finally the study and designs of an embedded system optofluidics in micro-optics Lab-On-Chip (LOC), which allows achieving very narrow spaces in a microfluidic system, ensuring a degree of portability, which it integrates optical realizing therefore, the right balance between the two disciplines. Played as part of a global project in which design and manufacture of micro devices LOC, and experimental studies within micro-optofluidics could easily fit in a biochemical analysis of the microscopic scale of biological particles of various kinds.

OPTICAL ACTUATION AND MONITORING IN MICROFLUIDICS

3.1 Basic Concept of optics for Microfluidics

The topics covered in the first sections of this chapter have been presented with the information in optics and how it relates to the world of microfluidics.

Also in this case it is necessary to define some important properties that will aid in understanding of concepts described below.

The radiation pressure- It consists in the pressure exerted on any surface exposed to electromagnetic radiation. This phenomenon was derived by theoretically by James Clerk Maxwell in *1871* and verified experimentally by Lebedev in *1900* and Nichols and Hull in *1901*. The pressure is very weak, but can be detected by means of a special instrument called a radiometer.

Interfacial tension- It is established when in contact with two fluids of different phases and is defined as the additional energy per unit area due to the formation of an interface. To implement the implementation are exploited then much focused optical radiation, in order to cause the interfaces of the fluids, deformation or local heating. Numerous studies have been carried out to investigate the destabilization of the interfaces of a fluid subjected to a radiation pressure, exerted, for example, by a laser.

The result obtained is that the deformation of the interface is very weak due to the strong stabilizing effect due to the interfacial tension [13]. To overcome the limitations of the techniques that exploit the pressure of radiation, is used, instead, the so-called "*Thermo Capillary Effect*" induced by a laser.

3.1.1. Definitions and Recurrent Parameters

The term "*optical*" refers to everything that is based on "*optical radiation*", i.e. able to be detected by the human eye. The optical radiation represents a small part of the electromagnetic radiation. It comes to oscillations of an electric field and a magnetic field; these oscillations propagate in a straight line and the electric and magnetic fields have a direction perpendicular to the direction of propagation and perpendicularly relative to one another.

The electromagnetic spectrum consists of wavelengths with orders of magnitude ranging from a few pico meters (*10-12m*) to several thousands of kilometers (*103m*). The visible spectrum identifies a very small part of the whole electromagnetic spectrum and has wavelengths between *400* and *700nm* (from violet to red). The wavelength is related to the frequency of propagation, by the speed of light in vacuum, through the relationship:

$$\lambda = \frac{c}{v} \qquad\qquad (3.1)$$

where λ is the wavelength of the electromagnetic radiation, v is frequency propagation and c is speed of light in vacuum.

Optics Classification into two categories:

- *wave Optics*

- *geometrical optics*

The physical laws that govern the wave optics are enclosed in *4* notes Maxwell's laws of electromagnetism. The behavior of the light rays is described by the so-called geometrical optics. This is only an approximation of the behavior of light, which is described fully optics wave, but an approximation that is able to describe most of the phenomena, particularly if the sizes of the objects which it interacts with light and the distances into play, are much larger than the wavelengths of visible radiation (*VIS*).

From this, it is understood that for the study and design of an electro-optical system, one can resort to approximations dates geometric optics, seeing the light rays in the form of many linear and free of undulations; in this way does not take into account aberrations and interferences of the system: the rays thus calculated are transferred through the optical system, without suffering the effect of aberrations; aberrations cause, then, in reality, deviations (usually small) in the directions of the rays with respect to the actual directions calculated with linear equations. Not taking account of aberrations is possible, therefore, verifying the basic behavior of one or more optical components traversed by the radiation.

The interest in studying hours, regardless of aberrations, geometric relationships that link the relative positions of the optical system, object and image. It attracts in what are called the characteristics "Gaussian" of the optical system, i.e. the characteristics

of an optical system that does not depend on the aberrations. Define certain parameters that identify the characteristics of a Gaussian optical system:

Optical axis: indicates the direction of propagation of the electromagnetic radiation, then the direction of the path of light.

Subject: represents the sample of which is to create an image, very often also indicated in microscopy, with the term "specimen".

Picture: reconstruction of a view of an object, obtained by means of those rays of light that depart from its surface or that exist in space and, after being collected by an optical system, are, from this, conveyed in positions geometrically similar to those of points where the rays are gone.

An optical system act to the formation of an image collects the light beams which diverge from each point of the object and transforms them into beams that converge at other points, producing, so, an image; if the beam converges at a point after being passed through the optical system, the image produced is "*real*", and you can pick it up on a screen, and if the beam diverges from a point, the image produced is "virtual", is located in the "*space images*" of the optical system , but appears to come from an object placed in the "*space object*".

Conjugate: two points are so called, when one of them is the image of the other.

Focal plane: is the flat surface perpendicular to the optical axis, passing through the point where the rays converge relative to a point object placed at an infinite distance from the optical system (in this case, for the optical system can be understood even a simple lens).

Main floor: is the flat surface perpendicular to the optical axis passing through the points of meeting of the extension of the rays coming from an object point to infinity before the axial optical system (object space) and after it (image space). In the case of a single convergent lens, the main plane corresponds with the surface of the lens.

Focal length: distance between the focal plane and the main plane.
Back focus: distance between the vertex of the last surface from the focal plane and the focal plane.

Input/output: The maximum diameter of the beam of rays coming from an object point and passing through the optical system to the point image is limited by a mechanical diaphragm, which can be constituted by the edge of a lens or an optical component specific.

Major Radius: radius joining the point object with the center of the entrance pupil. In the case of a single lens, the principal ray is the straight line passing through a point on the object and the point of intersection between the optical axis and the main plane (which would represent, in this case, the surface of the lens).

3.1.2. The optical phenomena

The main phenomena involved in the study of optical systems, are refraction, reflection, diffraction, dissemination, polarization, interference and aberration. Among these, have lesser significance aberrations and interference, because since the size of the objects which it interacts with the light, are much more of its wavelength.

Refraction and reflection- When a radiation of light, propagating, passes through a separation surface between two media having different physical characteristics, the electromagnetic wave will succeed in part to cross the second means and in part will be reflected from it, thus creating a component transmitted (or refracted) and reflected.

These phenomena are governed by the "laws of Snell," which state that in the passage of a wave between two media with different physical characteristics, it will create a reflected component with angle of reflection equal to that of incidence, and a component refracted (or transmitted) with an angle of refraction (i_2) given by *3.3*:

$$i = r \qquad\qquad\qquad (3.2)$$

$$n_1 sin(i_1) = n_2 sin(i_2) \qquad\qquad\qquad (3.3)$$

Where i_1 is the angles of incidence, r angle of reflection, i_2 angle of refraction, n_1: refractive index of the first medium, n_2 refractive index of the second medium [13].
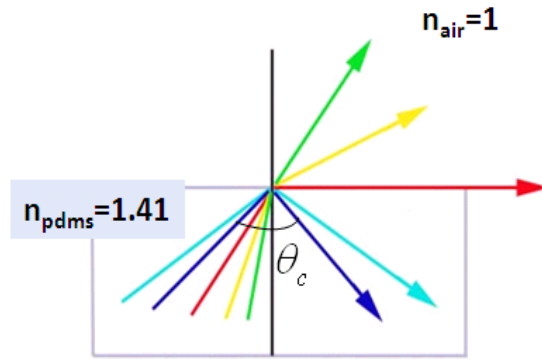
Figure. 3.1. Law of reflection and law of refraction

The index of refraction (*n*) is an intrinsic characteristic of all means and represents the ratio between the speed of light in vacuum (*c*) and the speed of light propagating within a medium (*v*), in fact all 'interior of a material the light propagates at a slower speed than that in a vacuum, by this it is clear that the index of refraction is always greater than one, and only the vacuum has refractive index unit:

$$n = c/v \qquad (3.4)$$

where:

$$c = 1 \Big/ \sqrt{\varepsilon_o \mu_o} \qquad (3.5)$$

$$v = 1 \Big/ \sqrt{\varepsilon_r \varepsilon_o \mu_r \mu_o} \qquad (3.6)$$

ε_o and dielectric represent respectively the "*dielectric constant*" in a vacuum and in the middle; μ_o and μ_r are respectively the "*magnetic permeability*" in the empty and in the middle. Through simple mathematical manipulations, by *3.4*, *3.5* and *3.6*, it is seen that the refractive index can also be expressed in the form:

$$n = \sqrt{\varepsilon_r \mu_r} \qquad\qquad (3.7)$$

The angle of incidence (as well as those of reflection and refraction) is the angle formed between the direction of propagation of the radiation and the normal to the surface that separates the two means. From *3.3*, it is evident that, when the wave passes from one medium to a less reflective more refractive ($n_1 > n_2$), then the angle of refraction is greater than that of incidence ($i_1 < i_2$); vice versa, passing from one medium to a less reflective more refractive ($n_1 < n_2$), there is a decrease of the angle of refraction ($i_1 < i_2$). In case, the radiation is incident with a zero angle, will be zero also the angle of refraction [13].

Diffraction, polarization and diffusion- The diffraction occurs whenever a wave encounters an obstacle whose dimensions are comparable or smaller than the wavelength. This phenomenon has been studied systematically by two great minds, Huygens and Fresnel, who expressed three basic principles that allow you to simply understand the operation of the effect of diffraction.

1) Principle of Huygens. All points of a wave front that is the locus of points whose phase differences anything you can think of as coherent sources of circular waves. The wave front next is constituted by the effect of such sources.

2) Principle of Huygens-Fresnel. All points on a wave front can be thought of as coherent sources of circular waves. The perturbation in a generic point *P* is given by the interference of these waves.

3) Postulate Fresnel. The intensity of each source of coherent circular waves which constitutes a wave front is perpendicular to the tangent of the maximum wave front at the point considered, while decreases to zero parallel to it.
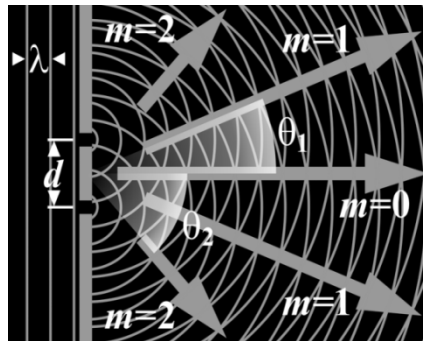

Figure. 3.2 Diffraction caused by two slits

The phenomenon of diffraction, under previous principles and postulates, is more noticeable if the dimensions of the obstacles are similar to the wavelength that meets them. In particular, the slits show more the effects of diffraction, if their dimensions are comparable with the length of the wave which passes through them. If two slits, observe, in addition to the phenomenon of diffraction, also to the interference between the two waves "generated" by each slit. Thus the picture that is projected is more complex.

If a number of slits equidistant from each other and from the same opening, built what is called diffraction grating. If the light is laser type, and size of the slits is of the same order of magnitude as the wavelength of the radiation, on a screen placed in front of the hole or the slot can be observed the formation of alternate light and dark areas. The phenomenon is explainable by the wave theory of light and is derived from phenomena of interference between the waves.

The light diffusion occurs every time a beam of light meets an obstacle. When passing through a medium, the electromagnetic radiation interacts with the molecules and the atoms which constitute the medium itself. Part of "photons" which constitute the radiation may be absorbed or diffused by the medium constituents; this phenomenon reduces the intensity of the radiation but does not alter the energy associated with each photon: the wavelength is not altered the phenomena of absorption and diffusion are statistical phenomena that have no influence on the wavelength of the radiation [13].

The polarization of an electromagnetic radiation indicates the direction of oscillation of the electric and magnetic fields, during the propagation of the wave; the electric and magnetic fields are orthogonal to the direction of wave propagation and with each other, while the wave propagates, they oscillate in a plane orthogonal to the direction of propagation, the fields can vibrate forming an ellipse, in which case it is called "*elliptical polarization*"; a circumference, "*circular polarization*"; or a straight line, "*linear polarization*".

Interference and aberration- The interference is the effect of the overlap, in space, of the electromagnetic waves constituting the light. When, in space, overlap two electromagnetic radiations which have in common at least one component of the polarization (which are not, therefore, linearly polarized with polarization planes orthogonal to each other), the parallel components of the electric and magnetic fields are added algebraically taking into account of the respective amplitudes and phases.

The intensities of the sum, which are equal to the square of the amplitudes, can vary from zero, in the case of equal amplitudes and phases in opposition, to four times the intensity that would have each of the two radiations considered separately, in the case of equal amplitudes and phases equal.

In space, the ambient light causes constantly a large number of interference. Aberrations are deviations from the Gaussian behavior. The study and classification of aberrations is of primary importance for the construction of optical systems. Here some types of aberration resulting from the limitations of the theory of Gauss: Spherical aberration. Concern images due to point-like objects belonging to the optical axis. The paraxial rays converge at the point image as expected from the theory of Gauss, while the rays of greater aperture converge at different points on the optical axis, at a distance from the theoretical point image which is a function of the opening angle.

Coma: The coma aberration is analogous to sphericity, but regards point-like objects placed outside the optical axis. In this case the image has a shape that resembles that of a comet (hence the name).

Astigmatism: As regards the coma images of springs located outside the axis and regard the formation of the image in a direction parallel to the axis.

Field curvature: An optical system possesses plans conjugates only in approximation of Gauss: to object points lie on a plane not correspond in general images that are on a plane. The curvature of the field is due

to the loss of definition to the edges of the image of an extended object.

Distortion: The magnification is generally a function of the distance from the optical axis: an image of an extended object is thus distorted. Chromatic aberration: This aberration is due to the fact that the index of refraction varies with the wavelength of the light and that, in general, do not work with monochromatic light.

3.2   Methods of Optical Actuation

The microfluidic devices have been developed with basic structures similar to those realized in macro scale; can be divided into two categories namely in active devices and passive devices. The latter are generally more easy to fabricate, but are less functional and active devices are not activated by external signals imposed by us, but their operation is tied to the natural evolution of the environment that surrounds them, for example, a control valve passive is driven by the pressure of the fluid that attempts through, while a micro active valve can be activated or deactivated by an external signal related to the state of the entire fluidic system assessed at that instant [12].

Micro valves- The active micro valves can be classified according to different parameters:

• Liquids that run through-liquid or gas;

• Materials used in the production - silicon, glass, polymers;

• Implementation mechanisms - electrostatic, pneumatic, thermo pneumatic, etc.

• Microstructure physical implementation - membrane, etc.

The most common way to distinguish them is the classification based on mechanisms.

Pneumatic actuation- The pneumatically actuated micro valves to provide for the presence of an external source of pressure to implement a flexible diaphragm; conceptually these micro valves are constituted by three orifices through which the fluid is injected into the system, of which two (places laterally with respect to the structure) serve to flow the fluid of interest through the micro valve, the remaining channel (located below) instead is useful to inhibit the passage of the fluid as it moves upward a membrane that is opposed to sliding.
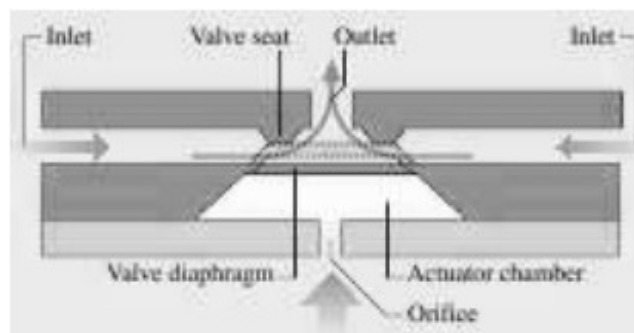
Figure 3.3. Pneumatic actuation

Implementation thermo pneumatic- This technique is carried out by heating a fluid (usually gas) contained in a cavity confined. The increase of the temperature determines the increase of the gas pressure

and this pressure is exploited for deflecting a membrane that inhibits the passage of the fluid in the valve [6].

Electrostatic actuation- The devices implemented electro statically have a simple structure and are therefore easy to realize; present a membrane consisting of a thin conductive layer having an S-shape (S-shape) which rests on two electrodes from which and fed to deflect. Such membrane regulates the flow inside a chamber or less obstructing the passage of the fluid.
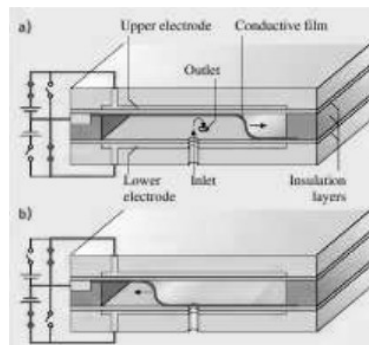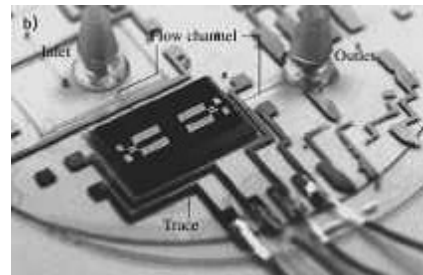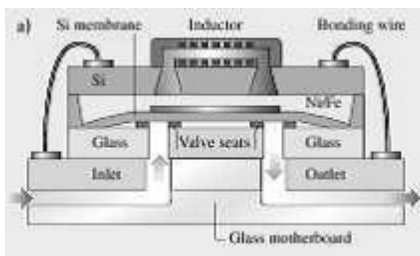

Figure. 3.4. Electrostatic actuation

Piezoelectric actuation- The piezoelectric actuators are generally the fastest in realizing the implementation; are constituted by a movable membrane on which and deposited a film of piezoelectric material which deforms when an electric field is applied and this deformation is then also transferred to the membrane of the valve [12] [13] .

Electromagnetic actuation- The micro valves actuated electromagnetic have the advantage of being almost insensitive to external interference, the disadvantage of being subject to a bag-making process rather complex. Their membrane and consists of a thin layer of electro-magnetic equipment such as *Ni-Fe* which is actuated by an electromagnet that attracts external to whether or not such a thin layer by inhibiting the passage of the fluid.


(a)   (b)

Figure. 3.5. Electromagnetic Actuation

Micro pump- One of the objectives principalities to achieve an integrated microfluidic system and to develop efficient micro-pumps, in macro scale there are many techniques that exploit different-pumping well established principles. This type of pump based on the flow of a constriction of a tube, while in micro scale it is possible to use other effects such as the electro-osmotic pumping.

The most important parameters to be considered in relation to a pump are as follows:

• Maximum flow: and the volume of liquid per unit time delivered by the pump;

• Maximum back pressure: and the maximum pressure at which the pump may object in his work, and in this pressure the maximum and nothing.

Micro pumps equipped with control valves- The following figure shows a typical and pumping mechanism that uses of valves control; such a pump and equipped with two valves, an inlet and the other Pout separated by a chamber.
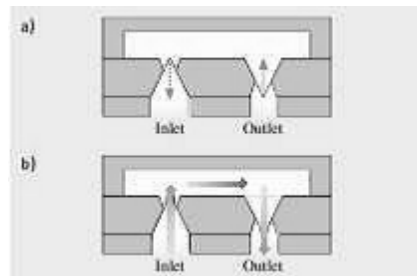
Figure 3.6 Valve Control

When the membrane is deflected upward in the pumping chamber is created a zone of low pressure and the inlet valve is forced to open up so that the fluid is sucked inside the chamber; in while in which the membrane returns to its original state and continues to deflect downward, it creates a positive variation of that pressure closes the inlet valve and simultaneously in mind ago open that output. In this way the fluid is expelled from the chamber and the pump can suck again another fluid.

Micro pumps diffusion- The idea on which is based the operation of these pumps and linked to the fact that the geometric structure of the inlet valve has a preferred direction of flow towards pumping chamber, while that of the outlet valve presents a privileged direction of flow opposite to the chamber pumping.

In fact, as the pump and in the mode of suction (suction), the flow within the diffuser inlet and mainly directed towards the pump and from the speaker output is has a gentle reflux; if instead the pump and the pumping phase (compression), the diffuser P_{out} allows to expel most of the fluid (properly a liquid) from the chamber, while the diffuser inlet allows a gentle reflux. The net effect is that the pumping occurs from left to right. The micro pumps diffusion are simple in operation and have no valves, but have the drawback of not eliminable reflux [7].

3.2.1 Thermo-Capillary Effect

The optical forces at play in microchannels are very weak, on the order of *pN*. They are therefore ineffective in manipulating the fast streams of drops or bubbles.

The alternative is to cause extensive localized thermal stress, also known as "Marangoni effect" [13], the interface of the droplet. The orders of magnitude of the forces thermo capillaries are around *μN* [14] and therefore are much more efficient than optical. This effect is associated with the temperature dependence of interfacial tension σ (*T*) between two immiscible fluids. Suppose that a drop (or bubble), which flows in a fluid within a channel, is in the presence of a temperature gradient, caused by a highly focused laser [12] [13]. What

happens is that the temperature gradient will itself have a gradient of interfacial tension, which will induce a change in viscosity for both fluids. The result of this process is the formation of an interfacial flow, directed towards the area with the highest interfacial tension. It develops both inside and outside the drop. Therefore, due to the preservation of the mechanical moment, it has the displacement of the drop in the opposite direction. This is shown in the following figure:
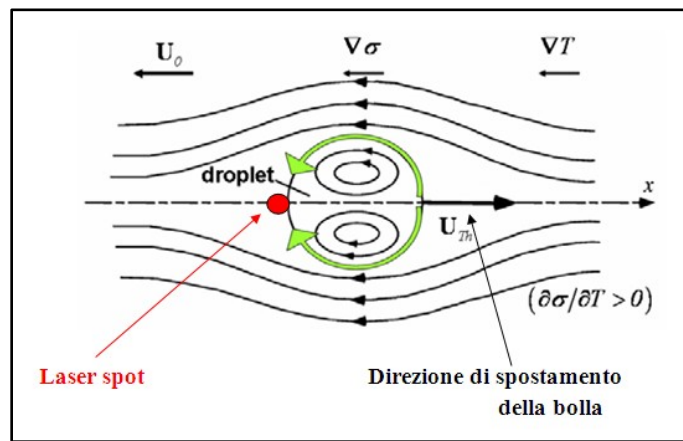

Fig. 3.7 Thermo Capillary Effect

The migration thermocapillary of a drop is given by the following expression [13]:

$$U_{Th} = -\frac{2}{2\mu_o + 3\mu_i}\left(\frac{\partial \sigma}{\partial T}\right)\frac{R}{2 + \Lambda_i/\Lambda_o}\nabla T$$

where R is the radius of the droplet, μ_o, i_e $\grave{A}_o$, i are respectively the viscosity and the thermal conductivity and the subscripts i, or are inside and outside, that is, inside and outside the drop.

From this equation it can be seen U_{TH} depends on the temperature gradient and not directly from it. This means that even a weak heating, can manipulate the flow in an efficient manner if the gradient is large. This usually happens with the light of lasers [13]. Finally, it is clear dependence on the sign of the term ($\partial\sigma/\partial T$). Then a laser beam will attract or repel the drop depending on whether $\partial\sigma/\partial T$ is less than or greater than zero.

3.3   Method of Optical Monitoring

Considering microfluidic applications in the bio-medical field, both in vivo and in vitro, the movement of fluids, gases and particles, can be studied through the analysis of optical information, through a study of morphological and deformations in the micrometer scale. Flow maps, particle migration and deformation are in fact central to the study of multiphase microfluidics.

Monitoring Local - There are several methods for the determination of the flow in two-phase systems or in suspension, including those based on the Doppler Effect and those that exploit optical information.

The Optical Doppler Velocimetry Intra vital can be used for micro vessels of any size although it is not suited to measuring flow in vessels that are located on different functional layers. Another technique, based on the principle of Doppler, *ELA*-Enhanced High Resolution Laser Doppler Imaging (*LDI-EHR*) carries out measurements of flow using the principle of scattering of light and the

analysis of the spectrum of the signal scattering. In both cases measuring velocities is not absolute but relative to the time window.

The methods involving optical properties are based on optical contrast between fluids, gases and particles. The methodology Dual Slit (*Wayland et al. 1967*), in particular, is a real-time method for the measurement of the transit of red blood cells (*RBCs*) between two optical windows, thus obtaining the blood flow and in general the speed of particles with a spatial resolution flexible and dependent on the optical characteristics of the measuring system.
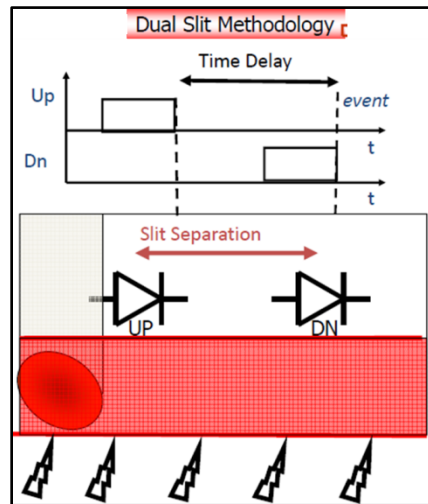
Figure. 3.8. Dual Slit Methodology

The non-invasive observation of the internal dynamics is often required in physical and biological processes and therefore must refer to an electro-optical instrumentation as an interface between the microfluidic device and the analysis system for the extraction of visual information.

The information related to localized points, and extracts the signals represent an average area under study. This allows obtaining

134

time series representative of the flow pattern, shape and size of the drops. An example of extracting information from a local area is the calculated speed through the methodology Dual Slit. It exploits the temporal dynamics and the delay between two signals related to the light transmitted through the microfluidic device in two different areas of the channel, while in this flowing particles or droplets. Another example is the measurement of the concentration of components related to fluorescent, evaluated using the principle of quenching of fluorescence. Other dynamics, such as the flow of micro-bubbles, can be extracted through the use of simple epi-or trans-illumination and brightness sensors.

Generalizing compared to the single physical or chemical principle, all measures have in common two basic actions, lighting and the acquisition of information on the brightness in localized areas of the microfluidic device respecting the spatial dimensions of the phenomenon and the need of non-invasiveness.

In the literature it is known the development of a simple device, based on micro-optical polymer and directly place of microfluidic systems transparent, realized for the characterization of optical information. It acts both as a source of light that as detector. The same principle can be improved for the phenomena analyzed here, so that it can be made a continuous monitoring of the microfluidic process, regardless of the experimental setup and the external disturbances.

The project involves the creation and characterization of polymeric micro devices, for the parallel detection of optical properties, which are applied in a spatially distributed domain, so as to characterize the phenomenon microfluidics using spatial maps and not

only local information. In particular, the immediate application of such a device is linked to the measurement of the velocity field, concentration of components in the fluids, flow pattern for two-dimensional two-phase flow in microfluidic channels or micro vessels and tissues.

These devices represent a new alternative to standard intra vital microscopy and fluorescence microscopy-*EPI* for the optical characterization of micro-channels and tissue, because they act as an interface between the phenomenon and microfluidic technology for information processing.

It often requires a filtering process to avoid, in particular measurements, interference between the light source and the fluorescence which originates from analyzed phenomenon. To implement this is possible the integration of a colored polymer layer which acts as an optical filter by dissolving coloring matter in a small volume of a polar solvent and added to the monomer of *PDMS* in the polymerization process. In this way you avoid additional layers for filtering, optimizing the processes of excitation in the wavelengths of the absorption spectrum and acquisition in the emission spectrum of the fluorescent used.

Monitoring of spatially distributed - The Particle Image Velocimetry (*PIV*) estimates the velocity profile of particles and has been widely used in experimental fluid mechanics. There are several variants of the method *PIV*, as the method of cross-correlation *2D*, the method of tracking of the particles and the correlation iterative. They are based on the analysis of images captured by *CCD* cameras with high speed

and damage output information for each point in two-dimensional space.

These analyzes can be obtained through standard processing technologies or using technologies such as analog cellular neural networks (*CNN*). They allow the extraction of the real-time parameters microfluidic using the optical information transuded by vision systems integrated technology on *CNN* and said Focal Plane Processor (*FPP*).

3.4   Examples of Implementation of Optics in Microfluidics

Examples of Implementation of Optics leaving unchanged the setup macroscopic, but changing the microfluidic device in question, it is possible to obtain many systems that, always through the thermo capillary, are able to manipulate the flows in various ways. Here are the most common examples of systems implemented optically, paying particular attention to the power of the laser beams used.

***Opto-fluidics Valve*-** For the realization of a valve optofluidics is used a device with two crossed microchannels. The oil and water flow respectively in the side channels and in the central one. Considering first the case in which the laser is off, is known experimentally that the two fluids, after meeting at the junction, giving rise to the drops of a certain size [13]. If considering the case in which the laser is switched on and comparing the two results, as seen from figure *3.9* note a substantial difference between the dimensions of the two drops.
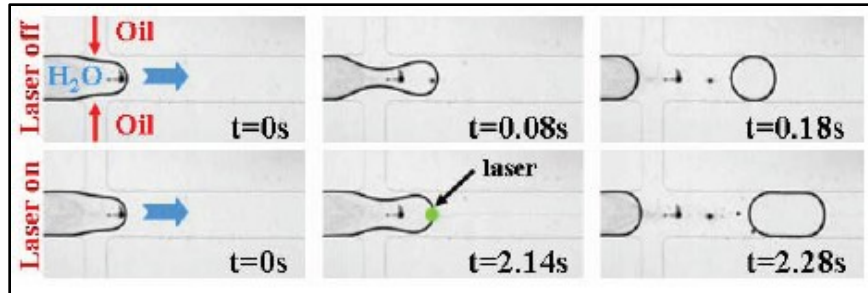
Figure. 3.9. Optofluidics valve.

This effect is due to the fact that when the drop is forming that meets the focused laser beam, it is rejected by the forces thermo capillaries and, therefore, is slowed down. This delay, also called "blocking time" T_b, increases with the laser beam power, and it is because of him that the drop size changes [19]. The power used for this experiment is equal to *P=80mW*. Prejudice the drop locked during T_b, there is an increase of the amount of water that composes it and, thanks to this effect and the valve optofluidics allows changing the frequency of emission of the droplets and also their size [13].

Sampler Optofluidics- Another way to manipulate the drops inside the device is to use a T-junction with two branches having different lengths [20]. Arrived at the T-junction, the drop is divided into two smaller droplets, the dimensions of which are imposed by the asymmetry of the two output channels.

If instead the junction was symmetric, that is, if the two arms having the same length, the drop would be divided into two equal parts. This type of symmetry can be broken by focusing the laser beam near one of the output channels; so as to obtain two streams controlled in figure *3.10*.

138
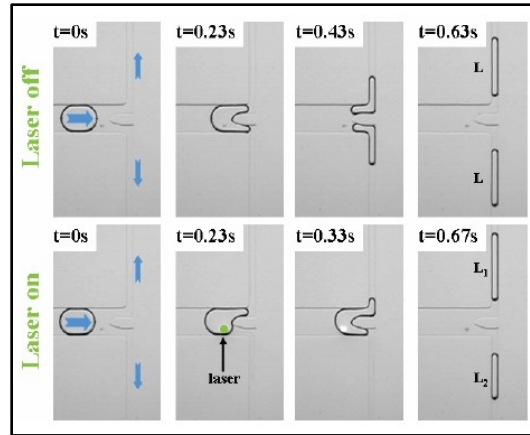
Figure. 3.10. Sampler optofluidics realized with a laser beam power equal to P = 87mW.

As is seen from figure *3.10*, temporarily blocking a drop in the vicinity of one of the output channels, it moves preferentially from the side where it meets a lower resistance and then towards the other channel. Thus the drop of departure remains divided into two parts with different lengths, L_1 and L_2 respectively.

This asymmetry can be controlled by changing the power of the laser beam. In the experiment proposed in figure *3.10* was used a power of *P= 87mW*. The threshold *P=100mW*, the drop does not divide over and is pushed completely to the other channel. This is one of the methods to realize a switcher [13].

Switcher Optofluidics- Another way to achieve a switcher, over that seen in the previous paragraph, is to use a slightly different geometry of the channel. Instead of blocking the drop close to an output channel, switches simply its trajectory to an enlargement of the main channel in figure *3.11*.
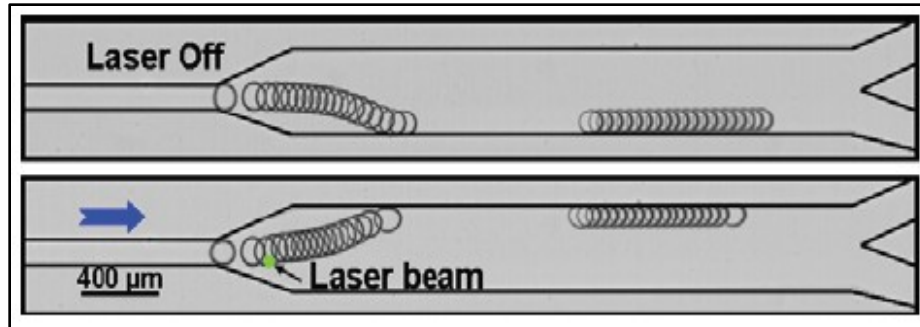
Figure.3.11. Switcher optofluidics realized with a laser beam power equal to P=58 mW

Without the influence of the laser, the drops flow through the widest part of the channel, and then take the path with the lowest flow resistance. On the other hand, turning on the laser, the flow is deflected in the opposite direction [13]. This occurs, of course, under the assumption that the laser power is high enough to deflect the entire stream, otherwise the device would behave like a sampler described above. In the experiment presented in figure *3.4* is used a power *P=58MW*.

3.5   Blocks to design an Electro-Optical System

An optical system collects the radiation from an object and modifies the geometrical characteristics, giving rise to an image; when speaking, however, of electro-optical system, includes an optical system that is able to pick up the image produced by the "optical" (optical components) upstream, by means of the use of "optical detectors".

The detectors are electronic devices that act as sensors/transducers; they acquire the image, convert it into an electrical signal, and allow viewing and editing with adequate

electronic equipment. Will be illustrated below are the main components that characterize these systems.

3.5.1 Light sources

The light source is the first block of the chain of an optical system, it part the radiation that passes through the entire system and is picked up by detectors placed downstream. The optical system has the task of modifying the light beam issued from the source, to achieve the purpose for which it was designed. The sources most commonly used are *LED,* Laser and Halogen Incandescent.

Laser - The lasers are basically constituted by an active material, from an excitation system of the material and by a system of mirrors that reflect the radiation emitted by the active material.

The active material contains atoms or molecules that, excited by a light radiation or by an electric field or by a chemical reaction, accumulate a large part of the absorbed energy for a relatively long time on energy levels higher than those of departure (population inversion). If a part of the active material drops out the accumulated energy in the form of electromagnetic radiation, this, investing other parts of the active material, still energized, causes de-energization, with a snowball effect (stimulated emission). If the active material is enclosed between two mirrors, the emitted radiation can pass more than once in the material itself still energized, favoring the de-energizing and amplified.

This description, much simplified, is already contained in the same word "*laser*", which is actually an acronym that indicates the light amplification based on stimulated emission (*Light Amplification by Stimulated Emission of Radiation*). One of the mirrors can transmit outside a small percentage (*1-2%*) of the radiation incident on it. This radiation is the laser beam which emerges from the partially reflecting mirror in figure *3.12*.
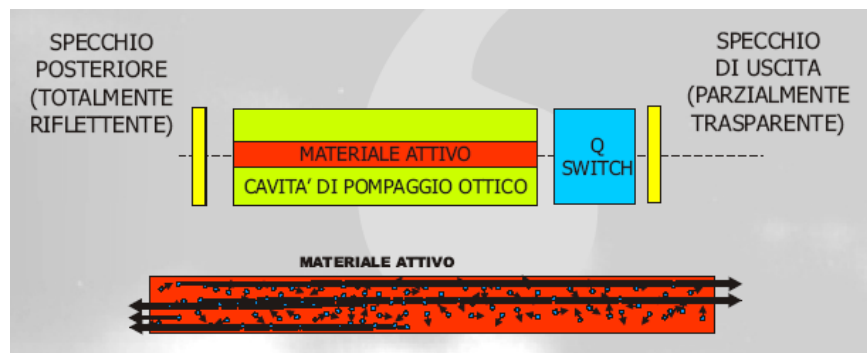

Figure. 3.12 Operating diagram of a laser

The two mirrors can be planes, one plane and the other concave, both concave. The choices of the geometry of the mirrors and their distance, together with the shape of the active medium, affecting the divergence of the laser beam. If, within the space between the two mirrors, an optical switch prevents the radiation to pass several times in the active material, provided that the energy cannot be significantly emitted for reenergizing spontaneous, it continues to accumulate as long as the excitation .

When the switch opens (Q-switch) all the stored energy is emitted in very short time. Through appropriate interventions in the optical and choice of the active medium can be obtained pulse

duration of the order of picoseconds (*10-12*sec) or femtosecond (*10-15sec*). The laser, just because they are linked to the amplification of stimulated emission, is radiation sources with very different characteristics from common sources (incandescent lamps, arc lamps, black's bodies, sun, etc). Within the laser sources include different types that emit beams not visible to the human eye. The main characteristics of the laser beams are:

➢   The great mono chromaticity, which has, in consequence, the possibility of producing and easily observe interference phenomena;

➢   The greatest energy density which can carry: amount of energy even modest, but on sections of the beam of very small area;

➢   The very low divergence, which allows the focusing of images of very small dimensions, and, therefore, of very high energy density; beam with a total divergence of *1* milli-radian, focused with a lens of 17 mm focal distance (the focal distance of 'human eye), is concentrated in a diskette *17* microns in diameter;

➢   The enormous power that can reach some lasers, due to the short duration of the pulses that can be produced. Suffice it to say that a beam that carries energy of *1* thousandth of a Joule, in a pulse of *1* nanosecond (*10-9* seconds), has a power of *1* MW.

3.5.2 Methods for the transport of the image

In many applications, in addition to providing an image of the sample taken, created through a lens or a lens system, it is necessary to process it according to the specifications and functionality that the electro-optical system must have. The changes that you can make the

images are varied, for example, you may have the need to transmit to the receiver only some wavelengths and not others, or it may be necessary to create multiple replicas of the same image, or create a beam of linearly polarized light.

There are several optical instruments, able to make changes to the images, in reality they act, not only the image but also on the electromagnetic radiation emitted by the source. In this respect, will be listed some components used for such purposes Polarizer, Filters, beam splitter, Diffraction gratings, Mirrors, Spectrophotometers and Fiber optics.

Grating
Normal to   Normal   Diffraction
Groove Face   Radiation

θ'

"0" Order
Radiation

Incident
Radiation

θ

θ

Blaze Angle

d

GRATING ANGLES & TERMS
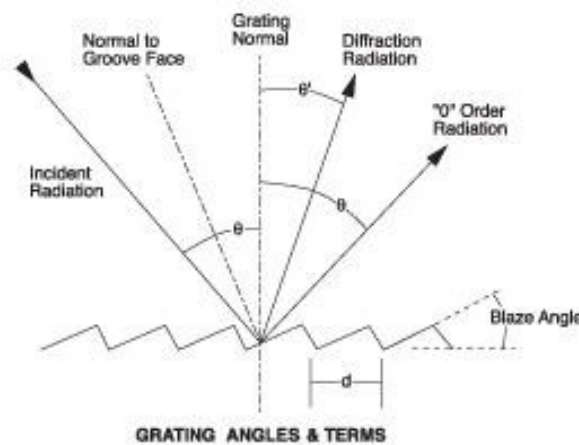
Figure. 3.13. Diagram of a diffraction grating

In figure *3.13* is an example of a grating (diffraction grating) operating in reflection, there are also the diffraction gratings able to transmit and diffract the incident ray. The gratings are the elements that characterize the spectrophotometers. With the spectrophotometer, it is studied the power transmitted, reflected and absorbed by a given sample, at various wavelengths; thanks to the aid of diffraction gratings, it is possible to go for a study of power at various

wavelengths, in that, as just said, the gratings emit rays with the emission angle dependent incident wavelength.

The optical fibers are of dielectric waveguides, consisting of two concentric layers of vitreous material extremely pure: a central cylindrical core, or core, and a cladding or cladding around it. The two layers are made of materials with slightly different refractive index; the cladding must have a lower refractive index than the core. They are used to create a guided propagation of the light radiation emitted by the source and produce a loss of light intensity negligible.

3.5.3 Optical Detectors

The detectors represent the last element of the chain constituting the electro-optical system; through them the light intensity is taken and converted into an electrical signal. The principle of operation of the detectors is based on the absorption of electromagnetic radiation by matter. There are two types of operation: "*photovoltaic effect*" and "*photoelectric effect*".

The photovoltaic effect is based on the use of semiconductors, which, by absorbing the incident radiation, generate an electron-hole pair within the material. Such a pair helps to generate the current photoconduction. The photoelectric effect is, instead, based on the emission of electrons by a material invested by photons with energy sufficiently high.

Now examine the main specifications of a detector, called "*figures of merit*". The types of detectors were listed below which

used for the realization of electro-optical systems and will be highlighted their most distinctive features:

Photodiodes: the detectors are most commonly used; depending on the material used are available detectors for *UV*, *NIR* and Thermal Infrared (*3-14µm*) offer high sensitivity and fast response time (wide frequency band power).

They can be used in both photovoltaic and photoconductive configuration. The first configuration features, in general, better performance in noise but is worse in the frequency response and dynamic.

CCD (charge coupled device): are based on storage dynamic and on the subsequent removal of a given electric charge in a series of *MOS* capacitors. Are quantum detectors with low noise and dark current, are therefore particularly suitable for very long exposure times. Typical applications include spectroscopy and fluorescence microscopy.

There is a specific type, called "Back Illuminated", obtained by thinning the detector by the side of the substrate (the rear of the device) and then using the rear surface and not the front for the collection of the signal. In this way, attain to higher values for the *QE* and a spectral response wider toward the *UV*.

C-MOS: quantum detectors are characterized by a high noise, offset by a very wide power band. They are used for "imaging" high-speed (*500-1, 00,000* frames per second).

Photomultipliers*:* are available to both individuals and small matrices. They offer high collection area and a high gain, have good dynamic and electric band, on the other hand require high bias voltages. As a result of a complete assembly (*photomultiplier + housing + power + amplifier*) can be expensive and tricky to use.

The spectral response depends on the material used for the photocathode (front surface). The photodiodes which performance very close to those of the photomultipliers, but to use much more simple, limiting their use only to cases where it is essential to their sensitivity.

3.6   Experimental Optical Workbench

As described in the preceding paragraphs is a description of the main parts that constitute a system optofluidics in macroscopic terms. The transition from the Macro-Micro-Optofluidics to Optofluidics has generated the need of having embedded system able to realize perform, in a much more precise and accurate, as well as at the microscopic level, a large number of microfluidic applications.

3.6.1 Basic Optical Tweezer System (OTKB)

The basic idea is to have a system that allows image detection of microfluidic systems that integrates the function of optical photo detection implementation, and which can nevertheless be easily modifiable in terms of setting to be able to integrate different functionality. In particular, in figure *3.14* is shown one of the possible configurations obtainable with such a system characterized by:

White light source: necessary to illuminate the sample (microfluidic chip for example).

Condenser Lens: White receives the light from the source and the condensate drain to the Objective Lens.

Sample: the sample under examination, the microfluidic chip.

Sample Stage: this is a shifter that allows you to move the sample in 3 directions (X, Y, and Z) between the condenser and the objective lens.

LD & TEC Controller: control the laser and regulate temperature.

CCD Image Detector: allows image capture from the focused light beam that is playing the spot illuminated sample.

Fiber Port: is the input of the optical fiber connected to butterfly mount generates in fact the laser beam.

Di-chronic Mirror and Beam Expander: through them the laser reaches the sample, and the image reaches the CCD.
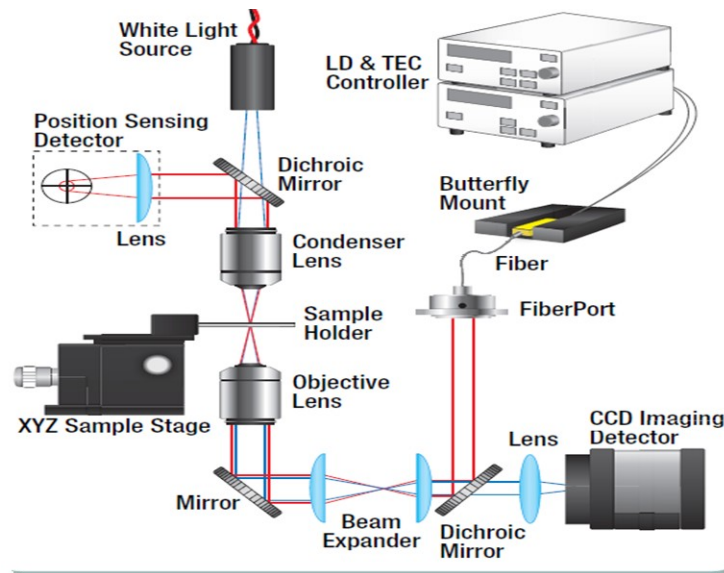
Figure 3.14 Assembled Setup of OTKB

Thorlabs offers an optimal solution for the realization of a system macro optofluidics integrated. The Optical Tweezers or traps as they are often called have become an important tool in a wide range of areas such as bioengineering, materials science, physics, and for their ability to retain and manipulate micro particles to measure the forces in piconewton (*pN*).

The nature modular of system makes it suitable for advanced teaching and research laboratories because of the ease with which the setting can be changed. Since the system is constructed using standard mainly components Thorlabs, it is easy to modify. While the *OTKB* kit includes all components necessary to build an optical trap, the module for measure *OTKBFM* of force can be achieved to allow quantitative measurements. How many optical systems trapping, this is based on a design inverted microscope. Figure *3.15* shows in detail

the system in question. The laser source is a diode laser trapping of single mode at *980 nm* stabilized.

An integrated part *TEC* (**1**) and a thermistor is possible to control the temperature of the laser in a precise manner when mounted on the support *LM14S2* (*connection butterfly*) and controlled via *LDC210C* (**1**) and a temperature controller *TED200C* (**1**). The combination of these two controllers has been chosen to ensure that the output power (*330mW* max) of the laser is extremely stable, which is of fundamental importance to maintain a constant force trapping.

The Fiber Port (**2**) collimates the laser output trapping. The Fiber Port a collimator is versatile in that it allows that the collimation of the spherical lens allows precise positioning in *5* degrees of freedom (*X, Y, Z,* Pitch and Yaw). For applications that require high sensitivity and precision, it is possible to perform an alignment so that it can be linearly set the orientation of the collimated beam

The two pairs of achromatic lenses *ACN254-050-B* and *AC254-150-B* (**3**) do so to expand the collimated laser beam by a factor of *3*.

The dichroic mirror (**4**) which is mounted in the central part *C6W* reflects light *980 nm* (trapping source) allowing the passing of visible light.

The visible light from the *LED* light source (**9**) illuminates the sample which is then taken up on the *CCD* (DCU224C) (**5**) color with a resolution of *1280* x *1024* pixels. A further dichroic mirror in the light path in combination with a filter that prevents the reflected light from the laser 980 nm ports in saturation the image seen by the *CCD* detector. An objective lens (**6**) Nikon of magnification equal to *100X*

is used to focus the laser beam at *980 nm* to form the optical trap. The diameter of the trap limited by diffraction is estimated at about *1.1μm*.

A *10X* objective Nikon is used as condenser and collimates the beam after the optical trap. The sample Stage (**7**) is constituted by a support which can accommodate microscope slides mounted to a translator *3* axes (*X, Y,* and *Z*) which presents the following displacement capacity:

• *2* "(*50mm*) and *2.4*" (*60mm*) perpendicular to the optical path. This makes it easier to load the sample grossly and place it near the trap.

• *4mm* travel in *X, Y* and *Z* with the differential modular *Nano-max MD311,* micrometric translational unit with manual shift knobs for providing *0.5 mm / rev*.

• *300 microns* in *X, Y* and *Z* with the knobs differential (*50 pm / rev*) *3*-axis differential.

• *20pm* in the directions *X, Y,* and *Z* using the piezoelectric actuators (*20nm* resolution without the use of feedback from the internal strain gauge sensors, resolution of *5nm* using strain gauges for internal positional feedback). Three T-Cube Piezo-drivers are included in the kit. The possibility of such a translation is obviously related to the need for very precise positioning during the processes of implementation laser.

The visible light emitted from the *LED* (**9**) passes through the di-chronic mirror and illuminates the sample, while the laser beam *980nm* is reflected towards the optional module for force

measurements *OTKBFM* (if the *OTKBFM* is not used, the laser is locked by a cap.

The form for force measurements *OTKBFM* (**10**) contains the hardware necessary to calibrate the trap. The iris on the back focal plane of the lens (used as condenser) is taken on the position detector Quadrant (*QPD*) with an objective lens focal length of *40mm* biconvex with *BK7*.

The detector position is characterized by a rise time of *40ns* and a bandwidth of *150 kHz*. The signal generated by the *QPD* is sensitive to the relative displacement of the particle trapped by the laser beam. As a result the detector output can be used to calibrate the position, stiffness, and the strength of the optical trap.
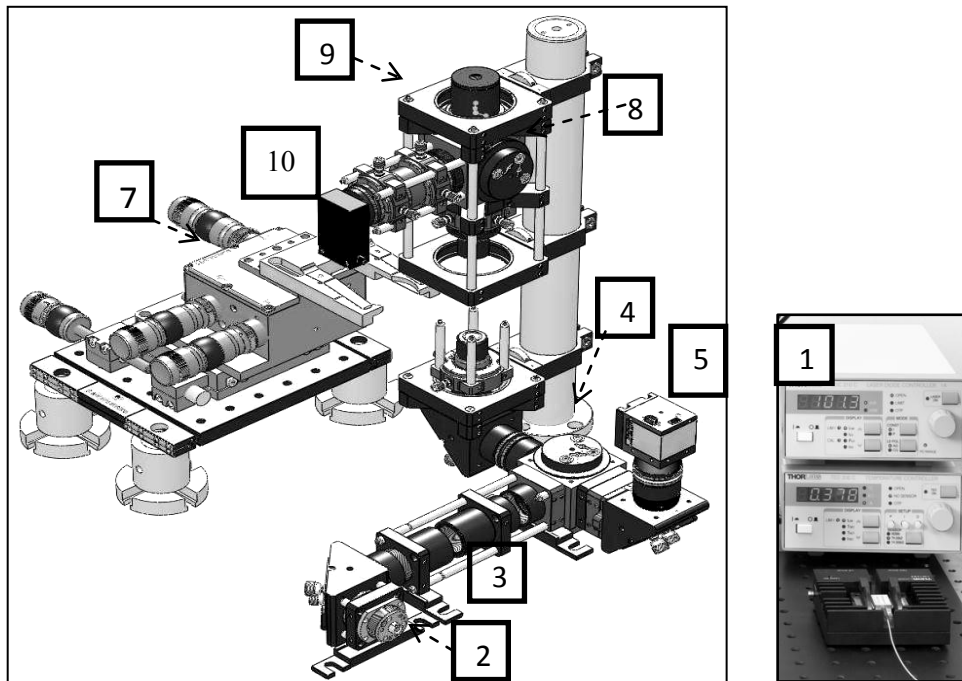
Figure. 3.15 OTKB Thorlabs

3.6.2 Customized OTKB

The integrated system made available from Thorlabs born primarily to perform the function of optical trap. However it has been an object of study the modification of the starting setup described above.

The basic idea was to take advantage of the modularity of the system to carry out investigations of different types. In particular, there were two photodiodes in order to perform function of detection. As you can see in figure *3.16* and using a dichroic cage cube, you get a split white light from an *LED*, for already the *CCD*.
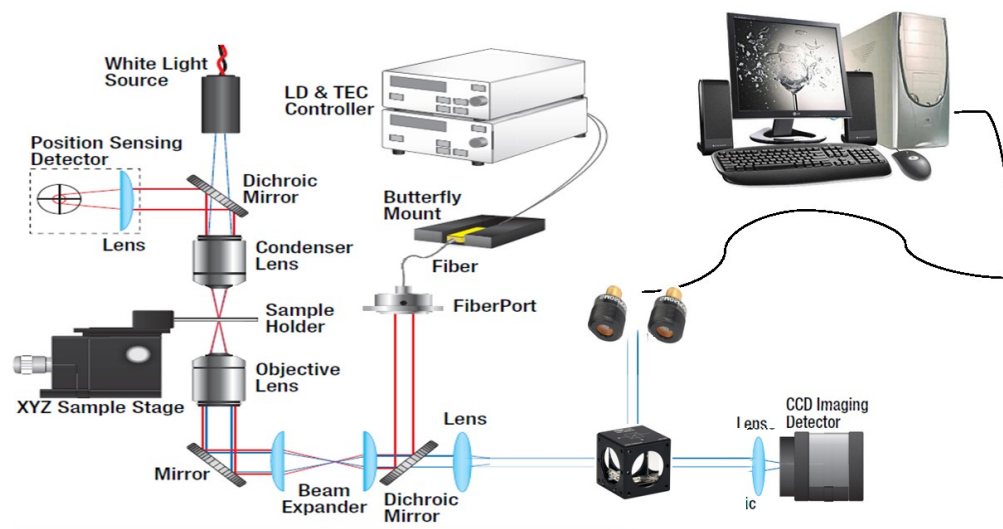
Figure. 3.16 New setup using the dichroic cube cage CM1-BS01

In this way it is possible to observe how the brightness varies examined on the chip, and then inside the microchannel allowing the distinction between different flows of the fluid of more detailed qualitative and quantitative analysis were carried out to characterize

the devices; In figure *3.17* shows the final setup assembled in the laboratories of the University of Catania.
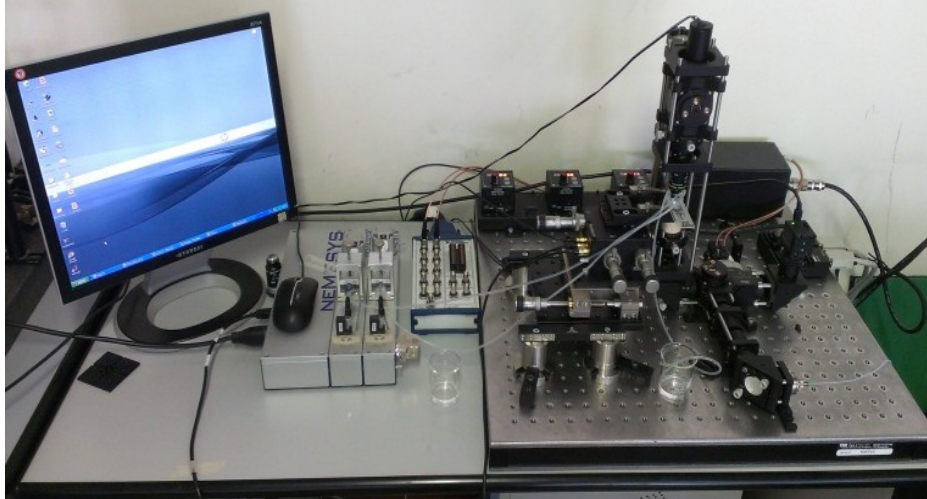
Figure. 3.17. Embedded Micro Optofluidics

3.7   Static Characterization of Optical Detection

To be able to give a correct interpretation, to the behavior of two-phase flow within microchannels, it was necessary to characterize a priori the detection system used for this purpose.

The monitoring of two-phase flow within microchannels represents a study of great interest in the field of microfluidic. Of two-phase flow is discussed in section-*2* of the first chapter, but wanting to resume briefly the definition that was given, "the two-phase flows are characterized by the presence of two phases of the same component and represent the simplest case of multiphase flows. To be precise it should also use the term multi component to indicate the flows consist of chemically different phases belonging to elements ".

How many times repeated the system *OTKB*, before being used for the implementation laser, requires a careful characterization in order to interpret the images from the *CCD* and the light signal coming from the white *LED* and captured by the photodiodes. In particular, as the chapter title suggests, will be given the results obtained by the experimental work conducted on the behavior of flows of air and water within microchannels of different sizes and geometries.

3.7.1 Positioning Photodiodes

The first step towards the characterization of the photodiodes has been their positioning in the system *OTKB*, not so much qualitative, rather in terms of position relative to the beam splitter, i.e. to diachronic cage cube.

(a)

(b)
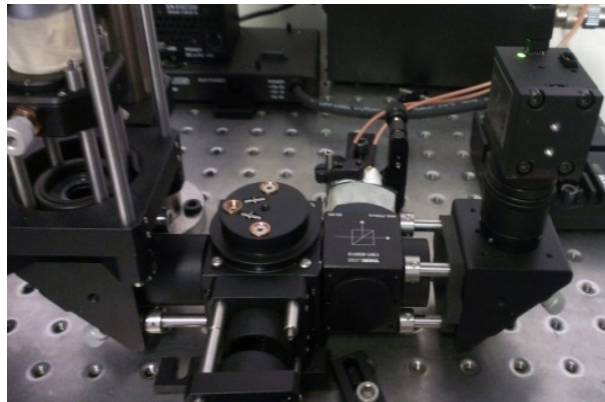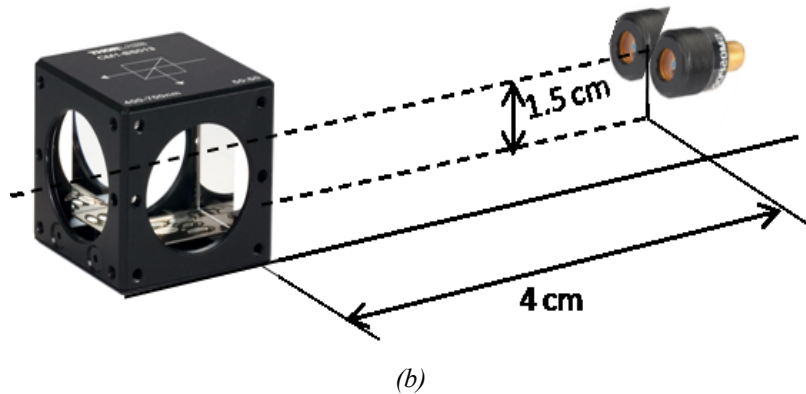
Figure. 3.18. (a) photodiode setup (b) Photodiodes Position

As can be seen from figure *3.18(b)* the photodiodes have been positioned at a distance from the beam splitter equal to 4 cm. In terms of height from the breadboard, instead, they are located at *1.5cm* from the base. They are also firmly positioned next to one another.

However, to avoid disturbing effects of the brightness has built a black cylinder that, just interposed between splitter and photodiodes, avoids that the measurements are affected by noise, as well as the white light to converge precisely towards the photodiodes, thereby increasing significantly the sensitivity to light variations, reducing the effect of ambient light measurement figure *3.18(a)*.

3.7.2 Terms of Reference Signal

In order to perform the various experimental tests has been appropriate to realize the sensitivity of the photodiodes used. It is also necessary to specify that with photodiode-*1 &2* shall be understood looking at them from above respectively one on the left and one on the right.

To this end, an analysis of the signals was Conducted from the photodiodes Subjected to different lighting, in Particular was useful to

observe the variation of the signal in a first time with the normal presence of the white light emitted from the *LED* to hit the target, while in a second time the signal was measured in the total absence of light, simply by interrupting the light beam by closing a cover lens placed between the *LED* and the condenser.

From this analysis have Emerged that date have allowed us to continue the experimental fact of knowing reference values in terms of brightness. In Figure *3.19* shows the trend of the light signal obtained by carrying out a recording of *20* seconds, in the absence of any microchannel interposed between condenser and objective for about *10* seconds while keeping the lens cover closed, and open for the remaining time.
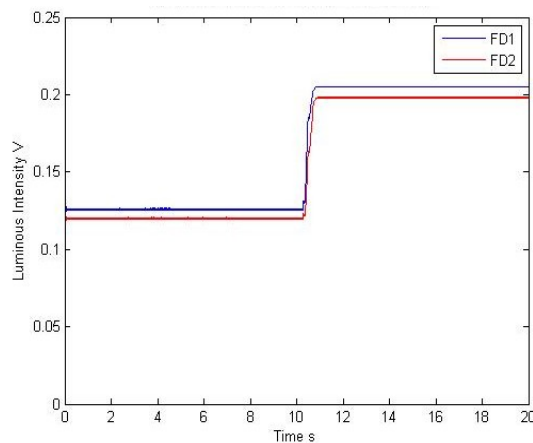
Figure. 3.19 Objective comparison of closed – open

As you could imagine, the two cases have different values, in particular:

The absence of light - The measured average value of photodiode-*1* is *0.1258V* and the photo diode-*2* is *0.1200 V*.

The presence of light - The measured average value of photodiode-1 is *0.2015V* and the photo diode-*2* is *0.1940 V*.

The obtained result shows a difference between the two cases, in which in the absence of light the two photodiodes detect roughly the same brightness distancing of just *5mV* and therefore produce the same signal; in the presence of light the two photodiodes characterize the brightness with two different values of course a value not overly different.

Interposing the microfluidic chip between condenser and objective was repeated the previous experiment, observing a similar trend of course, but in particular of slightly different values.
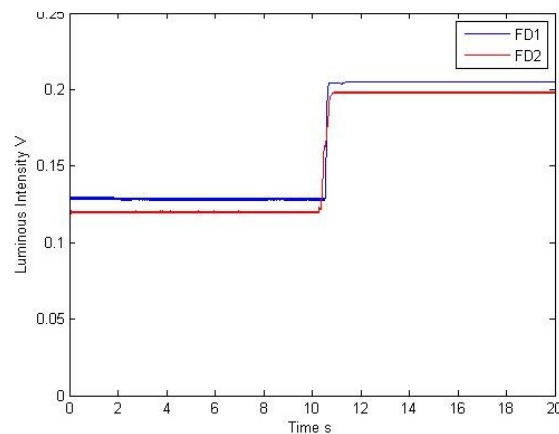
Figure. 3.20 Objective comparison of closed - open channel interposed

The results obtained show that:

The absence of light- The measured average value of photodiode-*1* is *0.1286V* and the photo diode-*2* is *0.1211V*.

The presence of light- The measured average value of photodiode-*1* is *0.2005V* and the photo diode-*2* is *0.1951V*.

3.7.3 Relative distance between two photodiodes

Despite the two photodiodes have been set alongside one another, they look at two different points, being the photosensitive elements between their spaced about *1cm*. This is the explanation for the previously discussed analysis showed a difference between the brightness perceived by the two photodiodes, subjected to a constant light intensity.

It was therefore interesting, beyond that necessary to calculate this distance and moreover the direction along which reflects the positioning of the two devices.
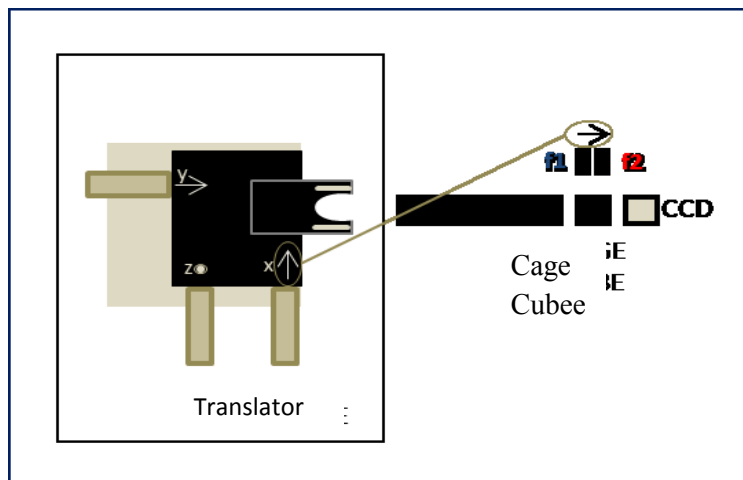
Figure.3.21. Long physical distance y between the two photodiodes f1 (in blue also the corresponding signals) and f2 (in red) translates into an optical distance along the x direction of the side shift

The photodiodes *f1* and *f2* (in Figure *3.21* is made the distinction between the two that is also reflected in the signals) are set

next to each other at an equal distance from the base. The view from above figure *3.21* highlights that are physically arranged along the *y* direction of the shifter but, through the optical system, this distance results in a projection along the *x*-direction, orthogonal to *y*. The distance between the two points viewed by the two photodiodes was calculated by placing a chip on the sampler and observing a microchannel by *320μm*.

By placing such a channel as has been carried out in which a measure in real time you move from one edge of the microchannel, observing that it responds to the extremes of a single photodiode. Therefore the distance sought was estimated around the value of *300μm* about.
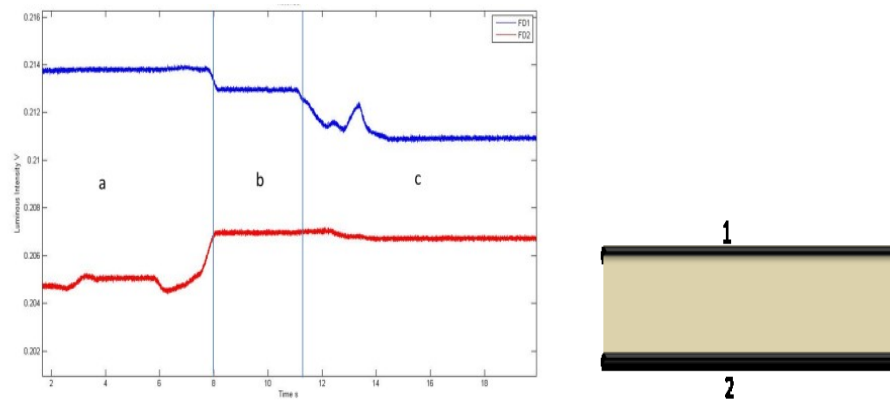
Figure 3.22. (a) Behavior on the edge 1; (b) behavior within the channel. (c) Behavior on the edge2

In figure *3.22* see the trend of the signals from the two photodiodes using a slide as the sample on which was printed a colored mark. Translating the slide along the *y* direction of the side

shift the two devices provide the same response, trying the actual projection of the two points shopped along the *x* direction.

Starting from the results obtained from the photodiodes, having carried out a detailed characterization, was much more significant characterization of air-water two-phase flow in microchannels. However, figure *3.22(a)* shows an enlargement of the chip with the aim of offering a greater degree of understanding when in the following section will mention the various channels examined.
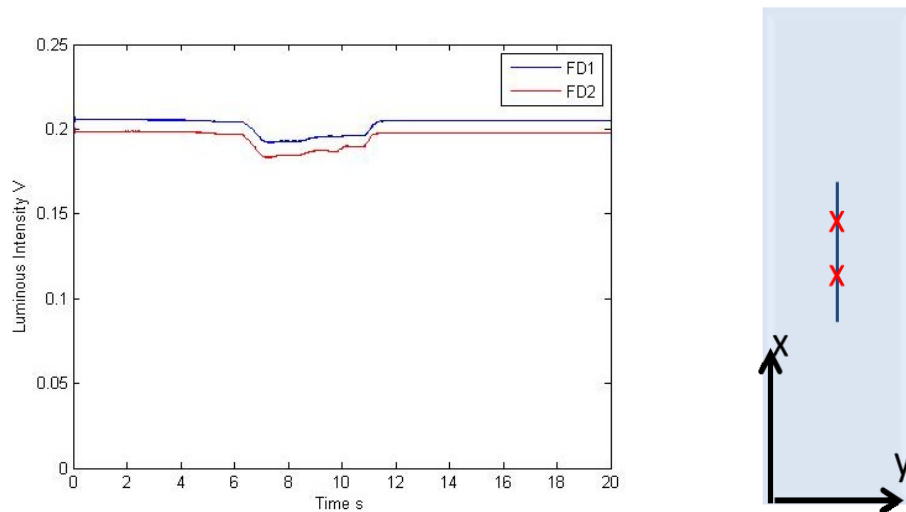
Figure. 3.23 – displacement along the y direction of the side shift

Referring to the experiments you can trace the guidelines followed in terms of case studies. For each channel was monitored the progress of the brightness in three different cases are airflow; water flow and two-phase flow water-air. In addition, for each fluid were performed various tests differentiated by different flow rate set through syringe pumps.

The following table *3.1* shows various combinations of flow rate of air and water each linked to a specific frequency. Based mainly on the microscopic size of the channels, and having the need to highlight the most significant aspects, has carried out an analysis with flow at low frequency, using precisely flow rate corresponding to frequencies from 7*Hz* to lower values. The following table has been examined and used as a source for the proper use of air and water flow rates.

water frequency [Hz]	flow rate [ml/min]	air frequency [Hz]	flow rate [ml/min]
5	1,57	5	1,2
7	2,26	7	1,71
10	3,3	10	2,5
12	3,96	12	3,03
15	4,87	15	3,81
17	5,39	17	4,3
20	6	20	5
22	6,2	22	5,44
25	6,4	25	6,04
27	6,4	27	6,42
30	6,3	30	7,02
32	6,12	32	7,43
35	5,7	35	8,05
37	5,4	37	8,46

Table 3.1 Water Flow rate and Air flow rates in time and frequency.

3.8   Setup of Microfluidic System

The optical monitoring discussed in this chapter was conducted using the system instead of custom mentioned in the previous chapter.

In addition to the integrated system, which plays a major role in the instrumentation worked, the main devices used in the experimental phase were mainly:

• Photodiodes;

• Syringe Pump;

• Acquisition Board;

• Microfluidic Channels;

• Objective Lens;
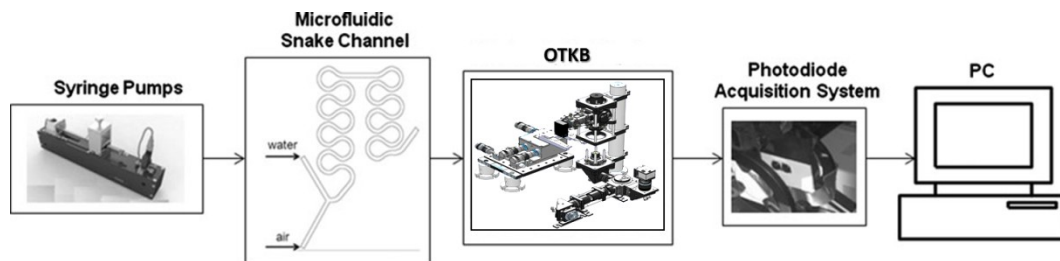
Figure. 3.24. Setup used for the optical monitoring

Photodiode - In opto electronic a photodiode a particular type of photo diode detector that functions as optical sensor exploiting the photovoltaic effect, i.e., capable of recognizing a specific wavelength of the electromagnetic wave incident (absorption of the photon) and to transform this event in an electric current signal by applying to its ends an appropriate electric potential. It is therefore a transducer from an optical signal to an electric signal.

In terms of technical specifications table *3.2* summarizes the characteristics of the photodiodes used for monitoring while figure *3.25* shows its response to the varying of the wavelength.

SM05PD2A

Figure. 3.25 – Photodiode SM05PD7A

Item #	Detector	Rise/Fall Time (ns)	Active Area (Dimensions)	NEP $(W/Hz^{1/2})$	Dark Current	Spectral Range (nm)	Material	Junction Capacitance
SM05PD7A	FGAP71	1 / 140[b]	4.8 mm^2 (Ø2.5 mm)	1.3×10^{-14}	40 pA[c]	150 - 550	GaP	1000 pF @ 0 V

Table. 3.2. Characteristics of Photodiode
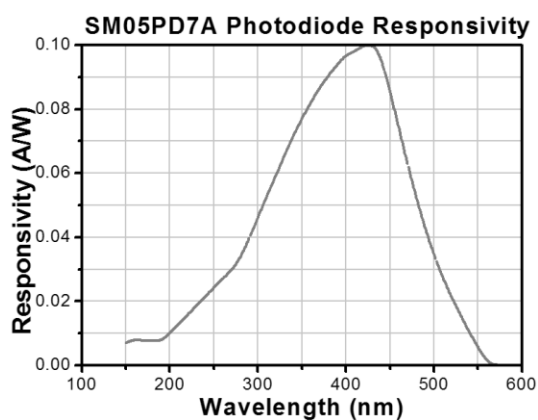
Figure. 3.26 – Response of SM05PD7A to vary the wavelength

Syringe Pump - The monitoring of flow in microchannels can be realized only through an appropriate control over the velocity of the fluids used, adjustment obtained with the aid of syringe pumps. For the purposes set have been used in particular syringe pumps offered by Nemesys.

They are the 'ideal for generating fluids of the order of milliliters or even nanoliter per second. These syringe pumps are ideally suited for high precision dosing of micro volumes in the range

of nanoliter. The unit of *PID* control of the actuators of each module ensures an extremely smooth movement of the piston of the syringe and prevents effects of jamming of the piston within the syringe.

This ensures a very high accuracy and the absence of pulsation in the fluid streams generated. The 'universal fixing syringes offers great flexibility in the choice of the syringe, thus allowing using one for your application.
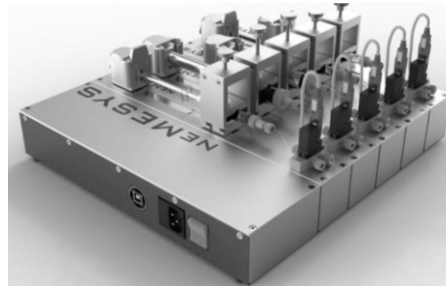
Figure.3.27. Syringe Pumps

Acquisition Board - The photodiodes used on the one hand have the photosensitive devices; on the other hand have a *BNC* type connector. To acquire and then analyze the signals from these sensors, capture card directly interfaced to the *PC* via *PCI 6024-E* of National Instrument. In particular, the user interface of the card is just a *BNC* (*BNC 2110*); with *I/O* analog and digital (used *AI4* and *AI5*). In figure *3.28* is a screenshot of the interface, for technical data much more effective to use the datasheet related to it.

Figure.3.28 – NI BNC 2110 Acquisition Board

Microfluidic channels - The microfluidic chip used is represented in figure *3.29*. It is a chip of Thinxxs Micro technology, *SMS0104*. This chip has a total of five continuous-flow mixer. The slide is made of cycle-olefin-copolymers (*COC*), which combines good optical properties with good biocompatibility and chemical resistance to most acids and bases. A series of connectors is available and allows you to connect standard tubes or typical laboratory instruments such as pipettes or syringes at the entrance of 'SMS0104.
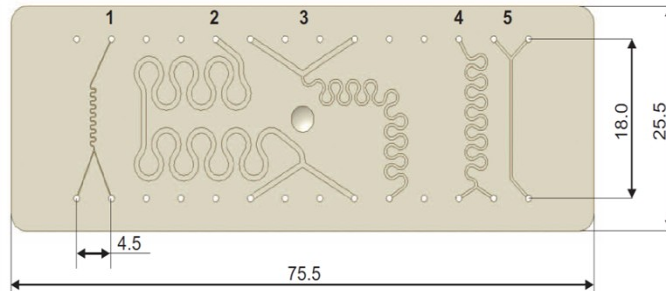
(a)
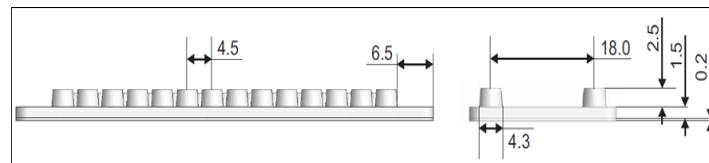
(b)

Technical Specification	
Max. Inlet pressure	Min. 6000 hPa (-87 psi)
Operating Temperature	10°-50° C
Media Temperature	10°-50° C
Storage temperature	10°-50° C
material	COC

(c)

Dimension				
Channel no.	Length *(mm)*	Width/depth *(µm)*	Internal Volume *(µL)*	Max. particle size *(µm)*
1	21	100	0.2	5
2	121	640	49.6	5
3	66	320	6.8	5
4	50	320	5.1	5
5	16	320	1.6	5

(d)

Figure.3.29 – (a) SMS0104 Snake Mixer Slide (Microfluidic Chip) (b) bottom view of the microfluidic Chip (c) technical specification of the chip (d) dimension of the microchannel

Objective lens -A further device was done in terms of objective lens. Thorlabs provides all' *OTKB* together, as previously stated, an oil immersion objective by Nikon *100x* magnification (magnification=M) undoubtedly useful for the purposes of implementation laser allowing to act on restricted areas really the order of tens of microns.
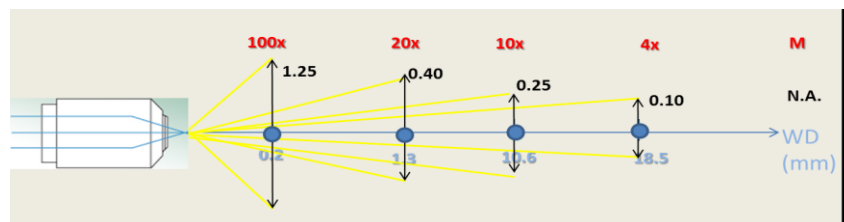
Figure. 3.30 – Summarizing scheme of the characteristics of the various objectives

Objective	Magnificent (*M*)	Numerical Aperture (*NA*)	Working Distance (*WD*) [*mm*]
Nikon E Plan	*100x*	*1,25*	*0,23*
Old Objective	*20x*	*0,4*	*1,3*
Olimpus Plan	*10x*	*0,25*	*10,6*
Olimpus Plan	*4x*	*0,1*	*18,5*

Table. 3.3 Objective Lens.

In order to observe therefore larger areas, or even the entire diameter of the microchannel, was used an objective of which was already in possession, characterized by *M=20x*, with which we are able to observe diameters of size up to *320μm*. Therefore moving in this direction, it turned towards the purchase of other instrumentation and especially of two new targets, whose technical characteristics, together with those of previous mentioned, is shown in table *3.3*.

3.9   Flow Pattern in Microfluidic Chip

A first analysis was conducted in order to disclose the levels of light intensity within the various channels to highlight any differences between them. Below are the graphs relating to the light intensity measured by the two photodiodes comparing particularly the cases in which the channel is filled with air or filled with water, naturally in the absence of a net flow, i.e. with fluids "*latches*" within the same microchannel.
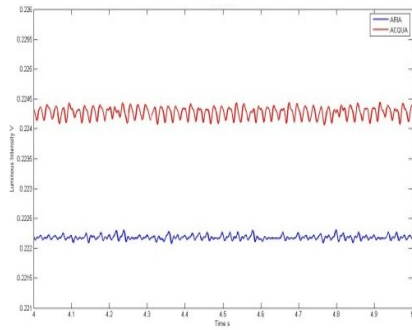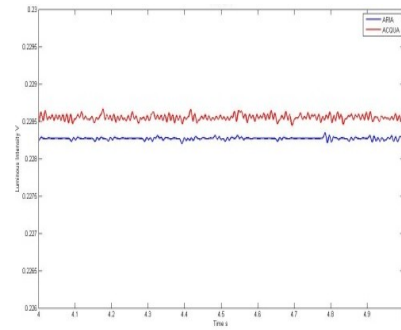
(a)   *(b)*
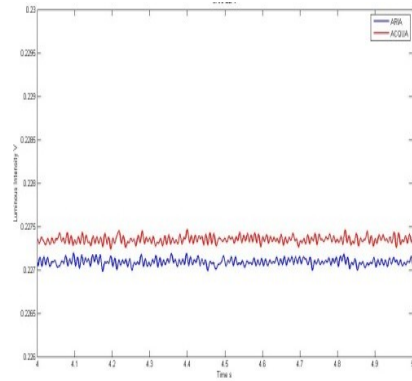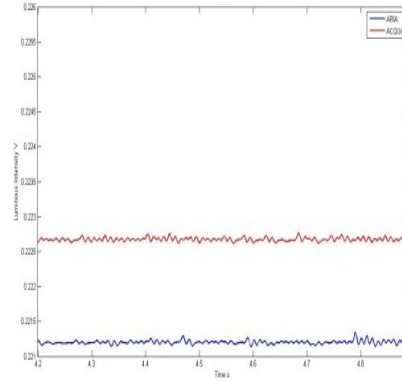
(c)   *(d)*

Figure. 3.31 – no flows - air (blue) water (red) for the photodiode-1 (a) microchannel-2 (b) microchannel-3 (c) microchannel-4 (d) microchannel-5
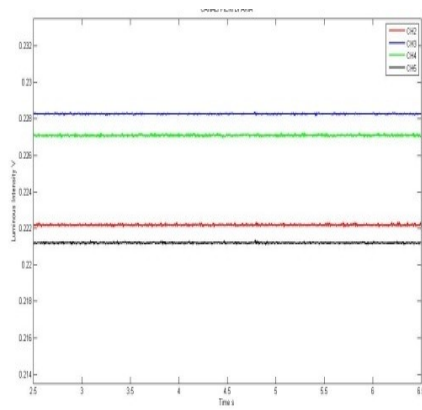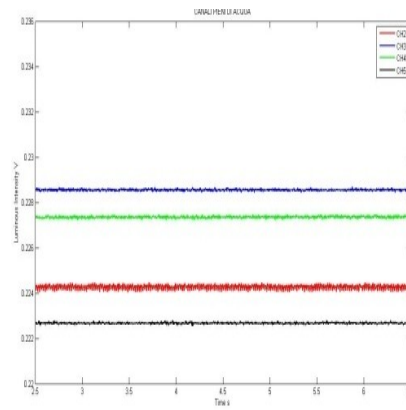
(a)   *(b)*

Figure. 3.32 (a) comparisons between the values for air in the 4 channels analyzed. (b) Comparisons between the values for water in the 4 channels analyzed

It was found that the brightness, to be with zero flow, depends on the channel under observation, not only in terms of size, being the channels *3*, *4*, *5* of equal diameter, but also in the form that they present. The channel-*2* diameter is *640μm* has found a greater separation between the brightness values related to 'air and water in figure *3.32*.

Channel 2- The measured averaged value of air is *0.2222V* and the measured averaged value of water is *0.2243V*.

       Δ=2.1mV

Channel 3- The measured averaged value of air is *0.2283V* and the measured averaged value of water is *0.2285V*.

       Δ=0.2mV

Channel 4 - The measured averaged value of air is *0.2271V* and the measured averaged value of water is *0.2274V*.

       Δ=0.3mV

Channel 5- The measured averaged value of air is *0.2212V* and the measured averaged value of water is *0.2227V*.

Δ=1.5mV

3.9.1 Straight Channel (*320μm*)

The microchannel*5* is not only geometrically, but also in terms of diameter different from the channel *2* previously analyzed. This drastic reduction in size has resulted in an equal decrease in the flow rates used.

Microchannel5-320μm - In this channel, as well as in others of equal size, it is still preferred to analyze three different flow rates, but discarding the analysis to *7Hz* (*2.26 ml/min* Water - *1.71 ml/min* air).

Air Flow - In a manner similar to what has been done for channel*2*, but with the devices described at the beginning of the paragraph have been studied flows having the following flow rate:

➢   *1.20ml/min →frequency =5 Hz*
➢   *0.12ml/min →frequency =0.5 Hz*
➢   *0,.012ml/min →frequency =0.05 Hz*

Water Flow - With regard to the flow of air used in this channel are shown the following flow rate:

➢   *1.57ml/min →frequency =5 Hz.*
➢   *0.157ml/min →frequency =0.5 Hz.*
➢   *0.0157ml/min →frequency =0.05 Hz.*
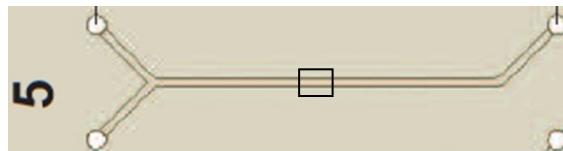
Fig. 3.33 Microfluidic channel 5 width/depth - 320μm

Bubble flow -From the combination of the flow rates of air and water mentioned above, the two-phase flow was monitored as a function of its speed.

In particular, trying to keep along the same line for the channel from *640μm* and then for others from *320μm*, the figures *3.34* shows the FFT and the signals of light intensity to vary the flow rate. The better interpretation were exposed below in the references signal water/air at the given flow rate.

(a)

(b)

(c)

(d)

(e)

(f)
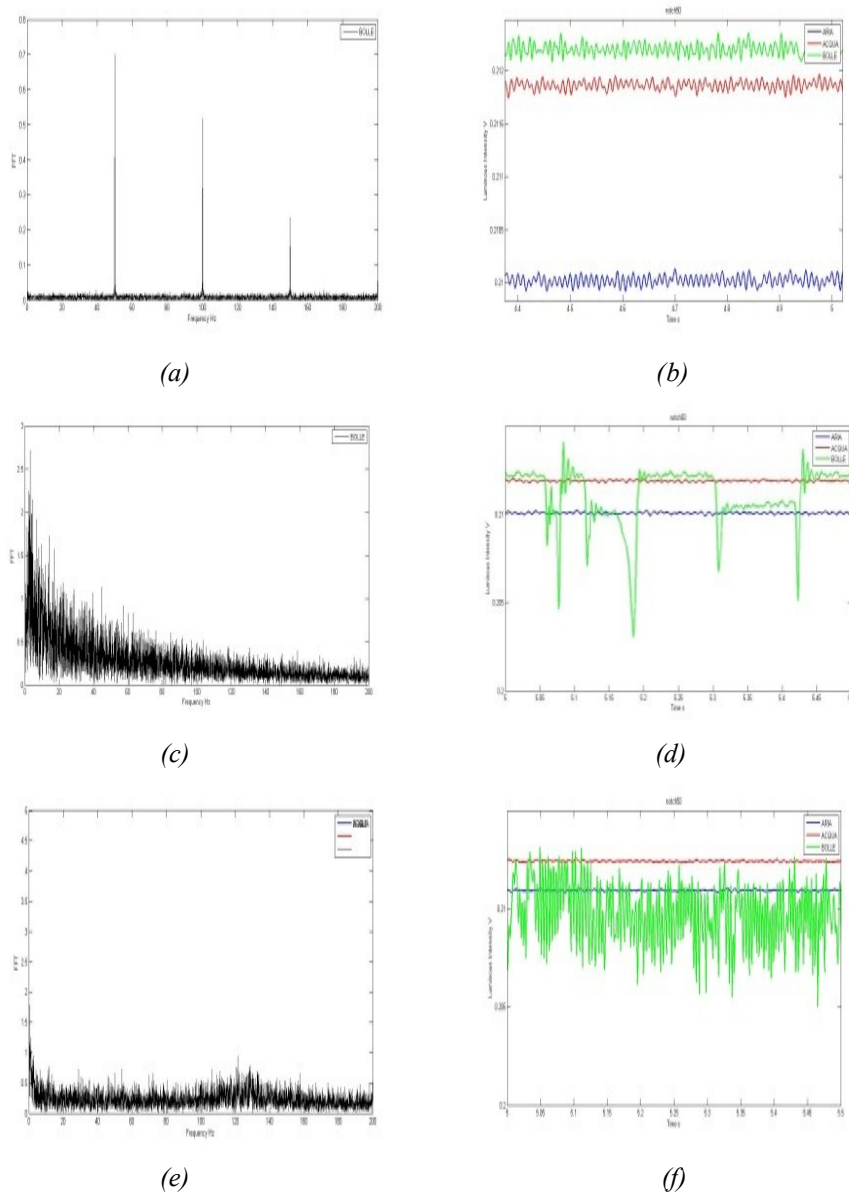
Fig. 3.34. (a)-(b) Experiment-3 FFT signal and microfluidic time series signal(c)- (d) Experiment-2 FFT signal and microfluidic time series signal (e)-(f) Experiment-1 FFT signal and microfluidic time series signal

172

In this channel, as well as the rest was observed in the other, albeit with minor differences, it is able to identify two basic behaviors:

• One puts in evidence a stream of bubbles or less regular depending on the geometry of the channel and this occurs for flow $rate > 1\,ml/min$;

• The other highlights a trend much slower dynamically, that does not represent a continuous stream of bubbles, but irregular events, alternating with long bubbles, or streams of water.

3.9.2 Serpentine Channel (*640μm, 320μm*)

Microchannel2-640μm- The first channel analyzed is shown in figure *3.35*. The rectangle shows the portion of the channel examined.
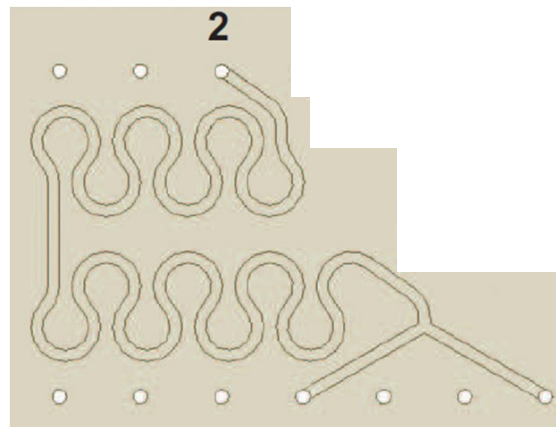
Figure. 3.35 Micro-Channel2

Air flow- The monitoring of the air flow has been addressed by examining mainly *3* different flow rate:

➢ **Experiment1:** 1.71 ml/min→*frequency* =7 Hz

➢ **Experiment 2:** 1.20 ml/min→*frequency* =5 Hz

➢ **Experiment 3:** 0.12 ml/min→*frequency* =0,5 Hz

Water flow – the analyzed three levels of flow rate for the flow of water corresponding to the three frequencies used for the air flow.

➢ **Experiment1:** 2.26 ml/min→*frequency* =7 Hz

➢ **Experiment 2:** 1.57 ml/min→*frequency* =5 Hz

➢ **Experiment 3:** 0.157 ml/min→*frequency* =0,5 Hz

Bubble flow - Similarly to what described for the flows of air and water, the study of two-phase flows constituted by the two fluids have been properly carried out using the three combinations of flow rate mentioned above.

The following are the signals of luminous intensity and the relative Discrete Fourier Transforms (*FFT*) for the three cases analyzed.
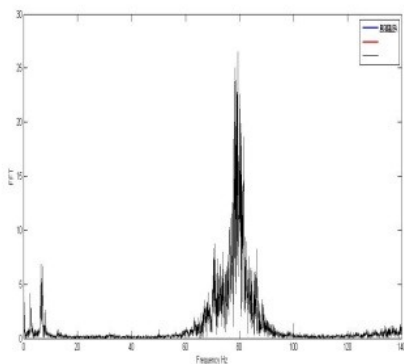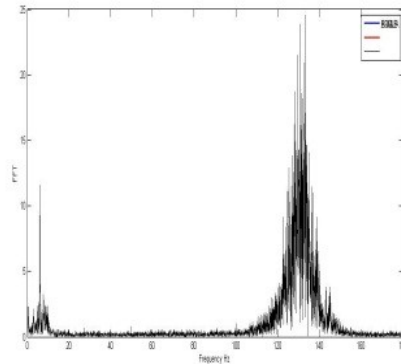
(a)   *(b)*
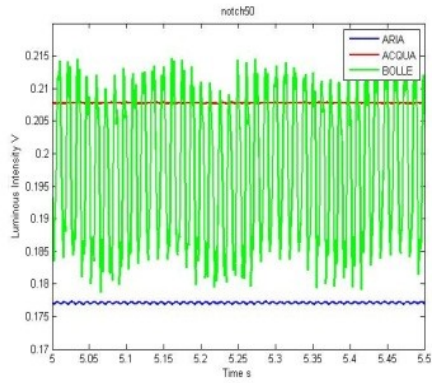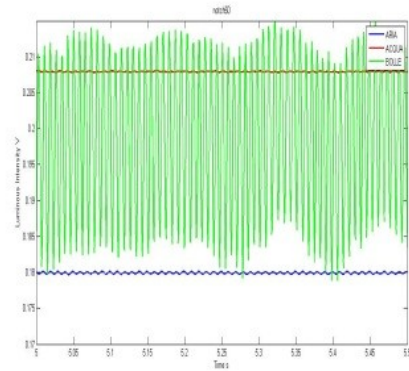
(c)   *(d)*

Figure. 3.36. Results for $flowrate > 1\,ml/min$: experiment-2 on the left and on the right experiment-1
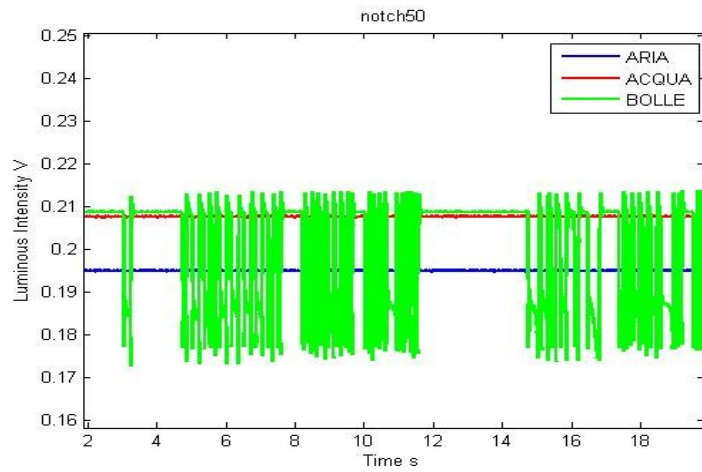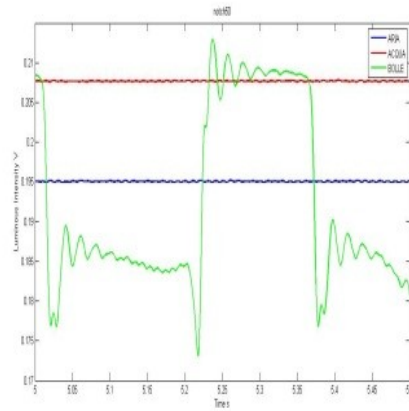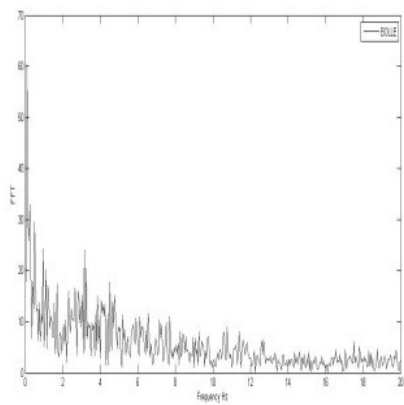

Figure. 3.37 FFT and signals obtained using the data of experiment 3

175

Figures *3.36* and *3.37* show a substantial difference to the different flow rates used. In particular, the *FFT* are clearly two different behaviors:

• For *flow rate>1ml/min* is a well-defined pattern, in which the light signal oscillates between the reference water to the air;

• For *flow rate<1ml/min* it has a pattern which does not characterize a continuous stream of bubbles, and this difference is significant in the *FFT*.

Analyzing in more detail the signal for an interval less than one realizes Circulation oscillatory.
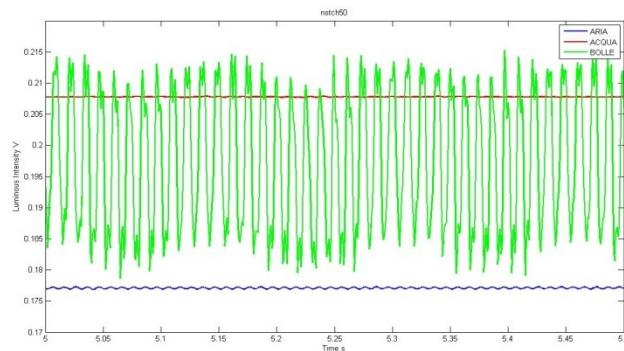

Figure. 3.38 Microfluidic Time series signal

Microchannel3 - 320μm- The microchannel-*3* is geometrically similar, but in terms of diameter different from the channel-*2* previously analyzed. In the previous channel, it has with different frequencies; it was found a common behavior for flow rate greater than 1mL/min. In this channel, as well as in others of equal size, it is still preferred to analyze three different flow rates, but discarding the analysis to *7 Hz* (*2.26 ml /min* Water - *1.71ml /min* air).

Air Flow - In a manner similar to what has been done for channel *2,* but with the devices described at the beginning of the paragraph have been studied flows having the following flow rate:

- *Experiment1:*1,20 ml/min → *frequency* =5 Hz
- *Experiment 2:*0,12 ml/min → *frequency* =0,5 Hz
- *Experiment 3:*0,012 ml/min → *frequency* =0,05 Hz

Water Flow - With regard to the flow of air used in this channel are shown the following flow rate:

- *Experiment1:*1,57 ml/min → *frequency* =5 Hz
- *Experiment 2:*0,157 ml/min→ *frequency* =0,5 Hz
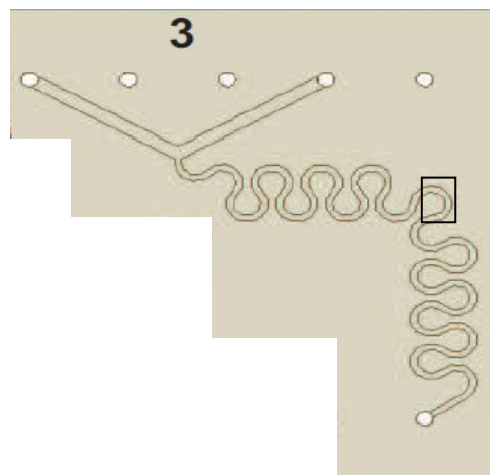- *Experiment 3:*0,0157 ml/min→*frequency* =0,05 Hz

Figure. 3.39. microchannel3-320µm

Bubble flow- The combination of the flow rates of air and water mentioned in the preceding paragraphs, the two-phase flow was monitored as a function of its speed.

In particular, trying to keep along the same line for the channel from *640μm*, the figure *3.40* shows the *FFT* for the experiment *3* and the signals of luminous intensity related to air, water and bubble. Natural mind for a better interpretation, are shown on the graph of the signals also the references of air and water at the given flow rate.
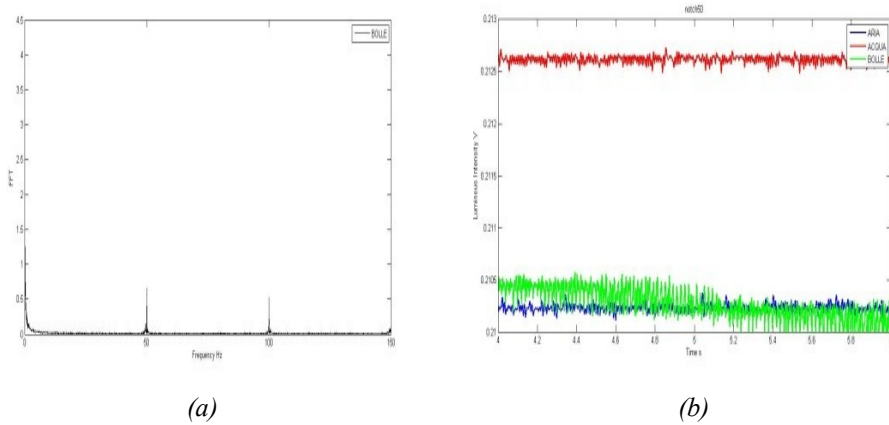

(a)   (b)

Figure. 3.40. Experiment-3 (a) FFT Signal (b) Time series signal

It is noted in a very obvious way as for a very low frequency of the order of *0.05Hz* in fact there is a flow of bubbles, in fact the signal oscillates as the flows of air and water (*FFT* equal to that of the signals of air and water).

Using the other two flow rates instead there has been a behavior similar to that found in channel-*2* in figure. *3.41*.
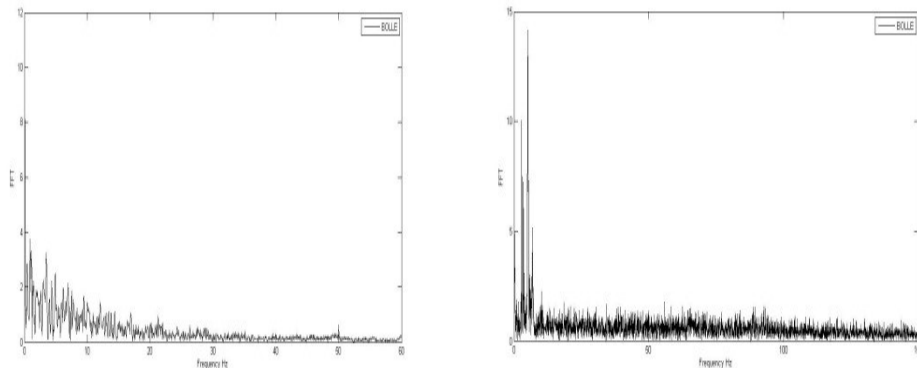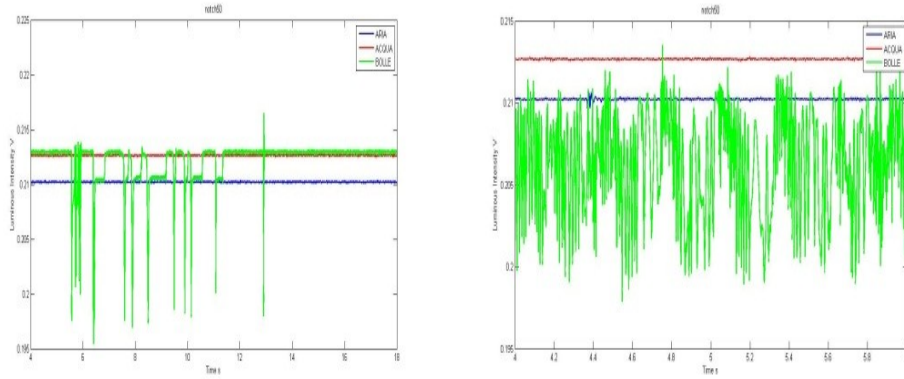
Figure. 3.41 – a left Experiment 2; a right Experiment 1

It is therefore found:

For *flow rate> 1ml/min* is a trend that, although not defined as in the larger channel, however, the light signals oscillates between the reference water to the air;

For *flow rate <1 ml/min* it has a pattern which does not characterize a continuous stream of bubbles, and this difference is significant in the *FFT*.

Microchannel4-320μm - As can be seen in figure *3.42* the channel *4* is once again geometrically a coil, even if in this case, unlike the previous it extends along a direction, linearly. The rectangle shows the area of channel monitored.
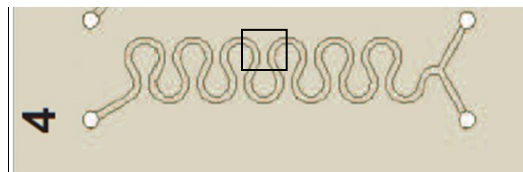

Figure. 3.42. Microchannel 4 of width/depth 320μm

Air Flow - In a manner similar to what has been done for channel 2, but with the devices described at the beginning of the paragraph have been studied flows having the following flow rate:

➢ *Experiment1:*1.20 ml/min →*frequency* =5 Hz.
➢ *Experiment 2:*0.12 ml/min →*frequency* =0.5Hz.
➢ *Experiment 3:*0.012ml/min →*frequency* =0.05Hz

Water Flow - With regard to the flow of air used in this channel are shown the following flow rate:

➢ ***Experiment1:***1,57 ml/min →*frequency* =5 Hz
➢ ***Experiment 2:***0,157 ml/min→*frequency* =0,5 Hz
➢ ***Experiment 3:***0,0157 ml/min→*frequency* =0,05 Hz

Bubble flow – Even in this case the experiments *1*, *2* and 3 were repeated to obtain a two-phase flow and then a stream of bubbles.

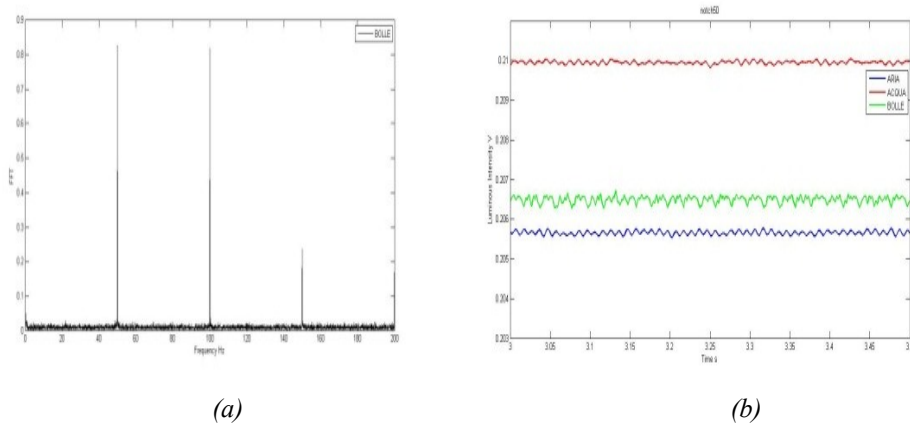(a)   (b)

Fig. 3.43 – Experiment3 (a) FFT signal (b) Time series signal

Once again it has been analyzed the discrete Fourier transformation of the signals from the photodiodes, and the variations in brightness in relation to the flow rate (experiment).

In figure *3.43*, it repeats the speech made for the previous cases, namely that a flow rate so low determines a flow that does not lead to the formation of bubbles, rather to a stream that is halfway between air and water. The *FFT* shall verify the trend, presenting the harmonic characteristics of the fluids of departure.

Below are instead the data obtained from experiments *1* and *2* in figure *3.44*. Here you can see the clear difference between the *FFT* compared with the previous experiment, as reflected inter alia in the signal intensity.

(a)   *(b)*
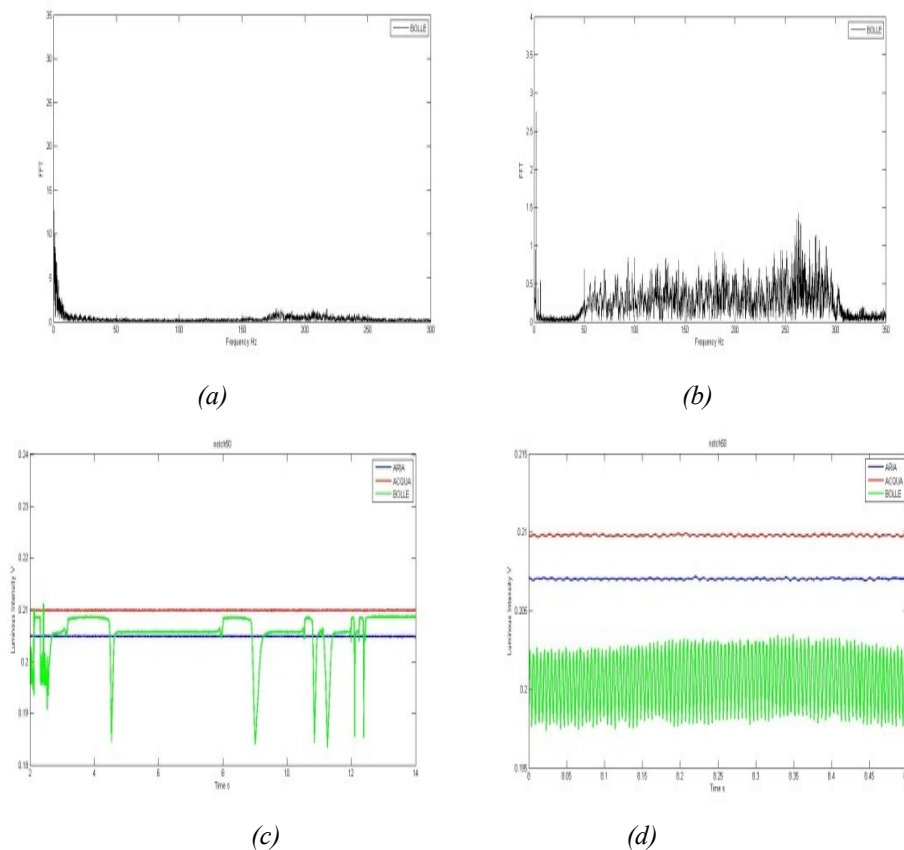
(c)   *(d)*

Fig. 3.44 Experiment-2 on the left and on the right Experiment-1 (a)-(c) FFT signal and (b)-(d) Time series signal

3.10 Y-junction Computational Modeling for Droplet Generation

The parametric computational modeling using T-junction has already been given in chapter 2 for various behaviors due to flow rates and the geometry. This context explains the parametric computational modeling of Y-junction for the droplet generator.

3.10.1 Parametric CM

The parametric computational modeling of Y-junction has been accomplished followed by proportion method applied using T-junction. The geometry has been subdivided into three parts as shown in figure 3.45 for the better performance. The two flow rate of continuous phase as water and disperse phase as hexadecane/air is pumped through D1 and D2. The computational setting for the software COMSOL 3.5a is explained in chapter 2.
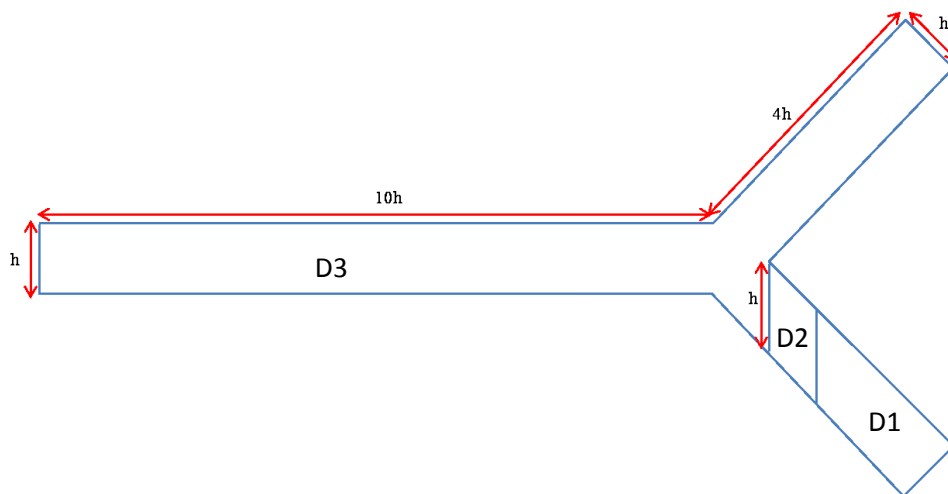

Figure. 3.45. Geometry of parametric computational model of Y-junction

There were three geometries have been executed as follow:

Geometry1- The parametric geometry is designed for width/depth *100x100μm*. The figure *3.46* shows the length of the bubble pattern is *100μm* obtained for the flow rate *0.05μL/s* and *0.1μL/s*.
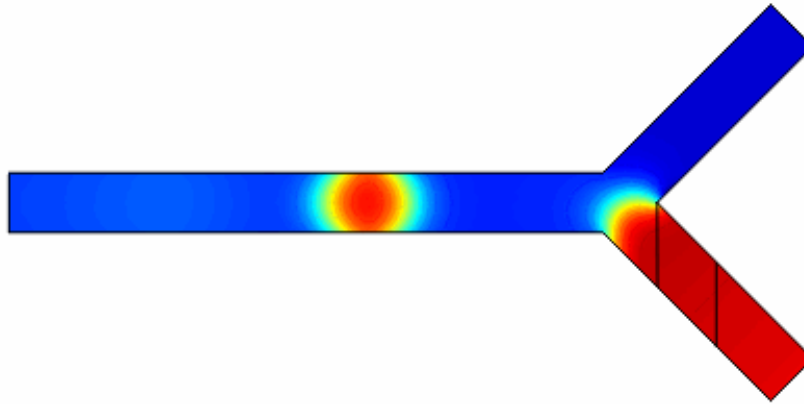

Figure. 3.46. Parametric computational geometry-1

Geometry2:   The parametric geometry has been designed for width/depth *50x50μm*. The bubble pattern shown in figure *3.47* is that the flow of disperse phase is greater than the flow rate of continuous phase. The length of the bubble obtained for the geometry is *200μm*.
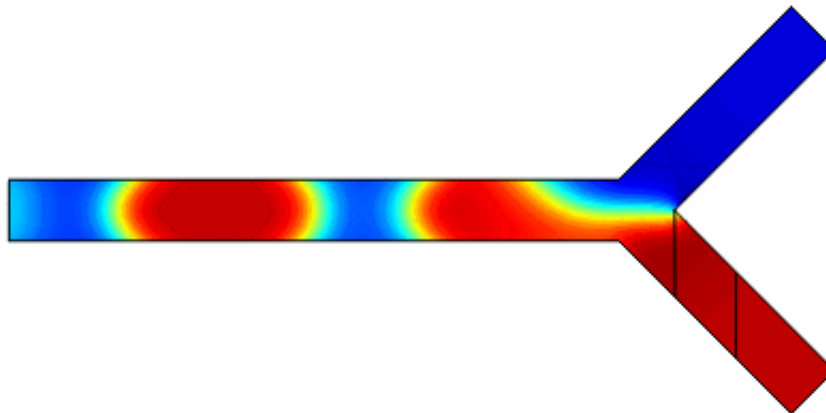
Geometry3: The parametric computational modeling of the geometry designed for width/height *640x640μm* has been realized using the same flow rate given in geometry1. The length of the bubble pattern obtained for this geometry is *1mm*.
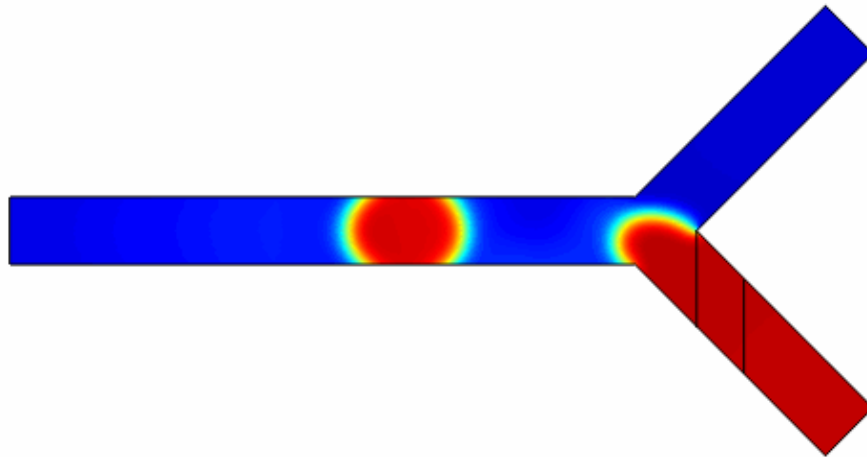
Figure. 3.48. Parametric computational geometry-3

3.11   Flow Pattern through CMs of Microfluidic Chip

Let see the computational model of microfluidic chip channels for two different measurements *320μm* and *640μm*. The given flow rate for microfluidic chip geometry is 1.6μL/s and also the two phase fluid as water and hexadecane because the simulation

3.11.1 Straight Channel (320μm)

The computational modeling of straight channel geometry is experienced as shown in figure *3.49* for the given flow rate. The bubble flow acquired shown in figure is periodic, but after some time the size of the bubble is loosens due to the length of the channel. The phase field graph is shown in figure 3.50.
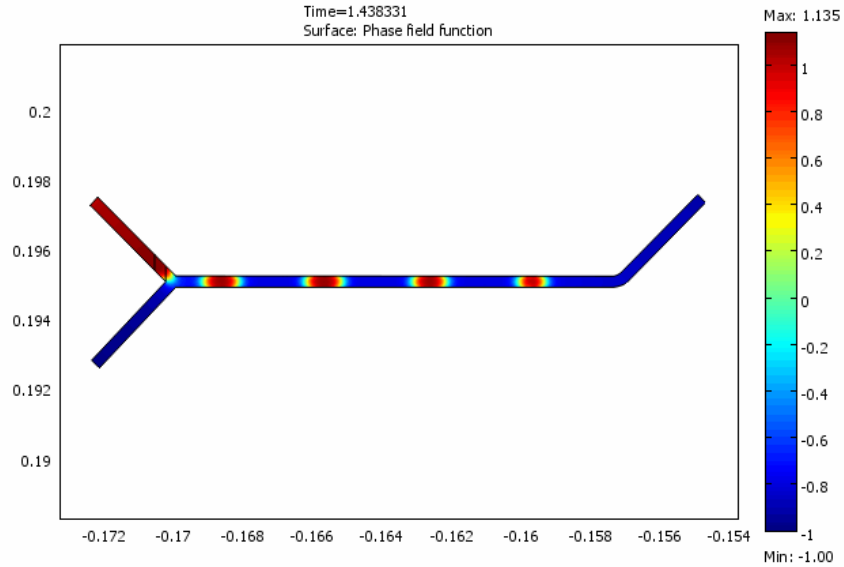
Figure. 3.49. Straight channel which has the width/depth 320µm
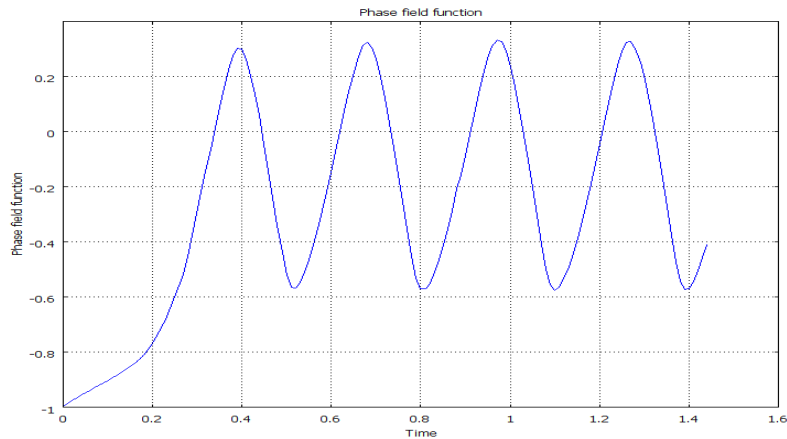
Figure. 3.50. Phase field function

3.11.2 Serpentine Channel (640µm)

The serpentine channel shown in the figure 3.51 has designed for width/depth *640µm*, actually the geometry of the serpentine channel is shown in figure *3.35* but it was very difficult to compute due to the complex serpentine geometry. As the figure shows the bubble reaches at some point and

loosens the size. The phase field function is shown in figure 3.51 shown periodic responses.
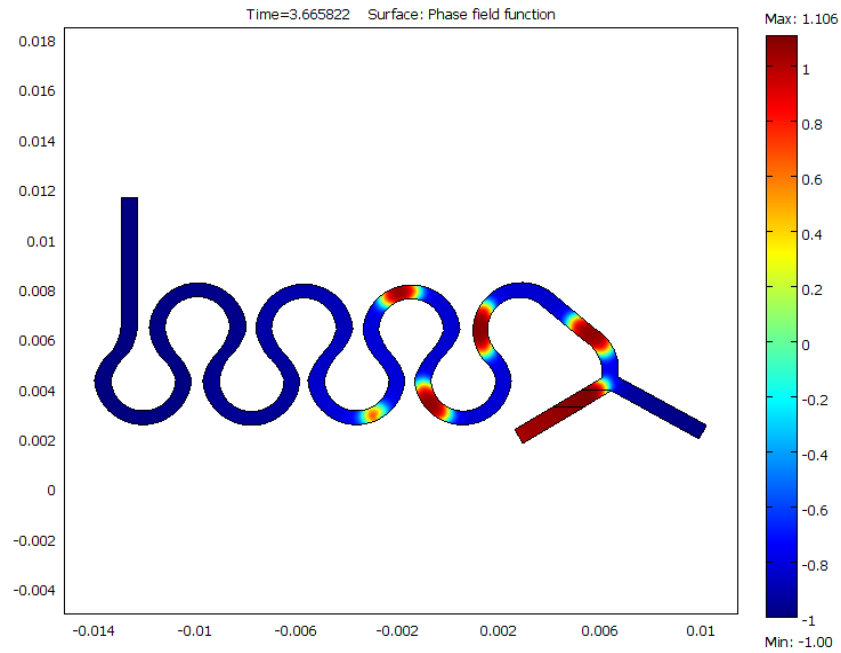
Figure. 3.51. Simulation result of Serpentine channel 640μm
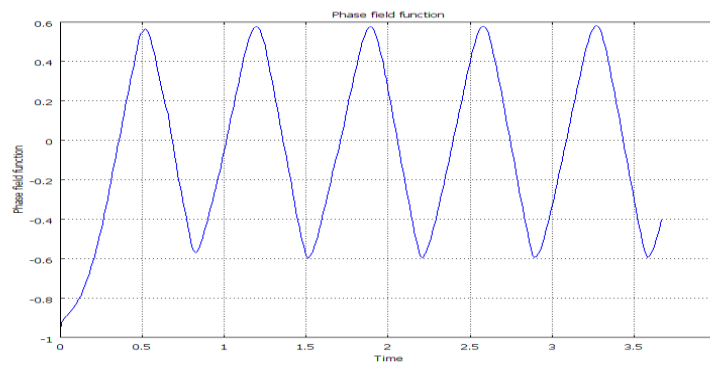
Figure. 3.51. Phase field function

The comparison of Experimental analysis and Computational analysis of microfluidic chip channels become very tricky, because the microfluidic chip channel has complex geometries which have high non-linearity, so when it comes to computational modeling the simulation stops at some point. It is also complicated to compare with the simulation and experimental results. For example see figure 3.52 serpentine channel simulation which has width/height 320μm stops before the disperse phase liquid filament break to form bubble.
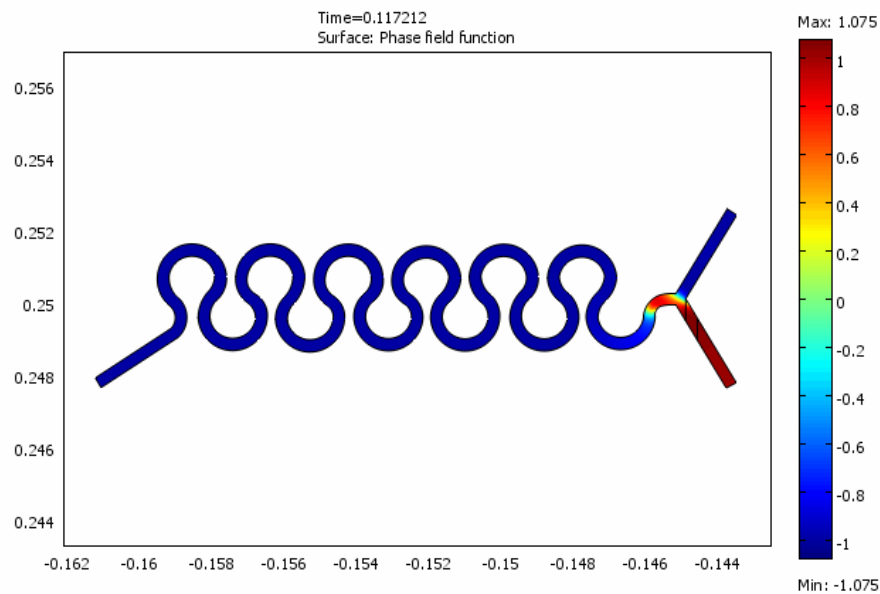
Figure. 3.52. Serpentine channel 320μm

The study, part of micro optofluidic, provides a starting point un-deniably linked to the really interesting disciplines such applications can achieve. The analysis that carried out have allowed to define in some detail the integrated system used to thorlabs has made available just for experimentation in the field micro optofluidic. In particular, the characterization of the detection devices used in

experimental tests provides an important reference if not essential in order to face future studies of two-phase flow and beyond.

In additions, it carried out the analysis in the various microchannels fixed distinctive features in terms of flow rate - for each dimension of it laid the foundations for the construction of a viable model usable for future analysis, and other microfluidic devices. Fundamental is finally the study and design of a system embedded in micro optofluidics optical Lab-On-Chip (*LOC*), to realize that allows very narrow spaces in a microfluidic system, guaranteeing a certain portability, That It Integrates optical functions

Thus achieving the right balance between the two disciplines, played as part of a global project in which design and manufacture of micro-devices *LOC*, studies and experiments within micro optofluidic could easily fit in a biochemical analysis of the microscopic scales of biological particles of various kinds.

Chapter-4

The dynamical model identification of the asymptotic Time signals belonging to a microfluidic two-phase flow Process is presented. The experimental time series are used to synchronize another system with known mathematical model but unknown parameters: the Chua's oscillator. This system has been chosen for its simple mathematical structure and for the Possibility, respect to other chaotic systems, of mapping various non-linear experimental phenomena. A genetic algorithm was Exploited for parameters estimation in relation to an optimization Index that takes into account the synchronization of master (microfluidic system) and slave system (Chua's oscillator).

Data driven Identification of Bubble Flow in Micro Channel

4.1   Data Driven Identification

In this context new trends in the generation and manipulation of micro droplets, known as digital or droplet microfluidics, have used passive strategies, related to well-chosen channel design to simplify the related control issues [6]. Microfluidic chips can act as logic gates explained in the second chapter, so that the control systems become part of the microfluidic process achieving the integration between chemistry and computation [6].

The main drawback in microfluidics is that the increasing complexity of the chain of processes brings the necessity of a precise knowledge of bubble/droplet dynamics in the microchannel network. Previous works focused on the determination of the hydrodynamic resistance of individual droplets to determine their global behavior [34]. Labrot et al. obtained a range of validity for a simplified theoretical model based on Kirchhoff laws. The main assumption in this work is that the bubbles have no dynamical interaction among each other and also a constant velocity.

In another study, the analog electrical model of the droplets' dynamics is based on Van Der Pol oscillator that tries to model the dynamical regime of microfluidic droplets [43]. In this complex scenario in which the properties of both buffer and dispersed fluid, input flow conditions, channel geometry etc. affect the dynamics of droplets it is necessary a general approach for the identification of the two-phase flow dynamics. The model that will be identified represents the emerging dynamics of a collective motion of a train

of bubbles in a snake microchannel, and it does not assume any hypothesis on the process. Instead it has been introduced a general approach in which the simplification is not related to the two-phase model itself but on the monitoring system and on the information acquired from experimental measurements.

A necessary effort instead is to find class nonlinear drive decomposable dynamical models, i.e. divisible into two subsystems, which can describe the bubble dynamics. Thus the main advantage of this methodology is the possibility of a fast identification of the model using experimental time series. Generally microfluidics processes can be monitored acquiring the light intensity variations through the channel section. Image or signal processing techniques allow the reconstruction of time series carrying information on the dynamics of droplets/bubbles.

The possibility to distinguish different flow regimes in two-phase microfluidic flows through time series analysis has been recently discussed in literature, and particularly it has been proved the capability to reach a classification of their nonlinear behaviors [40]. A set of 16 experiments were conducted. Air and water were flushed at constant flow rate at the inlets of the Y-junction of a snake microchannel and a train of very close bubbles was generated by tangential stress. The experimental measures on bubble flow are extracted by a photodiode-based acquisition system. The time series obtained, that are related to the average light intensity in a specific micro-channel area, were post processed and used for the successive identification step.

A classical problem of system engineering is the identification of known model starting from measured data. The experimental data represent the asymptotic time evolution of the state variable of a nonlinear system whose model is known but the parameters have to be estimated. On this purpose, one of the approaches proposed in literature is based on the concept of the synchronization in nonlinear science, which studies the adjustment of rhythms of oscillating objects due to their weak interaction. Synchronization of chaotic systems, i.e. the regime in which two or more chaotic oscillators evolve following the same chaotic trajectory despite their different initial conditions, is a very interesting feature studied under many points of view from secure communication systems to the transmission of digital signals [31]. Many schemes for achieving synchronization of coupled chaotic units are discussed in literature, in particular are relevant the seminal paper by Pecora and Carroll [37], and Boccaletti [20].

Synchronization schemes are classified in two main classes: unidirectional or bidirectional coupling. In the former case, the global system is subdivided into two parts, a master, whose dynamics remains unchanged, and a slave, that will be forced to follow the master dynamics. In the latter case, both master and slave system are affected by the coupling effects toward a common behavior that is often different from their original dynamics. Here an approach based on unidirectional synchronization is used for the identification of two-phase microfluidic processes. The experimental time series are assumed as the asymptotic behavior of a generic state variable of an unknown master system.

This information was used to drive a slave system, with a known model and undefined parameters. The nonlinear model used as slave system is the Chua's oscillator. To reach the synchronization, an identified set of parameters in Chua's model is able to reproduce the main dynamics of the bubble flows. The Chua's oscillator has been selected, among other nonlinear systems, for the variety of dynamical behaviors that can be obtained changing its parameters. In order to achieve synchronization by the identification of suitable values of the Chua's parameters, an iterative procedure based on Genetic Algorithm (*GA*) was implemented and a *L2-* norm was introduced to define and optimization index.

Different classes of synchronization can be distinguished in literature, particularly the presented results have shown that it is possible to reach a lag and phase locking synchronization for each experiment. Particularly, the phase locking synchronization (*PS*) occurs in oscillators when their frequencies and phases are locked, while amplitudes remain almost uncorrelated. In our case the important information is not strictly related to the signals amplitude but to the frequencies and the phase of the signals that are representative of the collective motion of bubbles in the micro device.

In section *2* a brief introduction on the physics of microfluidic two-phase systems and the main dimensionless parameters involved are presented. In section*3* the experimental setup and the acquired data are described and characterized by means of time series analysis. Finally section *4* and section *5* deal

with the adopted identification approach and the obtained results are discussed.

4.2   *Physical Background*

The evolution of two-phase flow is classically described using the one-fluid formulation of the Navier-Stokes equation in the chapter-*1*. An important dimensionless parameter in microfluidics is the Reynolds number defined represents an indicator of flow nonlinearity [1]. The Reynolds number at the transition between laminar and turbulent flow is of the order *103*, but is depends on channel geometry and type of the flow.

On the other hand considering the role of the input flows in the two-phase flow generation, two dimensionless numbers have been widely investigated in microfluidics for their influence in the control of mixing rate inside droplets [23] and in the characterization of flow patterns regime [24]. The Capillary Number *(Ca)* and the Sample Fraction (here indicated as Air Fraction because air is used as the dispersed phase).
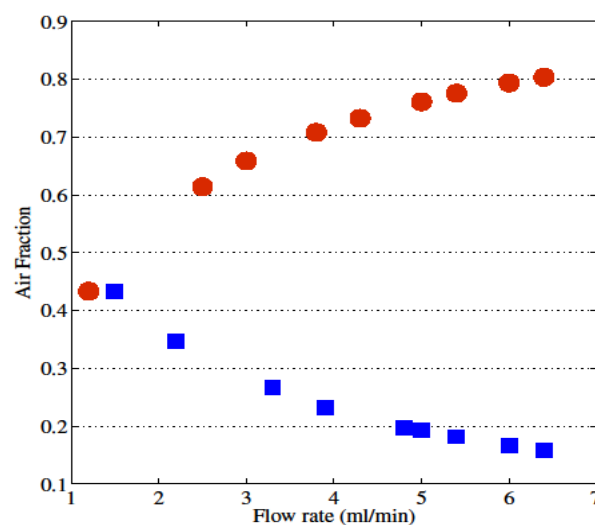

Figure. 4.1. Air Fraction versus flow rate for the two set of experiments. A red circle represents the AF for V_{water} fixed while blue squares V_{air} fixed.

In particular being the microfluidic process largely dominated by the interfacial effects Capillary Number *(Ca)* enhances the relative importance of viscous to surface tension force meanwhile the Air Fraction *(AF)* highlights the fraction of the sample flow that is flushed in the micro-channel. These two parameters are evaluated as follows [36]: The range of considered flow rates see table 4.1 leads to a unique range of Ca number *(0.01, 0.02)* and two separate ranges of AF as shown in Figure. *4.1.*

4.3   *Experimental Setup and Time Series Analysis*

Bubbles carried by de-ionized water were generated by tangential stress at the Y-junction of a snake microchannel made in *COC* (*Cyclic Olefin Copolymer*). It has a depth of S=640μm and internal radius of curvature of *R=1.28 mm* (*SMS0104, Thinxxs*).

EXP. 1-8	V_{water}=1.5 ml/min V_{air}=1.2 ml/min-V_{air}=2.5 ml/min-3 ml/min-3.8 ml/min-4.3 ml/min-5 ml/min-5.4 ml/min-6 ml/min-6.4 ml/min
EXP. 9-16	V_{air}=1.2 ml/min V_{water}=1.5 ml/min-V_{water}=2.2 ml/min-3.3 ml/min-3.9 ml/min-4.8 ml/min-5 ml/min-5.4 ml/min- 6 ml/min-6.4 ml/min

Table 4.1. Input flow rate for air and water

Constant flow rates for air and de-ionized water were imposed at channel's inlets by means of syringe pumps (Cetoni, Nemesys). The micrometric size of microfluidic systems require optical instrumentation for image magnification so in this work an ad hoc electro-optical system with 20x magnification objective was used.
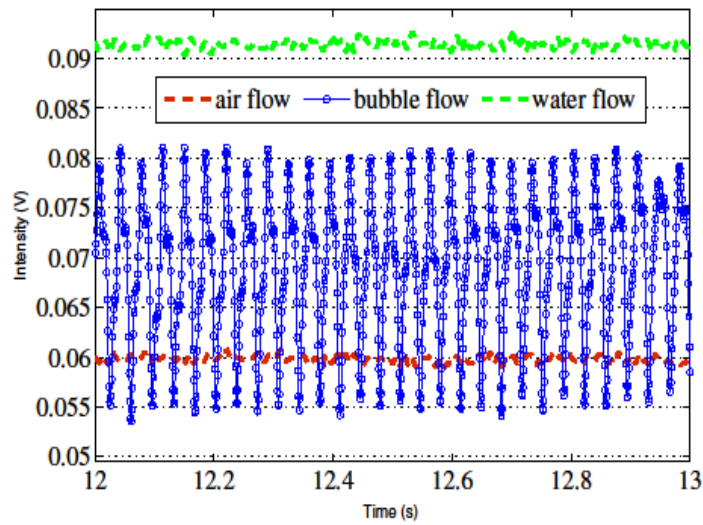
Figure. 4.2. Bubble flow signal (V_{air}=1.2 ml/min, V_{water}=1.57 ml/min) and reference flow of water (green bold line) and air (red bold line).

This optical system allowed a parallel acquisition of the light intensity variation in a well defined area of the microchannel of 640μm x 935μm through a *CCD* (*DCU224, Thorlabs, 30 fps*) and a photodiode based circuit (*SLD-70BG2, Silonex*).

Figure. 4.3. Fast Fourier transform for three different signals of bubble flows.

A *DAQ* converts the signals into time-series with sample rate of *1 kHz*. A scheme of the setup for the acquisition system is shown in figure *4.4*. The light intensity time series is fully

representative of the bubble flow (as named in the following) as highlighted in the time series shown in Figure. 2 where the signal representative of a bubble flow (blue line) oscillate betw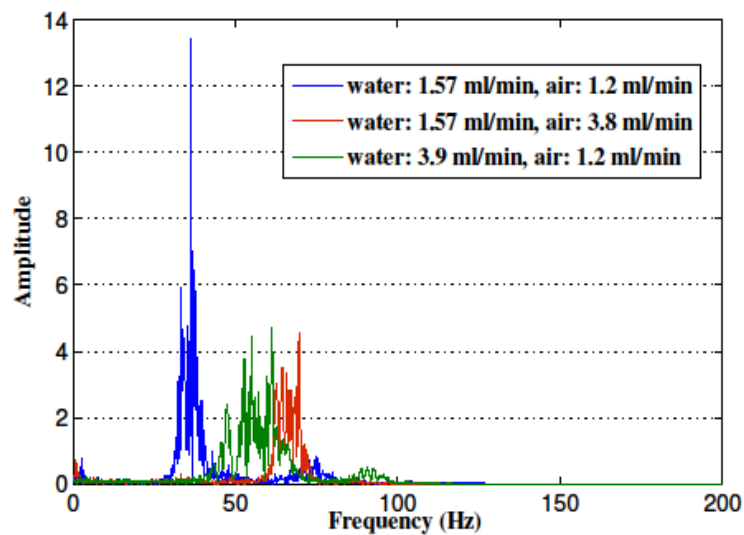een two reference signals of air (red line) and water (green line). The oscillating dynamics of the signal is related to the bubbles passage in the specific location of the acquisition area. We performed two sets of experiments.
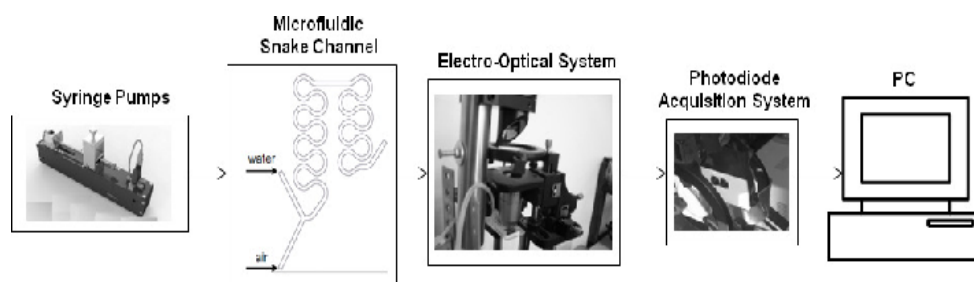
Figure. 4.4. Complete setup for the acquisition of Microfluidic time series.

In the first one the air flow rate Vair has been fixed at *1.2 ml/min* while the water flow rate Vwater has been increased progressively from *2.26ml/min* up to *6.4ml/min* and vice versa considering Vwater fixed at *1.57ml/min*, Vair has been increased progressively from *2.5ml/min* up to *6.4ml/min*, leading to a total of *16* experiments. Each bubble flow has been recorded for a time window of *20* seconds. The details of the input flow rates for the experiments are shown in table *4.1*. All the time series were filtered with a low pass filter ($f_{cut}=100$ *Hz*) and two Notch filter ($f_{cut}=50$-*100 Hz*) to avoid unwanted components due to environmental light and electric noise.

As shown in figureure.*4.3* when we tune the input flow rate the Fourier transform of the signals shows a broad band in which the central frequency increases as the input flow rate increases. Starting from this experimental evidence we can assume that the

main information on the system is contained in frequency of the signals.

4.3.1 *Nonlinear indicators*

In previous works [40] it has been widely proved the nonlinearity of the dynamics of the bubble flow and the possibility for their classification through nonlinear indicators [32]. Nonlinear time series analysis were applied to the experimental time series in order to quantify the flow patterns and the bubbles' dynamics in terms of Largest Lyapunov exponent (*LE*) [19] and d_∞ [22]. Lyapunov exponents are fully representative of the sensitivity to initial conditions (stretching phase) of a given nonlinear dynamical system, being positive for chaotic behaviors [41].

(a)   (b)
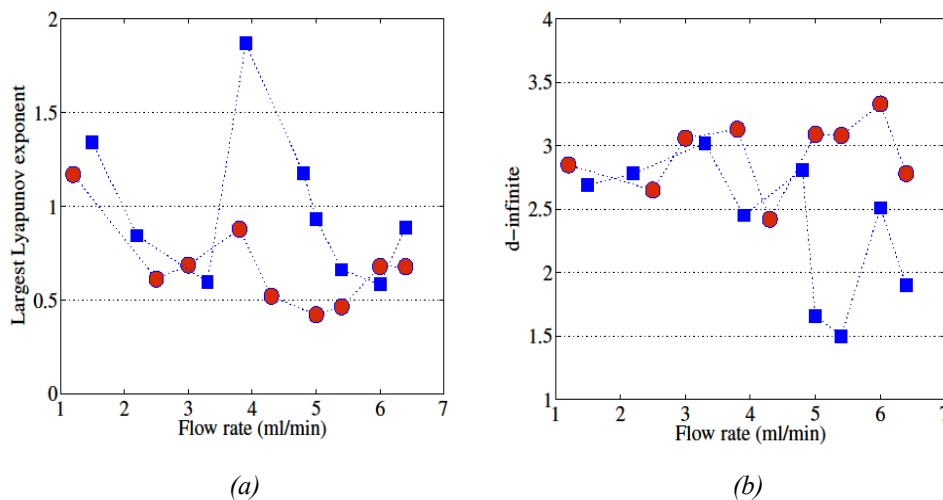
Figure. 4.5. (a) Largest Lyapunov exponent and (b) d-infinite calculated from the time series of the bubble flow for V_{air} fixed (squares) and V_{water} fixed (circles).

Often it is sufficient to establish the existence of at least one positive Lyapunov exponent to define chaotic dynamics [42]. Thus the Largest Lyapunov exponent quantify a degree of nonlinearity while the d_∞ is sensible of both stretching and folding mechanism so it is not only a complementary measure to maximal Lyapunov

exponent but also a robust parameter for time series corrupted by noise. The relationship between Largest Lyapunov exponent λ and the divergence of the jth pair of trajectories started from nearest initial condition can be represented by the following relation [43]:

$$d_j(i) \approx C_j e^{\lambda(i\Delta t)} \tag{4.7}$$

where λ is the largest Lyapunov exponent and C_j is the initial separation between the trajectories, i is the discrete time step and Δt the sampling period of the time series. Equation is valid for a finite number of time-step after that the diverging curve saturates since the effects of *folding* process take place keeping all the trajectories bounded. Thus taking into account the evolution of the first order expansion of $d_j(i)$ and adding a second order term representative of the folding process, the asymptotic value d_∞ is defined as the non null fixed point of the following equation [22]:

$$d(i+1) \approx \Lambda d(i) - \Gamma d^2(i) \tag{4.8}$$

where Λ and Γ represent respectively e^λ and the coefficient of the second order correction term related to folding effect. The Largest Lyapunov exponent is estimated through the finite size Lyapunov exponent method [19]:

$$\lambda(\delta, \Delta) = \langle \frac{1}{T(\delta,\Delta)} \rangle \ln\left(\frac{\delta}{\Delta}\right) \tag{4.9}$$

where δ is the initial error and Δ our tolerance, while T is the predictability time. The d_∞ has been calculated from the asymptotic value of the logarithm of the stretching factor d_j [43]:

$$\sum_{i=N}^{M} \langle ln\left(d_j\left(i\right)\right)\rangle \qquad (4.10)$$

with *N=600 (t$_N$=0.6)* and *M=800* (for a total of *800* iterations, in time *t$_M$=0.8*). It is worth to notice that the d_∞ obtained values are bounded in the range *(0, 1)* and in the following is considered the absolute value of its logarithm *(|log(d$_\infty$)|=d-infinite*) so the lower value, the higher the nonlinearity (and vice versa). All the nonlinear parameters have been calculated by means of the software *TISEAN* [30].

Moreover the state space reconstruction was performed by the method of delays giving a visual characterization of the microfluidic dynamics looking at the attractor geometries associated to the former nonlinear measures (Lyapunov exponents and d_∞) [32]. In figure *4.5(a)* and 4.*5(b)* the dynamics of the Largest Lyapunov exponents and d-infinite versus flow rate for each experiment are reported.

4.4 Two-Phase Flow Modeling

When we deal with chaotic systems, synchronization is nontrivial. One of the property of chaotic systems is the sensitivity to initial conditions, thus two identical systems starting from slightly different points in the state space evolves, in long-term, in a totally uncorrelated manner. Therefore, synchronization of chaotic systems is a relevant problem, being the initial conditions not exactly known in experimental setups. The interest rises when

the synchronization theory is used as a framework for the modeling and identification of real-world process by means of experimental data.

In this case it is useful to use a unidirectional synchronization scheme that considers only how one system, the master, can affect a second system, and slave. Following this schema it can be estimated a set of parameters of a known model to reach the synchronization between the asymptotic time evolution of at least one state variable of the model and the experimental data extracted from a physical process [37].

4.4.1 Synchronization of chaotic systems

Considering the definition of master-slave synchronization first introduced by Pecora and Carroll [20], in third order systems (*x,y,z*) it can be assert that the master is synchronized with the slave if for all the choices of initial states the following limits hold (28):

$$lim_{t \to \infty} |x(t) - \tilde{x}(t)| = 0$$
$$lim_{t \to \infty} |y(t) - \tilde{y}(t)| = 0 \qquad (4.11)$$
$$lim_{t \to \infty} |z(t) - \tilde{z}(t)| = 0$$

where *x, y, z* and $\tilde{x}, \tilde{y}, \tilde{z}$ are the state variable of respectively the slave and the master system considered. In this representation the slave system can be decomposed at least into two subsystems: a drive system and a stable response subsystem (method of decomposition into sub-systems) such that we can force the slave system to follow desiderate state variable (driven variable). It has been demonstrated that with this procedure the systems synchronize also in presence of noise [20].
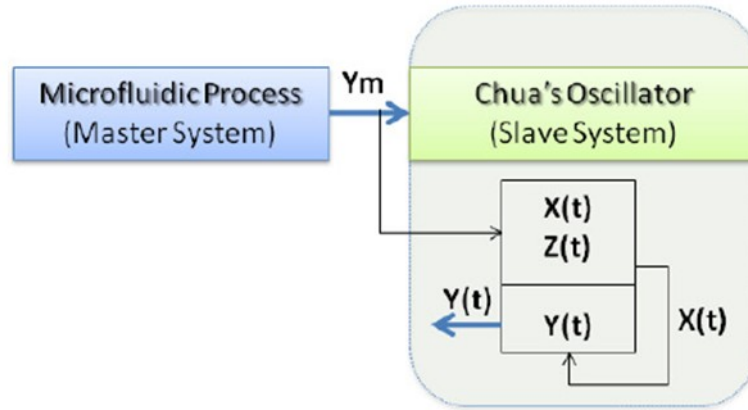
Figure. 4.6. Schematic representation of master-slave synchronization in which the microfluidic time series works as the master system.

It is possible to distinguish four main classes of synchronized behavior: Complete (or identical) synchronization (CS) consists in a perfect matching of the two (or more) chaotic trajectories, in this sense the systems forget their initial conditions continuing to evolve chaotically; phase synchronization (PS) occurs in oscillators when their phases are locked, while amplitudes remain almost uncorrelated; lag synchronization (LS) is somehow between PS and CS [38] and occurs when the two trajectories are locked both in phase and amplitude but with a finite time lag; generalized synchronization (GS) is achieved when the dynamics of one of the coupled systems can be expressed as a function of the other dynamics. Transitions through the four synchronizations have been observed with respect to the strength of the coupling [39]. Synchronization of chaotic systems is often studied for schemes of the form of (29):

$$M : \dot{x} = f(x) + M(x - \tilde{y})$$

(4.12)

$$S : \dot{\tilde{y}} = g(\tilde{y}) + N(x - \tilde{y})$$

with $f(\cdot):\Re^n{\rightarrow}\Re^n, g(.):\Re^n{\rightarrow}\Re^n$, state vectors x, $\tilde{y}\epsilon\Re^n$ and coupling matrices M, $N \epsilon \Re^{nxn}$. The unidirectional synchronization setup (*M=0*) used in this work is shown in Figure. 6.

It is worth to notice that here the master system is the experimental microfluidic time series (a single state variable) and the slave system is the Chua's model. The last one has been decomposed into two subsystems corresponding respectively to the state variable *y* and the state variables *x* and *z*.

4.4.2 The Chua's oscillator

The Chua's oscillator has been chosen for the wide range of behavior that can arise changing its parameters. One important advantage of the Chua's oscillator over other nonlinear systems is that it is the only known physical system whose mathematical model is capable of duplicating almost all experimentally observed phenomena [33].

The state equations of Chua's system are topologically conjugate to a *21*-parameter family of continuous odd-symmetric piecewise-linear equation in *R3*, so virtually every known third-order odd symmetric chaotic autonomous system with 3 equilibrium points can be modeled by a Chua's oscillator [33].

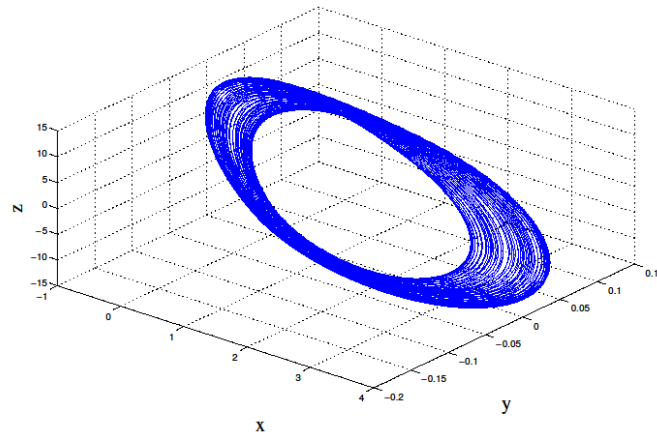The dimensionless state equations of the Chua's oscillator are:

Figure. 4.7. Reconstructed attractor of the Chua's oscillator for α=1800, β=10000, γ=0, m0=-1.026, and m1=-0.982.

$$\frac{dx}{d\tau} = k\alpha\big(y - x - f(x)\big)$$

$$\frac{dy}{d\tau} = k(x - y + z) \qquad\qquad (4.13)$$

$$\frac{dz}{d\tau} = k(-\beta y - \gamma z),$$

$$f(x) = m_1 + \frac{1}{2}(m_0 - m_1)\{|x + 1| - |x - 1|\}$$

where *x,y,z*, and *z* are the state variables and α, β, γ, m_0 and m_1 the parameters. In Figure. 4.7 is represented the reconstructed attractor of the Chua's oscillator for the selected parameters *α=1800, β=10000, γ=0, m₀=-1.026*, and *m₁=-0.982*. This set of parameters lead to the toroidal structure attractor typical of the bubble flow dynamics for the considered input volumetric flows [40].

4.5   *Genetic Algorithm Optimization Technique*

The time series of the microfluidic process are used as master driving signal for the synchronization with the Chua's oscillator using the sub-system technique explained before. The

time series are normalized obtaining signals of zero mean and unity in variance. Moreover each time series has been divided into three sets each one lasting *5* seconds and for those time series the identification procedure has been applied. In particular, the parameters m_0 m_1 are kept fixed while *α, β* and *γ* are set respectively in the range (*1700, 2000*), (*9500, 10000*), (*0, 1*).

Also the time step t_s were imposed in the range (*0.001, 0.007*) in order to find via the genetic algorithm the correct time scale. The response sub-system (Chua's system) is solved by using a Dormand-Prince method [9] with fixed time-step. The optimization method used is based on genetic algorithms (*GA*) in a standard form [28].

Genetic Algorithm (GA) - It is an efficient and versatile instrumentation for global optimization of a function and furthermore is applicable in different fields [28]. Genetic Algorithms (*GA*s) are adaptive heuristic search algorithm premised on the evolutionary ideas of natural selection and genetic. The basic concept of *GA*s is designed to simulate processes in natural system necessary for evolution, specifically those that follow the principles first laid down by Charles Darwin of survival of the fittest. As such they represent an intelligent exploitation of a random search within a defined search space to solve a problem.

First pioneered by John Holland in the *60*'s, Genetic Algorithms has been widely studied, experimented and applied in many fields in engineering worlds. Not only does *GA*s provide an alternative method to solving problem, it consistently outperforms other traditional methods in most of the problems link. Many of the real

world problems involved finding optimal parameters, which might prove difficult for traditional methods but ideal for *GA*s. However, because of its outstanding performance in optimization, *GA*s has been wrongly regarded as a function optimiser. In fact, there are many ways to view genetic algorithms. Perhaps most users come to *GA*s looking for a problem solver, but this is a restrictive view.

Herein, *GA*s as a number of different things:

➢   *GA*s as problem solvers
➢   *GA*s as challenging technical puzzle
➢   *GA*s as basis for competent machine learning
➢   *GA*s as computational model of innovation and creativity
➢   *GA*s as computational model of other innovating systems
➢   *GA*s as guiding philosophy

However, due to various constraints, it has always been like a problem solvers and competent machine learning here. Many scientists have tried to create living programs. These programs do not merely simulate life but try to exhibit the behaviors and characteristics of real organisms in an attempt to exist as a form of life. Suggestions have been made that a life would eventually evolve into real life.

Such suggestion may sound absurd at the moment but certainly not implausible if technology continues to progress at present rates. Therefore it is worth, in our opinion, taking a paragraph out to discuss how a life is connected with *GA*s and see if such a prediction is farfetched and groundless.

*GA*s was introduced as a computational analogy of adaptive systems. They are modeled loosely on the principles of the evolution via natural selection, employing a population of individuals that undergo selection in the presence of variation-inducing operators such as mutation and recombination (*crossover*).

A fitness function is used to evaluate individuals, and reproductive success varies with fitness. The Algorithms:

➢   Randomly generate an initial population *M(0)*

➢   Compute and save the fitness *u(m)* for each individual *m* in the current population *M(t)*

➢   Define selection probabilities *p(m)* for each individual m in *M(t)* so that *p(m)* is proportional to *u(m)*

➢   Generate *M(t+1)* by probabilistically selecting individuals from *M(t)* to produce offspring via genetic operators

➢   Repeat step *2* until satisfying solution is obtained.

➢   The paradigm of *GA*s described above is usually the one applied to solving most of the problems presented to *GA*s. Though it might not find the best solution. More often than not, it would come up with a partially optimal solution.

Nearly everyone can gain benefits from Genetic Algorithms, once encode solutions of a given problem to chromosomes in *GA*, and compare the relative performance (fitness) of solutions. An effective *GA* representation and meaningful fitness evaluation are the keys of the success in *GA* applications. The appeal of *GA*s comes from their simplicity and elegance as robust search algorithms as well as from their power to discover good solutions

rapidly for difficult high-dimensional problems. *GA*s is useful and efficient when:

➢ The search space is large, complex or poorly understood.

➢ Domain knowledge is scarce or expert knowledge is difficult to encode to narrow the search space.

➢ No mathematical analysis is available.

➢ Traditional search methods fail.

The advantage of the *GA* approach is the ease with which it can handle arbitrary kinds of constraints and objectives; all such things can be handled as weighted components of the fitness function, making it easy to adapt the *GA* scheduler to the particular requirements of a very wide range of possible overall objectives.

*GA*s has been used for problem-solving and for modeling. *GA*s is applied to many scientific, engineering problems, in business and entertainment, including:

Optimization: *GA*s have been used in a wide variety of optimization tasks, including numerical optimization, and combinatorial optimization problems such as traveling salesman problem (*TSP*), circuit design [Louis 1993] , job shop scheduling [Goldstein 1991] and video & sound quality optimization.

Automatic Programming: *GA*s has been used to evolve computer programs for specific tasks, and to design other computational structures, for example, cellular automata and sorting networks.

Machine and robot learning: *GA*s has been used for many machine- learning applications, including classification and prediction, and protein structure prediction. *GA*s have also been used to design neural networks, to evolve rules for learning classifier systems or symbolic production systems, and to design and control robots.

Economic models: *GA*s has been used to model processes of innovation, the development of bidding strategies, and the emergence of economic markets.

Immune system models: *GA*s has been used to model various aspects of the natural immune system, including somatic mutation during an individual's lifetime and the discovery of multi-gene families during evolutionary time.

Ecological models: *GA*s has been used to model ecological phenomena such as biological arms races, host-parasite co-evolutions, symbiosis and resource flow in ecologies.

Population genetics models: *GA*s has been used to study questions in population genetics, such as "under what conditions will a gene for recombination be evolutionarily viable?"

Interactions between evolution and learning: *GA*s has been used to study how individual learning and species evolution affect one another. Models of social systems: *GA*s has been used to study evolutionary aspects of social systems, such as the evolution of cooperation [Chughtai 1995], the evolution of communication, and trail-following behaviour in ants.

The *TSP* is interesting not only from a theoretical point of view, many practical applications can be modeled as a travelling salesman problem (*TSP*) or as variants of it, for example, pen movement of a plotter, drilling of printed circuit boards (*PCB*), real-world routing of school buses, airlines, delivery trucks and postal carriers. Researchers have tracked *TSP*s to study bimolecular pathways, to route a computer networks' parallel processing, to advance cryptography, to determine the order of thousands of exposures needed in *X*-ray crystallography and to determine routes searching for forest fires (which is a multiple-salesman problem partitioned into single *TSP*s).

Therefore, there is a tremendous need for algorithms. In the last two decades an enormous progress has been made with respect to solving travelling salesman problems to optimality which, of course, is the ultimate goal of every researcher.

One of landmarks in the search for optimal solutions is a *3038*-city problem. This progress is only partly due to the increasing hardware power of computers. Above all, it was made possible by the development of mathematical theory and of efficient algorithms. Here, the *GA* approach is discussed.

There are strong relations between the constraints of the problem, the representation adopted and the genetic operators that can be used with it. The goal of traveling Salesman Problem (*TSP*) is to devise a travel plan (*a tour*) which minimizes the total distance travelled. *TSP* is *NP*-hard (*NP* stands for non-deterministic polynomial time).

It is generally believed cannot be solved (*exactly*) in time polynomial. The *TSP* is constrained:

➢ The salesman can only be in a city at any time.

➢ Cities have to be visited once and only once.

➢ When GAs applied to very large problems, they fail in two aspects:

➢ They scale rather poorly (in terms of time complexity) as the number of cities increases.

➢ The solution quality degrades rapidly.

The easy implementation of genetic algorithms makes them capable of optimizing also not convex functions. To drive the optimization procedure is fundamental to set the appropriate values for the *GA* parameters as reported in table *4.2*.

NIND	MAXG	GGAP	PREC
8	20	8	7

Table. 4.2. Parameters for the Genetic Algorithm

Moreover an optimization index, named fitness function, takes into account the error between the time series y_m of the microfluidic process and the y state variable of the Chua's oscillator, has been chosen as follows:

$$I(\alpha, \beta, \gamma) = \sqrt{\sum_{k=0}^{N}(y_m - y(\alpha, \beta, \gamma))^2} \qquad (4.14)$$

It is worth to notice that complete synchronization is not achieved for all the microfluidic time series. We encounter an alternation of phase synchronization (*PS*) and lag synchronization (*LS*).

4.6   Bubble Flow Non-Linear Models

The Fourier spectrum of the y state variable of Chua's system after the synchronization procedure has been compared with the respective spectrum of the experimental time series (see Figure. *4.8*) for four different couples of input flows: V_{water}=2.2 ml/min and V_{air}=1.2 ml/min, V_{water}=1.5 ml/min and V_{air}=1.7 ml/min, V_{water}=1.5 ml/min and V_{air}=2.5 ml/min, V_{water}=6.4 ml/min and V_{air}=1.2 ml/min. In Figure. *4.8* are indicated the fundamental frequency for each spectrum.
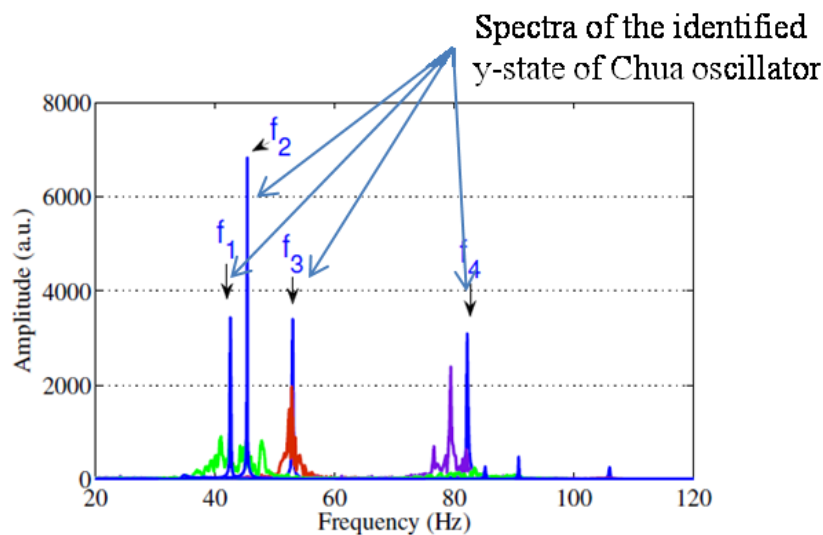

Figure.4.8. Spectra of the identified y-state of Chua oscillator (blue line) and experimental microfluidic time series for four different experiments: Vwater=2.2 ml/min and Vair=1.2 ml/min (green), Vwater=1.5 ml/min and Vair=1.7 ml/min (black, perfectly superimposed to the identified spectrum), Vwater=1.5 ml/min and Vair=2.5 ml/min (red), Vwater=6.4 ml/min and Vair=1.2 ml/min (violet).

These frequencies have values from f_1=43 Hz to f_1=85 Hz. It is worth to notice that with this identification procedure it is possible to capture the main component of the Fourier transform of the experimental time series but not the broad-band spectrum in the experimental time series. It has been demonstrated in a previous

work, through also surrogate analysis [40], that the broad band spectra are related to the non-linearity of the microfluidic process.
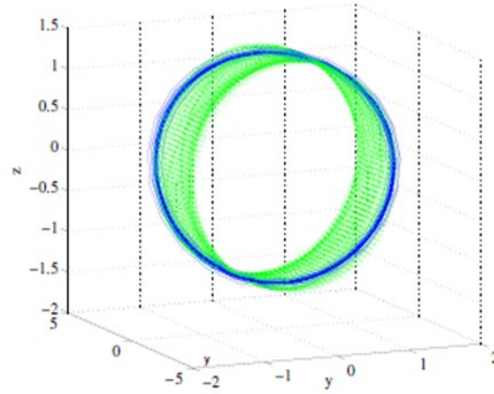

(a)
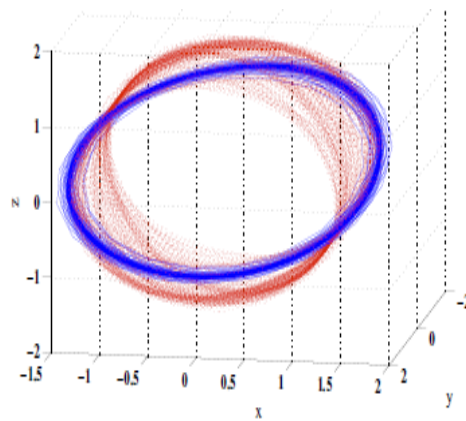
(b)

Figure. 4.9. State space reconstructions for time series for the y-state of the Chua system (blue line) and microfluidic signal obtained for (a) Vwater=2.2 ml/min and Vair=1.2 ml/min (green dashed line) and (b) Vwater=1.5 ml/min and Vair=2.5 ml/min (red dashed line).

The presented results are enforced looking at the phase space reconstructions in figure *4.10* for two selected experiments $V_{water}=1.5$ *ml/min* and $V_{air}=2.5$ *ml/min*, $V_{water}=1.5$ *ml/min* and $V_{air}=2.5$ *ml/min*. Both the attractors are not perfectly matched in amplitude and phase for the entire time window considered in the

analysis and their comparison shows and alternance of synchronization. Figure *4.10* shows the time series in different time windows for each experiment where there is an alternance of synchronization (lag synchronization) between the systems.
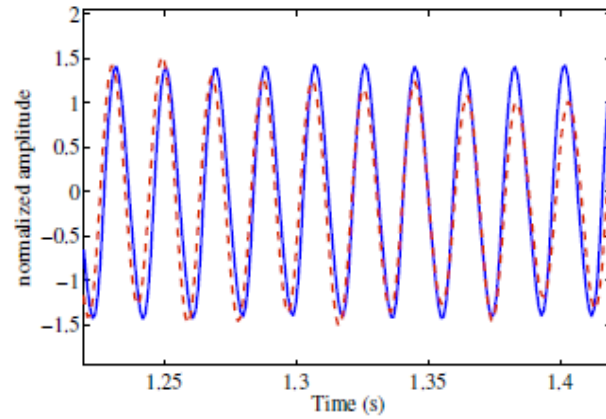
A global view of the variability of the obtained parameters after the optimization procedure in relation to flow rate changes is visible in figure *4.11(a)* for α parameter in figure *4.11(b)* for *β* and finally in figure *4.11(c)* for *γ* parameter.
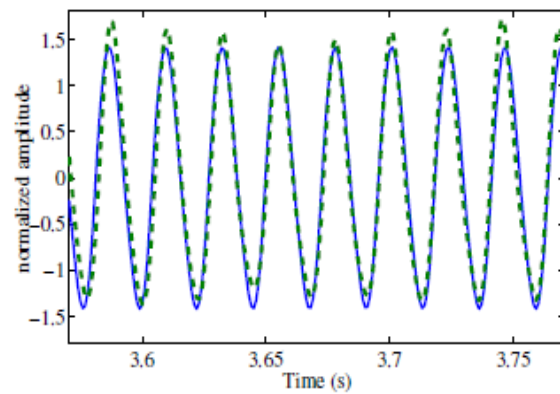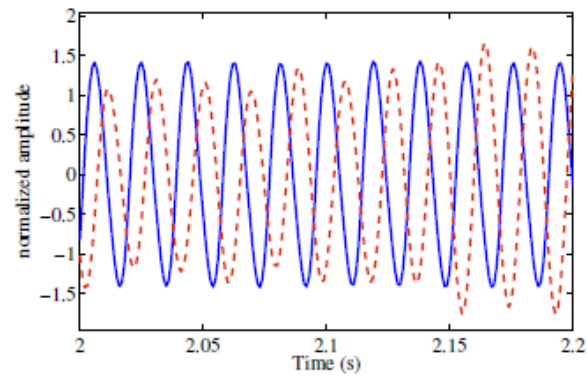

(a)
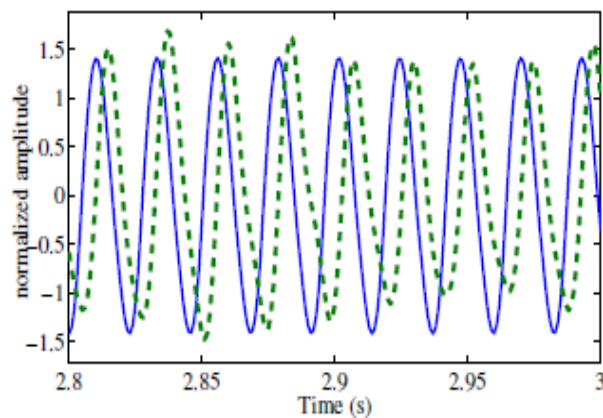
(b)

(c)

(d)

Figure. 4.10. Time series showing (a-c) synchronized and (b-d) and not synchronized regions for the identified Chua system (blue line) and microfluidic signal Vwater=1.2 ml/min and Vair=1.2 ml/min (green dashed line), microfluidic signal Vwater=1.5 ml/min and Vair=2.5 ml/min (red dashed line).

An error of the order of 10^{-2} is achieved for all the experiments. In this graphs we can notice how α parameter is able to distinguish the two experimental sets for flow rate lower that *5 ml/min*. Also it is worth to notice that the *β* parameter takes similar values in relation to the two experimental campaigns, while γ seems to be the most sensible parameter to V_{water} and V_{air} changes. It is possible to identify two different zones for lower and higher flows and as expected the dynamical differences between the two

sets of experiments increase with the flow rate as shown in figure *4.1*.
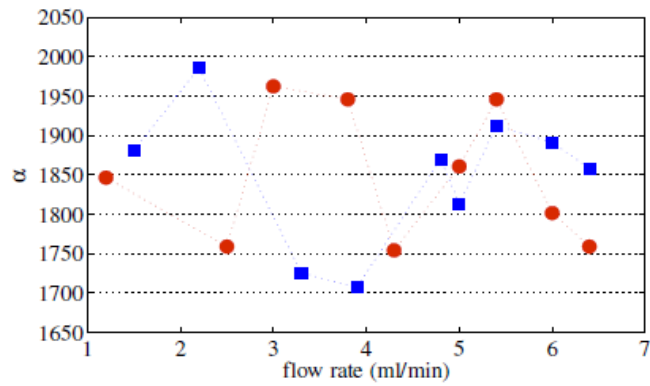
(a)
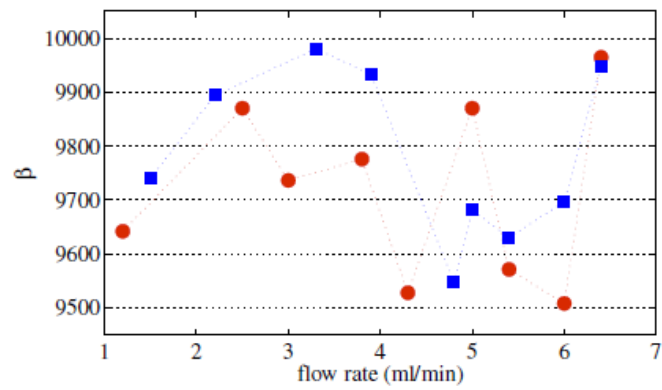
(b)

(c)

Figure. 4.11. The parameters (a) α versus flow rate (b) β versus flow rate (c) γ versus flow rate, results of V_{air} fixed are indicated by blue squares while V_{water} fixed with red circles.
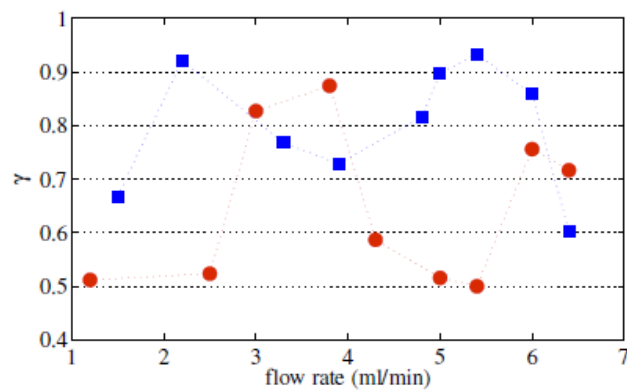
An approach for the identification of the microfluidic process is presented and discussed. This is a new methodology for state identification of the main features in experimental time series. The identification is based on master slave synchronization. In particular the parameters of the Chua's model were estimated by the minimization of a suitable index and parameters are chosen by means of standard genetic algorithm procedure.

The strength of this approach is that unknown nonlinear flows could be identified without any particular assumption using the presented procedure. On the contrary the limit remains model selection and the complete synchronization between the two systems. A future work will deal with the correlation between the Chua's model and physical parameters of the microfluidic processes.

CONCLUSION

Computational fluid dynamics (*CFD*) is an important tool in microfluidics, providing detailed information when theoretical models and experimental results are unavailable or difficult to obtain. The analysis of elementary flow in micro channels of different cross sections, comparing the flow rate in a rectangular channel.

In the chapter-2, through computational model analysis of the T-Junction, it is possible to determine the geometric proportions that allow a numerical stability and achieve a dynamic characterization of the system.

Thus allows, from the flow of fluid input, the frequency, and the bubbles generate. This activity has been considerable benefit when the face of the work on the logic gate: being able to characterize the generators, it has been possible to better adapt the size, as well as the speed and timing of the bubbles so as to contribute significantly to correct operation of the logic gate.

The universal logic gates i.e., AND/OR gate: type-1, type-2, NOT gate and toggle flip-flop can be used to create complex microfluidic circuits capable of performing illogical fluid process control and computation in an integrated approach. Such circuits may reduce the size, cost, and complexity of current microfluidic systems, thereby enabling the development of very-large-scale microfluidic reactors for use in areas including combinatorial chemistry and drug discovery.

In chapter-3, the study and design of a system embedded in micro-optofluidics allows very narrow spaces in a microfluidic system, guaranteeing certain portability, which integrates the optical functions.

Thus achieving the right balance between the two disciplines, played as a part of a global project in which design and manufacture of micro-devices, studies and experiments within micro optofluidic could easily fit in a biochemical analysis of the microscopic scales of biological particles of various kinds.

In chapter-4, an approach for the identification of the microfluidic process is presented and discussed. This is a new methodology for state identification of the main features in experimental time series. The identification is based on master slave synchronization. In particular the parameters of the Chua's model were estimated by the minimization of a suitable index and parameters are chosen by means of standard genetic algorithm procedure.

The strength of this approach is that unknown nonlinear flows could be identified without any particular assumption using the presented procedure. On the contrary the limit remains model selection and the complete synchronization between the two systems.

REFERENCE

[1]   H. Bruus, "***Theoretical Microfluidics***", Oxford University Press, Newyork, USA (2008).

[2]   Springer, "***Microfluidics and Nanofluidics***", 12, pp. 841-886 (2012).

[3]   IEEE Circuits and Systems magazine, 9, pp.6-17 (2009)

[4]   P. Garstecki, A.M. Ganan-calvo, and G.M. Whitesides, "***Formation of bubbles and droplets in microfluidic systems***", Bulletin of the Polish Academy of Sciences Technical Sciences, 53 (2005).

[5]   E. Verneuil, M. L. Cordero, F. Gallaire, and C. N. Baroud, "***Laser-Induced Force on a Microfluidic Drop: Origin and Magnitude***", Langmuir, 25, pp. 5127–5134 (2009).

[6]   M. Prakash and N. Gershenfeld, "***Microfluidic Bubble Logic***", 2 7;

[7]   L. F. Cheow, L. Yobas, and D. L. Kwong, "***Digital microfluidics: Droplet based logic gates***", (2007).

[8]   M. Prakash and N. Gershenfeld, "***Synchronization in microfluidic circuits***", Centre for Bits and Atoms, MIT, USA.

[9]   Patent application publication, "***Microfluidic Bubble Logic Devices***", (2008).

[10]   P. Anandan, F. Schembri, and M. Bucolo, "***Computational modeling of droplet based logic circuits***", AIP, 1479, pp. 220-223 (2012).

A.   John D, "***Computational fluid dynamics***", Oxford University Press, 2010.

[11]   Springer, "***Springer Handbook of Nanotechnology***", 2004.

[12]   Delville et al, "*Laser microfluidics: fluid actuation by light*", J. opt. A: Pure Appl. Opt. 11, pp. 15, (2009).

[13]   Grier D, Nature 424, pp. 810 (2003)

[14]   Dholakia K, MacDonald M P, Zemanek P and Cizmar T, Methods Cell Biol, 82 pp. 467 (2007).

[15]   Psaltis D, Quake S R and Yang C, Nature, 442, pp.381 (2006).

[16]   Hunt H C and Wilkinson J S, Microfluid. Nanofluid, 4, pp. 53, (2008).

[17]   Monat C, Domachuk P, Grillet C, Collins M, Eggleton B J, Cronin Golomb M, Mutzenich S, Mahmud T, Rosengarten G and Mitchell A, Microfluid. Nanofluid, 4, pp. 81 (2008).

[18]   H. Kopka and P. W. Daly, "*A Guide to LATEX*", 3rd ed. Harlow, England: Addison-Wesley, 1999.

[19]   E. Aurell, G. Boffetta, A. Crisanti, G. Paladin, A. Vulpiani, "*Predictability in the large: an extension of the concept of Lyapunov exponent*", J. Phys. A., 30, pp. 1-26 (1997).

[20]   S. Boccaletti, J. Kurths, G. Osipov, D. L. Vallardes, C. S. Zhou, "*The synchronization of chaotic systems*", Phys. Rev., 366, pp. 1-101 (2002).

[21]   N. Boccara, "*Modeling Complex Systems*", Springer-Verlag, New York (2004).

[22]   A.Bonasera, M. Bucolo, L. Fortuna, M. Frasca, A. Rizzo, "*The d1 parameter to characterise chaotic dynamics. Nonlinear Phenomena in Complex Systems*", 6, pp. 565-570 (2003).

[23] M.R. Bringer, C.J. Gerdts, H. Song, J.D. Tice, R.F. Ismagilov, "*Microfluidic systems for chemical kinetics that rely on chaotic mixing in droplets*", Philos. T. Roy. Soc. A. 362, pp. 1087-1104 (2004).

[24] T. Cubaud, C.M. Ho, "*Transport of bubbles in square microchannels*", Physics of Fluids, 16, pp. 4575-485 (2004).

[25] J. R. Dormand, P. J. Prince, "*A family of embedded Runge-Kutta formulae*", Journal of Computational and Applied Mathematics, 6, pp.1926 (1980).

[26] Dreyfus, R., Tabeling, P., Willaime, H.: "*Ordered and disordered patters in two-phase flows in microchannels*", Phys. Rev. Lett. 90 (2003).

[27] Journal of latex class files, 6, (2007).

[28] D.E. Golbert, "*Genetic Algorithms in Search, Optimization and Machine Learning*", Addison Wesley (1989).

[29] Griffiths, A.D., Tawfik, D.S.:"*Miniaturizing the laboratory in emulsion droplets*". Trends in Biotechnology 249, pp.395-402 (2006).

[30] Hegger, R., Kantz H., and Schreiber T.: "*Practical implementation of nonlinear time series methods: The TISEAN package*", Chaos, 9, pp. 413 (1999).

[31] M. Hesler, "*Synchronization Principles and Applications*", ISCAS'94 Tutorials, pp. 314-327 (1994).

[32] H. Kantz, T. Schreiber, "*Nonlinear Time Series Analysis*", Cambridge University Press, Cambridge (2004).

[33] R. N. Madan, Chua's Citcuit: "*A Paradigm for Chaos*", World Scientific pub., vol. 1, Series B, Singapore (1993).

[34] V. Labrot, M. Schindler et al., "*Extracting the hydrodynamic resistance of droplets from their behavior in microchannel networks*", Biomicrofluidics, 3(1):12804 (2009)

[35] N. Lorber et al, "*Some recent advances in the design and use of miniaturized droplet-based continuous process: application in chemistry and high-pressure microflow*", Lab on Chip, 11(5), pp. 779-787 (2011).

[36] N.-T. Nguyen, S. Wereley, "*Fundamentals and applications of microfluidics*", (ed.) Integrated Microsystems Series, Artech House (2002).

[37] L. M. Pecora, T. L. Carroll, "*Synchronization in chaotic systems*", Phys. Rev. Lett., 64:8, pp. 821-824 (1990).

[38] M. G. Rosenblum, A. S. Pikovsky, J. Kurths, "*From Phase to Lag Synchronization in Coupled Chaotic Oscillators*", Phys. Rev. Lett., 78:22, pp. 4193-4196 (1997).

[39] Rosenstein, M. T., Collins, J. J., De Luca, C. J.: "*A practical method for calculating largest Lyapunov exponents from small data sets*", Physica D, 65, pp.117 (1993).

[40] F. Schembri, F. Sapuppo, M. Bucolo, "*Experimental Identification of Nonlinear Dynamics in Microfluidic Bubble Flow*", Nonlinear Dynamics, Springer.

[41] J.C. Sprott, S. Wereley, "*Chaos and Time-Series Analysis*", Oxford University Press, Oxford (2003).

[42] J.M.T. Thompson, H.B Stewart, "*Nonlinear Dynamics and Chaos*", John Wiley and Sons (1989).

[43] H Willaime, V. Barbier, L. Kloul, S. Maine, and P. Tabeling, Phys. Rev. Lett., 96 (2006).

[44] C. N. Baroud, H. Willaime, "*Multiphase flows in microfluidics*", C. R. Physique, 5, pp. 547–555 (2004).

[45] George M. Whitesides, "*The Origins and the Future of Microfluidics*", nature, 442 (2006).

[46] Charles N. Baroud, Francois Gallaireb and Remi Dangla, "*Dynamics of microfluidic droplets*", Lab Chip, 10, pp. 2032–2045, (2010).

[47] Peter Gravesen, Jens Branebjerg and Ole Sondergard Jensen, "*Microfluidics-a review*", J. Mioromech. Microeng, 3, pp. 168-182 (1993).